



UNIVERSITY
OF
JOHANNESBURG

COPYRIGHT AND CITATION CONSIDERATIONS FOR THIS THESIS/ DISSERTATION

 creative
commons



- Attribution — You must give appropriate credit, provide a link to the license, and indicate if changes were made. You may do so in any reasonable manner, but not in any way that suggests the licensor endorses you or your use.
- NonCommercial — You may not use the material for commercial purposes.
- ShareAlike — If you remix, transform, or build upon the material, you must distribute your contributions under the same license as the original.

How to cite this thesis

Surname, Initial(s). (2012) Title of the thesis or dissertation. PhD. (Chemistry)/ M.Sc. (Physics)/ M.A. (Philosophy)/M.Com. (Finance) etc. [Unpublished]: [University of Johannesburg](https://ujcontent.uj.ac.za/vital/access/manager/Index?site_name=Research%20Output). Retrieved from: https://ujcontent.uj.ac.za/vital/access/manager/Index?site_name=Research%20Output (Accessed: Date).



UNIVERSITY
OF
JOHANNESBURG

**SYNTHESIS AND CHARACTERIZATION OF MESOPOROUS SILICA/TITANIA
NANOCOMPOSITES: POTENTIAL ADDITIVES FOR DYE SENSITIZED SOLAR
CELLS (DSSCs)**

by

MPINGANA NDILIMEKE AKAWA

Student Number: 215062259

Dissertation in fulfilment of the requirement for the degree

MASTERS

in

NANOSCIENCE

in the

FACULTY OF SCIENCE

of the

UNIVERSITY OF JOHANNESBURG

Supervisor : PROF PATRICK G. NDUNGU

Co-supervisors : Dr MESSAI MAMO

DEDICATION

This work is lovingly dedicated to my beloved family: more especially to my husband Inekela Kambindji, my mother Meme Beatha Akawa; my children: Sindano, Tulimeke, Inekela and Eтуhole. For their love, support and understanding! And to the lovely memories of my Father, Tate Isak Akawa and brother, Kristof Akawa.



PRESENTATIONS AND MANUSCRIPTS

Conference Presentations

1. **Mpingana N. Akawa, Messai Mamo, Patrick G. Ndungu: Synthesis and characterization of mesoporous Silica/Titania nanocomposites for DSSC application. Poster presentation at the 6th UJ Inter-faculty Post graduate Symposium, University of Johannesburg. 14 October 2016**
2. **Mpingana N. Akawa, Messai Mamo, Patrick G. Ndungu: Synthesis and characterization of mesoporous Silica/Titania nanocomposites for Dye-Sensitized Solar Cells (DSSCs) Application. Oral Presentation at the 1st Nanoscience Symposium of the NNPTTP, Hotel Verde, Cape Town. 03 October 2016**

MANUSCRIPT

1. **Titania supported on mesoporous silica (SBA-15): Synthesis and Characterization**
Submitted to the Supervisor

ACKNOWLEDGEMENT

I would like to express my appreciation and gratitude to the following people and organisations for their contributions towards the success of this work:

- ❖ My Supervisors, Prof Patrick G. Ndungu and Dr Messai Mamo for their guidance and support during the course of the research work.
- ❖ University of Johannesburg Faculty of Science and Namibia Students Financial Assistance Fund (NSFAF) for their financial support during my studies.
- ❖ National Commission on Research, Science and Technology (NCRST, Namibia) and the National Nanoscience Postgraduate Teaching and Training Platform (NNPTTP, South Africa) for funding this research work.
- ❖ Eric Ngigi, Applied Chemistry Department, for his assistance with Raman analysis and guidance & training of the XRD technique.
- ❖ Bhekumuzi Gumbi, Chemistry Department, University of Kwa-Zulu Natal (UKZN) for Nitrogen Desorption Analysis.
- ❖ Fellow postgraduate students within the department and friends for their support.
- ❖ My beloved family for their love, unending support and understanding.
- ❖ Last but not least, the Lord Almighty for giving me strength to endure it all.

UNIVERSITY
OF
JOHANNESBURG

ABSTRACT

The photoanode is an important part of the DSSCs as it is the medium for dye adsorption, electron transport and electrolyte diffusion. The composition and morphology of the photoanode therefore directly influences the performance of the cell. Optimising the morphology of the photoanode is therefore one of the key factors in improving the performance of the DSSCs. This work entailed the synthesis of titania supported on silica nanocomposites for use as light scattering materials in the photoanode with the motivation of optimising the morphology of the photoanode and further enhance the energy conversion efficiency of the DSSCs.

The silica support materials, specifically mesoporous silica, SBA-15 and non-mesoporous SiO₂ were synthesized through the soft-template acid catalyzed sol-gel method and base catalyzed sol-gel method respectively. Two SBA-15 nanomaterials were synthesized by varying the hydrolysis and aging times which resulted in materials of different textural and morphological properties. These silica support materials (SiO₂, SBA-15 A1 and SBA-15 A2) were used as support materials for the synthesis of TiO₂ supported on silica nanocomposites. Also, TiO₂ nanoparticles of size 19.32 ± 3.70 nm (n = 193) were synthesized for use as active site of the photoanode. The physical, chemical and optical properties of the nanoparticles and nanocomposites were studied using FTIR, TEM, Nitrogen Sorption, SEM-EDS, XRD, and diffuse reflectance Ultraviolet-Visible (DR-UV-VIS) spectroscopy.

The nitrogen desorption results of the 10 wt% TiO₂ / SBA-15 nanocomposites just like the parent SBA-15 support, revealed the Type IV isotherms with H1 hysteresis loops which indicated that the support materials did not lose their mesoporosity and uniform pore size arrangement upon incorporation of TiO₂ nanocrystals. This finding was supported by the TEM results.

The energy band gaps of TiO₂ supported on the mesoporous silica (SBA-15) (3.60 eV) were blue shifted relative to the unsupported TiO₂ (3.44 eV) and TiO₂ supported on the non-mesoporous SiO₂ (3.55 eV). These results confirmed the XRD results which indicated smaller TiO₂ crystallite sizes for TiO₂ crystals supported on the SBA-15 support materials which were 10.60 nm as compared to the unsupported TiO₂ and TiO₂ supported on the non-mesoporous SiO₂ (15.89 nm). The band gap increased as the crystallite sizes decreased.

The TiO₂ nanoparticles were used to prepare the pastes for the photoanodes, with addition of 10% wt of the nanocomposites. The photoanodes were evaluated for the dye loading capacity and their effect on the morphology of the photoanodes. The photoanode incorporated with 10 wt% TiO₂ / SBA-15 A1, which had a higher surface area, adsorbed more dye molecules than the rest of the composites. Also the top view surface morphology of the photoanode incorporated with 10 wt% TiO₂ / SBA-15 A1 had a smoother surface than the rest of the photoanode which could result in better electron transport and electrolyte diffusion.

The photoanodes, counter electrodes and electrolyte were assembled together to form DSSC devices which were evaluated for performance under illumination using a 45 W incandescent lamp and dark current. The devices incorporated with the nanocomposites showed improvement in terms of the short circuit current density, relative to the TiO₂ reference devices. However, the devices showed the electrical behaviour of the photodiodes instead of the photovoltaic cells. This was possibly due to the method used to assemble the devices which could have resulted in two separate layers which behaved as the N-doped (top layer) and P-doped (bottom) layers. When the light shined on the top layer, the top layer acted as an electron collector while the bottom layer acted as a hole collector at the junction, creating the depletion region between the layers. Thus further work on these devices is beyond the scope of the current project; however, this work does provide new and exciting directions of research with photo-electrochemical systems.

Keywords: Dye Sensitized Solar cell, Mesoporous Silica, Titania, porosity, photoanode

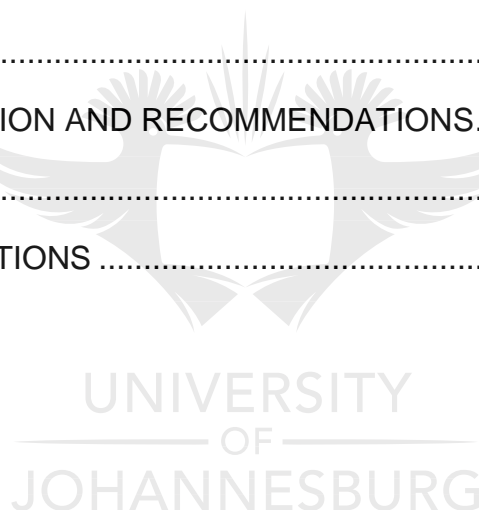
TABLE OF CONTENTS

DECLARATION.....	i
DEDICATION	ii
PRESENTATIONS AND MANUSCRIPTS	iii
ACKNOWLEDGEMENT	iv
ABSTRACT	v
TABLE OF CONTENTS	vii
LIST OF FIGURES.....	xi
LIST OF TABLES	xiii
LIST OF ABBREVIATIONS.....	xiv
CHAPTER 1: INTRODUCTION.....	1
1. BACKGROUND AND MOTIVATION	1
1.1. Problem Statement.....	5
1.2. Aim and Objectives of the research project	5
1.3. Research Approach.....	6
1.4. Research Scope	6
1.5. Outline	7
1.6. REFERENCES	8
CHAPTER 2: LITERATURE REVIEW.....	9
2. INTRODUCTION	9
2.1 Brief History of DSSCs	9
2.2 Operating Principle of DSSCs	10
2.2.1 Charge Transfer Processes in DSSCs	12
2.2.2 Characterizing key electrical parameters and efficiency	14
2.2.2.1 Short Circuit Current Density (J_{sc})	15
2.2.2.2 Open Circuit Voltage (V_{oc})	15

2.2.2.3	Fill Factor (FF).....	16
2.2.2.4	Energy Conversion Efficiency (η)	16
2.3	Components of the DSSCs.....	16
2.3.1	Working Electrode	17
2.3.1.1	Transparent Conducting oxide (TCO) Substrate	17
2.3.1.2	Titania: Mesoporous Semiconductor Oxide Layer	17
2.3.1.3	Sensitizer/Dye	18
2.3.2	Electrolyte.....	20
2.3.3	Counter Electrode.....	21
2.4	Mesoporous Materials	22
2.4.1	Ordered Mesoporous Silica (OMS).....	23
2.4.2	SBA-15	24
2.5	Recent development in working electrodes	25
2.5.1	The Light Scattering Approach	26
2.6	REFERENCES	30
CHAPTER 3: EXPERIMENTAL		35
3.	INTRODUCTION	35
3.1	Chemicals and Materials	35
3.2	Characterization Techniques	36
3.2.1	Nitrogen Absorption-Desorption Isotherm Analysis	36
3.2.2	Fourier Transform Infrared Spectroscopy	37
3.2.3	Transmission Electron Microscopy	37
3.2.4	Scanning Electron Microscopy	38
3.2.5	X-ray Diffraction (XRD).....	38
3.2.6	Diffuse Reflectance Ultraviolet-Visible (DRS UV-Vis) Spectroscopy	38
3.2.7	Raman Analysis.....	39
3.3	METHODOLOGY	39
3.3.1	Synthesis of Titanium Dioxide Nanoparticles.....	39

3.3.2	Synthesis of silica support materials.....	40
3.3.2.1	Synthesis of the non-mesoporous Silica particles	40
3.3.2.2	Synthesis of SBA-15	40
3.3.3	Synthesis of the Nanocomposites	41
3.3.3.1	Synthesis of 10% Titania Supported on Silica Nanocomposites ..	41
3.4	FABRICATION OF THE DSSCS	42
3.4.1	Cleaning of the FTO glass	42
3.4.2	Preparation of the working electrode	42
3.4.2.1	Preparation and application of the paste	42
3.4.2.2	Preparation of the dye solution and dye adsorption	44
3.4.2.3	Dye Adsorption Capacity Analysis.....	44
3.4.2.4	Characterization of the photoanodes.....	44
3.4.2.5	Preparation of the counter electrodes	44
3.4.3	Assembly and evaluation of the DSSCs	45
3.5	REFERENCES	46
CHAPTER 4: RESULTS AND DISCUSSION.....		47
4.	INTRODUCTION	47
4.1	CHARACTERIZATION OF TITANIA NANOPARTICLES	47
4.1.1	XRD ANALYSIS OF TiO ₂ SAMPLE	47
4.1.2	RAMAN ANALYSIS	48
4.1.3	TEM ANALYSIS	49
4.2	CHARACTERIZATION OF SILICA SUPPORT MATERIALS	50
4.2.1	TEM ANALYSIS	50
4.2.1.1	Non-mesoporous Silica Particles.....	50
4.2.1.2	Mesoporous silica SBA-15 A1 and SBA-15 A2 particles	51
4.2.2	Textural properties of SiO ₂ and SBA-15 samples.....	52
4.3	CHARACTERIZATION OF TITANIA SUPPORTED ON SILICA NANOCOMPOSITES.....	54
4.3.1	XRD ANALYSIS	54
4.3.2	Textural properties of the nanocomposites.....	56

4.3.2.1	Titania supported on non-mesoporous silica (10 wt% TiO ₂ / SiO ₂) sample 56	56
4.3.2.2	Titania supported on mesoporous Silica (10 wt% TiO ₂ / SBA-15 A1 and 10 wt% TiO ₂ / SBA-15 A2) samples.....	57
4.3.3.1	TEM ANALYSIS	60
4.3.3.2	SEM-EDS ANALYSIS	61
4.3.4	FTIR ANALYSIS	62
4.4	APPLICATION.....	65
4.4.1	PHOTOANODE MORPHOLOGY	66
4.4.2	DYE LOADING ANALYSIS.....	67
4.4.3	Testing and evaluation of the DSSC devices.....	69
4.5	SUMMARY	72
4.6	REFERENCES	73
CHAPTER 5: CONCLUSION AND RECOMMENDATIONS.....		75
5.1	CONCLUSION.....	75
5.2	RECOMMENDATIONS	76



LIST OF FIGURES

Figure 1.1:	Classification of Photovoltaic (PV) cells	3
Figure 2.1	Components and working principle of the DSSC.....	11
Figure 2.2:	Figure provides a simplified energy diagram of DSSCs, adapted from the reference	12
Figure 2.3:	Typical I-V characteristic plot for solar cells	14
Figure 2.4:	Structures of N3 and N719 dyes	19
Figure 2.5:	Pore structures of Ordered Mesoporous Silica.....	23
Figure 3.1:	Illustration of how ImageJ software was used to determine the particle sizes of spherical particles.	37
Figure 3.2:	Examples of DSSC devices assembled for testing.....	45
Figure 4.1:	The XRD diffraction pattern of TiO ₂ sample synthesized via a sol-gel method.	48
Figure 4.2:	The Raman Spectrum of TiO ₂ sample.....	49
Figure 4.3:	(a) TEM image and (b) the particle size diameter plot (n = 193) of the TiO ₂ sample.....	50
Figure 4.4:	(a) TEM Image and (b) Particle Size Distribution plot (n = 152) of the non-mesoporous silica sample.....	51
Figure 4.5:	TEM images of (a) - (b) SBA-15 A1 and (c) - (d) SBA-15 A2 samples.	52
Figure 4.6:	Nitrogen desorption isotherms for (a) SiO ₂ , (b) SBA-15 A1 and A2 and (c) their respective pore size distribution plots.	53
Figure 4.7:	The XRD diffraction patterns of Titania supported on silica (a) 10 wt% TiO ₂ / SiO ₂ , (b) 10 wt% TiO ₂ / SBA-15 A1 and (c) 10 wt% TiO ₂ / SBA-15 A2.....	55
Figure 4.8:	(a) Nitrogen desorption isotherm and (b) pore size distribution plot for (a) 10 wt% TiO ₂ / SiO ₂ sample.	57
Figure 4.9:	(a) Nitrogen sorption isotherms and (b) pore size distribution plots for SBA-15 A1 and 10 wt% TiO ₂ / SBA-15 A1 samples. SBA-15 A1 hydrolysis and aging times were 7.5 h and 18 h respectively. Panels (c) nitrogen sorption isotherms and (d) pore size distribution plots for SBA-	

	15 A2 and 10 wt% TiO ₂ / SBA-15 A2 samples. SBA-15 A2 hydrolysis and aging times were 24 h and 24 h respectively.....	58
Figure 4.10:	Types of pores found in SBA-15 after impregnation with nanoparticles, drying and calcination.....	60
Figure 4.11:	The TEM micrograms of the synthesized nanocomposites (a) 10 wt% TiO ₂ / SiO ₂ , (b) 10 wt% TiO ₂ / SBA-15 A1 and (c) 10 wt% TiO ₂ / SBA-15 A2.....	61
Figure 4.12:	The SEM images of (a) SBA-15 A1, (b) SBA-15 A2, (d) 10 wt% TiO ₂ / SBA-15 A1 and (e) 10 wt% TiO ₂ / SBA-15 A2 and EDS spectra of (c) silica support samples and (f) Titania supported on silica.	62
Figure 4.13:	The FTIR Spectra of (a) 10 wt% TiO ₂ / SBA-15, (b) 10 wt% TiO ₂ / SiO ₂ , (c) Silica and (d) TiO ₂ samples.....	63
Figure 4.14:	(a) The absorbance spectra and (b) the corresponding Kubelka-Munk plots of the unsupported and supported TiO ₂ samples.....	64
Figure 4.15:	SEM images of modified and unmodified electrodes: (a) TiO ₂ , (b) TiO ₂ + 10% TiO ₂ / SiO ₂ , (c) TiO ₂ + 10% TiO ₂ / SBA-15 A1 and (d) TiO ₂ + 10% TiO ₂ / SBA-15 A2.	66
Figure 4.16:	The Absorption Spectra of the N719 dye solution desorbed from the dye-sensitized TiO ₂ ; TiO ₂ + 10% TiO ₂ / SiO ₂ ; TiO ₂ + 10% TiO ₂ / SBA-15 A1 and TiO ₂ + 10% TiO ₂ / SBA-15 A2 photoanodes using 0.1 M NaOH aqueous solution.	68
Figure 4.17:	The Current-Voltage curves measured under (a) irradiance, (b) dark current and (c) an ideal DSSC curve [31]. Dark current curves for the devices showed similar trends, hence only one dark current curve is shown.....	69
Figure 4.18:	The characteristic Current-Voltage curves of the photodiode.....	71

LIST OF TABLES

Table 3.1:	List of chemicals used for the synthesis of nanomaterials and nanocomposites and their purities and suppliers.....	35
Table 3.2:	List of Chemicals used for the fabrication of the DSSCs and their suppliers	36
Table 3.3:	The composition of the prepared photoanodes	43
Table 4.1:	Textural properties of the synthesized materials	54
Table 4.2:	The crystallite sizes, calculated from the XRD pattern results, 2θ and FWHM using the Scherrer equation, of the supported and unsupported TiO_2 nanocrystals.	56
Table 4.3:	Textural properties of the synthesized particles and nanocomposites	59
Table 4.4:	The band gaps of the unsupported and supported TiO_2 in relation to their crystallite sizes.	65



LIST OF ABBREVIATIONS

TiO ₂	Titanium Dioxide
TEOS	Tetraethyl orthosilicate
TTIP	Titanium Tetraisopropoxide
DSSC	Dye Sensitized Solar Cell
P123	Poly(ethylene glycol)-block-poly(propylene glycol)-block-poly(ethylene glycol)
PEG	Polyethylene glycol
AM 1.5G	Air Mass 1.5 Global
SiO ₂	Silicon dioxide
ITO	Indium-doped Tin Oxide
SBA-15	Santa Barbara Amorphous
FTO	Fluorine doped Tin Oxide
FTIR	Fourier Transform InfraRed Spectroscopy
SEM	Scanning Electron Microscope
TEM	Transmission Electron Microscope
HOMO	Highest Occupied Molecular Orbital
XRD	X-Ray Diffraction
LUMO	Lowest Unoccupied Molecular Orbital
PV	Photovoltaic
EIS	Electrochemical Impedance Spectroscopy
IUPAC	The International Union of Pure and Applied Chemistry
DR-UV-Vis	Diffuse Reflectance Ultra Violet Visible

BET	Brunauer–Emmett–Teller
BJH	Barrett-Joyner-Halenda
FF	Fill Factor
M_w	Molecular Weight
FWHM	Full Width at Half Maximum
PCE	Power Conversion Efficiency
c-Si	Single Crystalline Silicon
Poly c-Si	Polycrystalline Silicon
Mono c-Si	Monocrystalline Silicon
CIGS	Copper Indium Gallium Selenide
GaAs	Gallium Arsenide
a-Si	Amorphous Silicon
CdTe	Cadmium Telluride
OPV	Organic Photovoltaics
qDSSC	Quantum dot Dye Sensitized Solar Cells

CHAPTER 1: INTRODUCTION

This chapter introduces an overview of the worldwide energy demands with the aim of clarifying the importance of seeking alternative renewable energy sources. Among all the alternative renewable sources, the chapter focuses mainly on current situation of photovoltaic technologies specifically the 1st, 2nd and 3rd generations of solar cells. The need for developing affordable, highly efficient PV devices while acknowledging the documented challenges associated with dye sensitized solar cells are emphasized. The aims and objectives of the research project as well as the research scope and approach are highlighted towards the end of the chapter. And finally, a presentation of the thesis outline concludes this introductory chapter.

1. BACKGROUND AND MOTIVATION

The world's energy consumption is increasing tremendously due to the present economic reforms, population growth and vast technological developments. Currently, the maximum global power consumption is about 13 TW and is expected to grow to 17 TW by 2030 [1, 2]. Climate change, pollution, and energy insecurity are some of the greatest challenges of our generation and addressing them necessitates major changes in the types of energy sources utilized and accompanying infrastructures.

The heavy reliance on fossil fuels as the primary source of energy has not only caused environmental problems, but it has also accelerated the depletion of fossil fuel reserves. Combustion of fossil fuels results in the production of greenhouse gases (GHGS) which are released into the environment. These gases cause a series of environmental issues such as acid rain, climate change and weakening of the ozone layer. Mining and exploration of minerals for nuclear power and other energy generating systems also result in land degradation and environmental pollutions. These environmental problems do not only damage the ecosystem alone, but they negatively affect humans as well as terrestrial and aquatic plants and animals [3-5].

The negative environmental impacts and other problems related to the utilization of fossil fuels as the main source of energy have shifted the effort into seeking environmentally friendly alternative energy sources that are renewable to sustain the growing energy demand. The renewable sources of energy include wind, hydropower, biomass, geothermal

and solar energy [2, 3]. Despite the disadvantages of utilising fossil fuels as sources of energy, renewable energy technologies have not been fully utilized because of the nature of some renewable sources and geographically restricted environments. Some regions of the world receive limited solar irradiance and solar energy may not be practical while arid and semi-arid regions may not fully utilize hydropower energy [3].

The use of renewable energy technologies has advantages such as diversification and secure energy supply, an increase of regional energy independence thereby saving on foreign exchanges, new wealth creation opportunities and acceleration of rural development opportunities and electrification and a much smaller negative environmental impact. Furthermore, the use of greener energy sources does not produce and emit pollutants in the atmosphere and smaller amounts of water is used, thereby reducing the burden on water resources [3, 6].

Among the renewable energy sources, solar energy has attracted more attention as the most viable option especially in developing countries within Africa due to its several advantages. In comparison to conventional energy sources, solar energy technologies provide apparent environmental advantages thereby contributing to the sustainability of human activities. Apart from reducing the burden on the already exhausted natural resources and solar energy abundance, the main advantages of the solar technologies include the reduction of greenhouse gases emissions, absence of pollutants and waste products during operation, reclamation of degraded land and improvement of the quality of water resources [2-4, 7].

Every year, the solar irradiance onto the earth every hour is 1.2×10^5 TW [3]. With the world's energy need at about 13 TW, even with a conversion at 10 % efficiency, this energy is more than enough to meet the energy needs of the world. There are several options for harnessing sunlight such as solar photovoltaic systems and concentrated solar power. Solar photovoltaic systems (SPVs) is the most recognized method of generating electricity from the sun. SPVs use the photovoltaic effect to convert electromagnetic energy directly into electricity. The electrons in the semiconductor or donor materials get excited by the photons from the sun and these electrons are transferred to the electrodes and thereby producing electricity [5, 6].

The basic working principle of solar cells was first demonstrated in 1839 by a French Physicist, Becquerel, and due to the use of newer technologies, the solar cell technologies

have grown over the years. Currently, solar cells are classified into three categories/ generations as shown in **Figure 1.1** below.

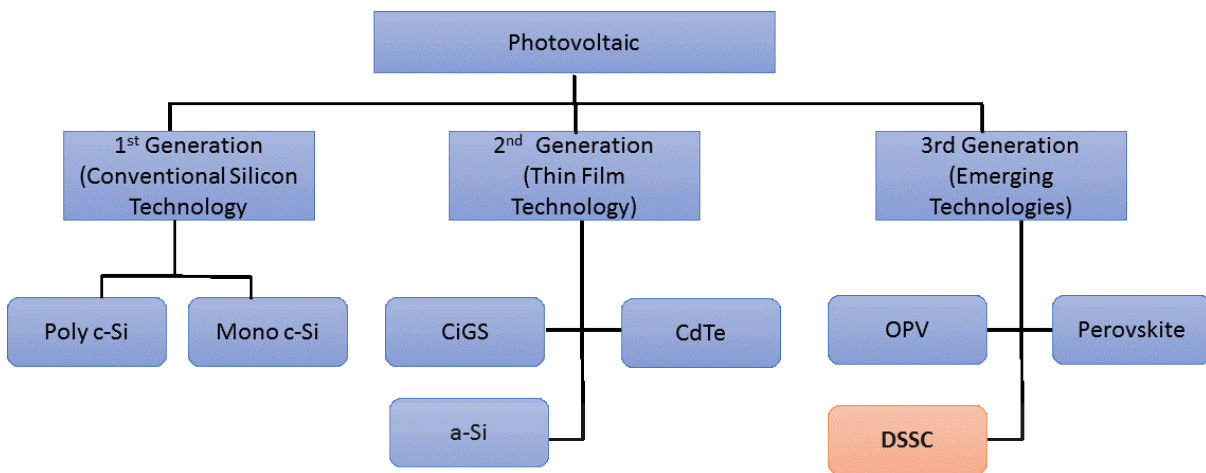


Figure 1.1: Classification of Photovoltaic (PV) cells

The first generation of solar cells were silicon based substrates such as single crystalline (c-Si), polycrystalline (poly-Si), and amorphous silicon (a-Si) which currently dominate the PV market [9], with highest efficiency at 25% for a monocrystalline silicon solar cell [8]. The second generation of solar cells replaced the use of silicon with thin film solar cells such as Copper-Indium Gallium Selenide (CIGS), Gallium Arsenide (GaAs) and Cadmium Telluride (CdTe) cells [9]. These cells have achieved efficiencies of about 23 % [8].

The first two generations of PV cells are single junction devices, and the efficiencies of these devices are limited by the Shockley-Queisser limit with a thermodynamic maximum limit of 31 – 33 % under AM 1.5 when the optimal band gaps are between 1.1 and 1.4 eV [9, 10]. This thermodynamic limit makes further improvement in efficiencies of the first and second generations of solar cells nearly impossible. In addition, the large scale commercialization of the first two generations is hampered by their high processing costs, as well as relatively lower efficiencies as compared to coal and nuclear power. Because of these challenges and limitations of the first and second generations, the PV research and development (R&D) over the last decades has focused on improving efficiencies, long term stability as well as usage of low cost, environmental friendly materials.

The third generation of solar cells are the emerging PV cells which include organic photovoltaic (OPV) cells [3] such as DSSCs and quantum-dot sensitized solar cells (qDSSCs) whose efficiencies are not limited by the Shockley-Queisser limit. An important

aspect of the third generation PV cells is that they are promising to produce electricity at a highly competitive price than the conventional solar cells. However, most of the third generation of solar cells are not yet available commercially but a lot of research is going on with promising results. Among the third generation PV cells, DSSCs offers more attractive features for mass production and commercialization however, the cell stability and efficiency remains a challenge and requires improvement. DSSCs have thus far achieved efficiency of about 13%.

Dye-sensitized solar cells (DSSCs) have received tremendous research attention as a possible candidate to realize the large-scale use of solar energy. This is because of advantages such as potential for moderate energy conversion efficiency, low production cost, compatibility with flexible substrates, easy-scale up and good performance under low incident light and high temperatures. However, the performance of the DSSCs, in terms of light conversion efficiency and long term stability still lag behind the performance of the conventional silicon solar cells which currently dominate the market.

The photoanode is an important part of the DSSCs as it acts as a media for dye adsorption, electron transport and electrolyte diffusion. The composition and morphology of the photoanode therefore directly influences the performance of the cell. Optimising the morphology of the photoanode is therefore one of the key factors in improving the performance of the DSSCs. This work entailed the synthesis of titania supported on silica nanocomposites for use as light scattering materials in the photoanode with the motivation of optimising the morphology of the photoanode and further enhance the energy conversion efficiency of the DSSCs.

1.1. Problem Statement

The main challenges facing the DSSC are the lower power conversion efficiency (PCE), long-term stability of the cells, thermoelastic expansion which induce liquid electrolyte leakages. Moreover higher PCE is only achieved with cells that are based on inflexible glass substrates are not suitable for large-scale manufacturing. The highest achieved efficiency for the DSSC is 13% which is lower than the conventional solar cells and requires further improvement for it to be commercially viable. Thus far, cell efficiency has been enhanced through three approaches namely:

- The improvement of light harvesting capability
- By reducing exciton recombination or
- Through a combination of the above two methods

The light scattering approach is used in DSSCs to enhance the possibility of interactions between the photons and dye molecules which consequently improves the conversion efficiency of the cell. The common method of introducing light scattering in DSSCs is by depositing a layer of large particles with diameters equivalent to the wavelength of the incoming light on the TiO₂ nanoparticle active layer. However, apart from this approach, nanomaterials can also be embedded in the active layer as light scatterers. Various nanostructures with efficient dye adsorption and light scattering properties such as core-shell and mesoporous materials have been used in the photoanode with promising results [11-15]. This research project aimed at developing SiO₂/TiO₂ nanocomposites and incorporating these nanocomposites as light scatterers in the photoanode for improving the light harvesting properties and hence improve the cell efficiency.

1.2. Aim and Objectives of the research project

The main goal of this research project was to synthesize and optimize photoanode materials for application in DSSCs, with the aim of understanding the physical-chemical properties of the synthesized materials. In this context, Silica support materials of different pore sizes were synthesized and used as support materials for titania nanoparticles.

The chemical and physical properties of the nanocomposites were studied using various techniques and the nanocomposites were used in the preparation of the working electrodes for the DSSCs. The overall aim of this research project was to investigate the effect of the

nanocomposites on light scattering efficiency and therefore on the improvement of the efficiency of the cell.

The individual tasks to achieve the objectives of this study were:

- Synthesis of silica support and TiO₂ Nanoparticles
- Synthesis of TiO₂ supported on silica nanocomposites
- Chemical and physical characterization of the synthesized nanostructures
- Preparation and evaluation of the photoanodes
- Assembly and performance evaluation of the DSSC devices as proof of concept with the modified photoanodes

1.3. Research Approach

The acid catalysed and base catalysed sol-gel methods were used to prepare TiO₂ and non-mesoporous silica samples respectively. The mesoporous silica (SBA-15) particles were synthesised using the soft template method, combined with acid catalysed sol-gel method using P123 as a structure directing agent. The TiO₂ supported on silica nanocomposites were also prepared via a sol-gel method. The physical, chemical and optical properties of the prepared materials were studied using various techniques. The nanocomposites were thereafter incorporated in the photoanodes of the DSSCs to study their effects on the morphology and dye adsorption capacity of the photoanodes and hence in the improvement of the light conversion efficiencies of the cells.

1.4. Research Scope

This research project focused on the synthesis, characterization and application of titania supported on silica nanocomposites in the photoanodes of the dye sensitized solar cells. The research scope of work and time frame only allowed for the synthesis and characterization of the 10 wt. % of TiO₂ / Silica nanocomposites. Also, for the modification of the photoanodes, only 10% of the composites were incorporated in the photoanodes. The morphology and dye adsorption capacity of the modified photoanodes were investigated using SEM and UV-Vis respectively. And lastly, the DSSC devices were assembled and tested.

1.5. Outline

The thesis outline below briefly describe the relevant aspects and discussions featured in each chapter.

Chapter 1

This chapter covers the background and the main objectives of this study.

Chapter 2

This chapter covers the literature review on the principle of operation and components of the DSSC, mesoporous materials as well as application of mesoporous material in the photoanode of the DSSC.

Chapter 3

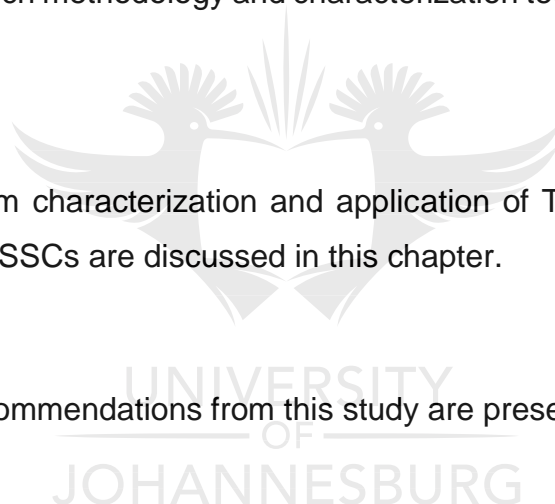
In this chapter, the research methodology and characterization techniques used in this study are presented.

Chapter 4

The results obtained from characterization and application of Titania supported on Silica nanocomposites in the DSSCs are discussed in this chapter.

Chapter 5

The conclusions and recommendations from this study are presented here.



1.6. REFERENCES

1. Aman, M.; Solangi, K.; Hossain, M.; Badarudin, A.; Jasmon, G.; Mokhlis, H.; Bakar, A.; Kazi, S. *Renewable and Sustainable Energy Reviews* **2015**, 41, 1190-1204.
2. Jacobson, M. Z.; Delucchi, M. A. *Energy Policy* **2011**, 39, (3), 1154-1169.
3. Keru, G.; Ndungu, P. G.; Nyamori, V. O. *International Journal of Energy Research* **2014**, 38, (13), 1635-1653.
4. Solangi, K.; Islam, M.; Saidur, R.; Rahim, N.; Fayaz, H. *Renewable and sustainable energy reviews* **2011**, 15, (4), 2149-2163.
5. Panwar, N.; Kaushik, S.; Kothari, S. *Renewable and Sustainable Energy Reviews* **2011**, 15, (3), 1513-1524.
6. Bahadori, A.; Nwaoha, C. *Renewable and Sustainable Energy Reviews* **2013**, 18, 1-5.
7. Tsoutsos, T.; Frantzeskaki, N.; Gekas, V. *Energy Policy* **2005**, 33, (3), 289-296.
8. NREL Best Research Cell Efficiencies. [cited 20 September 2016]; www.nrel.gov/pv/assets/images/efficiency_chart.jpg.
9. Reddy, K. G.; Deepak, T.; Anjusree, G.; Thomas, S.; Vadukumpully, S.; Subramanian, K.; Nair, S. V.; Nair, A. S. *Physical Chemistry Chemical Physics* **2014**, 16, (15), 6838-6858.
10. Jung, H. S.; Lee, J.-K. *The Journal of Physical Chemistry Letters* **2013**, 4, (10), 1682-1693.
11. Son, S.; Hwang, S. H.; Kim, C.; Yun, J. Y.; Jang, J. *ACS applied materials & interfaces* **2013**, 5, (11), 4815-4820.
12. Yang, C.-C.; Zheng, Y. R. *Journal of Power Sources* **2012**, 201, 387-394.
13. Deepak, T.; Anjusree, G.; Thomas, S.; Arun, T.; Nair, S. V.; Nair, A. S. *RSC Advances* **2014**, 4, (34), 17615-17638.
14. Tanvi; Mahajan, A.; Bedi, R. K.; Kumar, S.; Saxena, V.; Aswal, D. K. *Chemical Physics Letters* **2016**, 658, 276-281.
15. Ye, Y.; Jo, C.; Jeong, I.; Lee, J. *Nanoscale* **2013**, 5, (11), 4584-4605.

CHAPTER 2: LITERATURE REVIEW

2. INTRODUCTION

This chapter covers the literature review on the history, working principle and components of the DSSC. It also covers the mesoporous materials, synthesis as well as a comprehensive review on the application of mesoporous materials in the working electrodes of the DSSC and their effect on the performance of the DSSC devices.

2.1 Brief History of DSSCs

Conventional silicon solar cells continue to dominate the commercial solar cell market. However, in the last two decades, research momentum has grown in support of alternative solar cell devices such as organic solar cell technology and dye sensitized solar cells. Although silicon is abundantly available in the earth's crust, silicon is not found free but as oxides and therefore requires extensive processing before use in the manufacturing of solar cells. This extensive processing of silicon oxides makes silicon solar cells costly [1]. One economically viable alternative to the silicon solar cells is the dye sensitized solar cell.

A DSSC is a type of photo electrochemical cell which converts solar energy into electrical energy. The advantages of DSSCs, include moderate energy conversion efficiency (~13 %), low production cost, compatibility with flexible substrates, easy-scale up and good performance under low incident light and high temperatures (80 °C). These factors make DSSCs better competitors over the traditional solar cells [2-5].

The photosensitization of inorganic materials by dyes spans from several decades, starting with the dye sensitization of AgBr for photographic applications. The research continued on the photosensitization of wide band gap semiconductors such as ZnO by organic dyes and for photo-electrochemical processes. However, up to the 1970s, the conversion efficiencies remained as low as 1% [6, 7]. This changed in the early 1990s when Gratzel *et al.* made a breakthrough in DSSC research and invented the current structure of the DSSC. The breakthrough involved the incorporation of high surface area TiO₂ nanoparticles in the photoanode which improved the light harvesting properties of the cell. They incorporated a thin layer of dye onto the surface of a porous TiO₂ film, which then resulted in the collection of the photogenerated electrons from the dyes by the TiO₂ layer. Gratzel *et al.* achieved an

efficiency of 7.1 % under 1.5 AM condition [6, 8, 9]. This breakthrough motivated wide research interests on DSSCs, and resulted in an increase in DSSC research, covering areas of device operating mechanisms and its fundamental physics. Other research areas covered material innovation and novel structure designs and these have resulted in significant improvement in the performance and overall characteristics of the cell as well as reduced processing costs [7].

At the moment, DSSCs using ruthenium complexes have conversion efficiencies of around 13% under 1.5 AM conditions (NREL, 2016). Although the energy conversion efficiencies of the DSSCs are lower than the conventional PV solar cells, there is potential for the improvement of their efficiencies and overall cell characteristics with the use of innovative designs and materials, especially using nanomaterials.

2.2 Operating Principle of DSSCs

A DSSC is made up of three main components namely a photoelectrode, electrolyte and counter electrode. The photoelectrode, also referred to as photoanode or working electrode is made up of a transparent conductive oxide (TCO) supported on a glass substrate, a mesoporous wide-band gap semiconductor metal oxide nanoparticles film and a sensitizer such as ruthenium complex dyes adsorbed on the semiconductor metal oxide. The electrolyte consists of I^-/I_3^- redox couple in an organic solvent while the counter electrode is a platinized TCO glass substrate [8, 10, 11]. These components and the working principle of the DSSCs are shown in **Figure 2.1**.

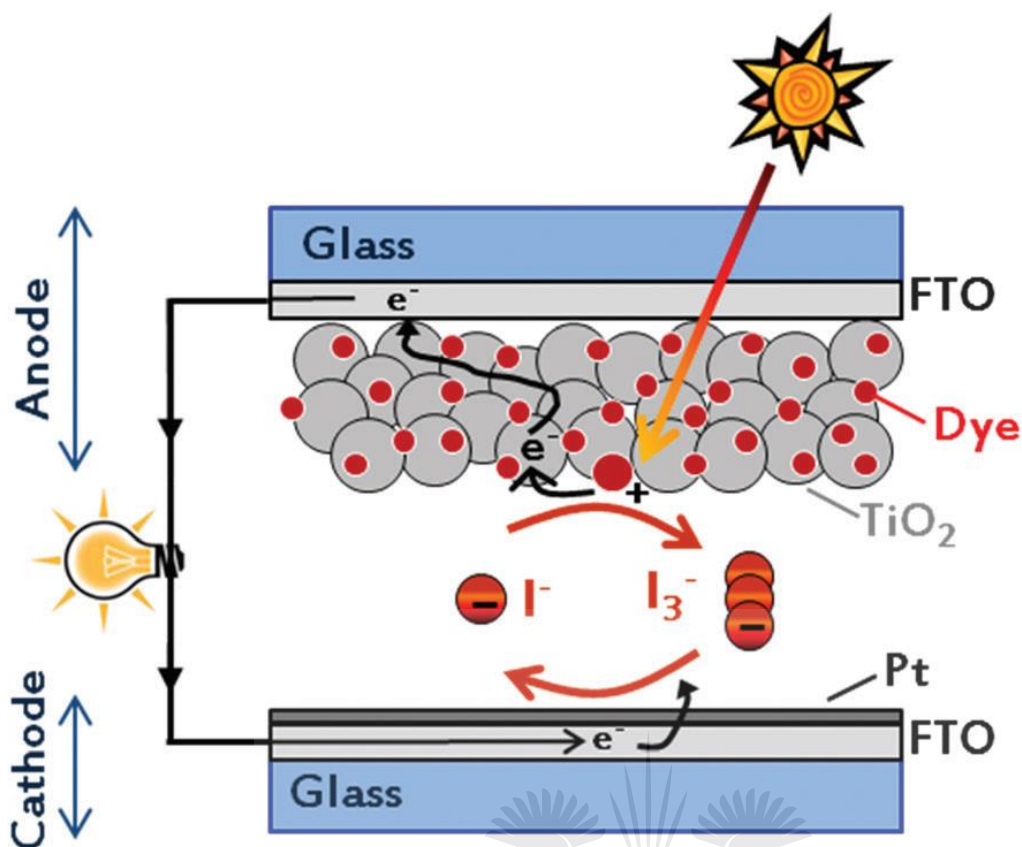


Figure 2.1 Components and working principle of the DSSC

When the dye molecules absorb incoming photons from the sun, electrons are generated by the dye molecules which are then transferred to the metal oxide films. The electrons percolate through the metal oxide films to the TCO such as fluorine doped tin oxide (FTO). The electrons are then transferred from the TCO and circulated through the external circuit, across a load, and finally reach the counter electrode. Platinum on the counter electrode acts as a catalyst for successive redox reactions which reduce the electrolyte, and in turn the electrolyte regenerates the dyes and therefore completing the circuit [1, 8, 12]. This description of the processes within a DSSC is oversimplified, but serves as a useful starting point when working with DSSCs. The following section provides a more in-depth review on the charge transfer processes with DSSCs.

2.2.1 Charge Transfer Processes in DSSCs

The electron transfer processes within DSSCs are depicted in the electronic band energy diagram shown in **Figure 2.2**, and the figure was adapted from the references [3, 8].

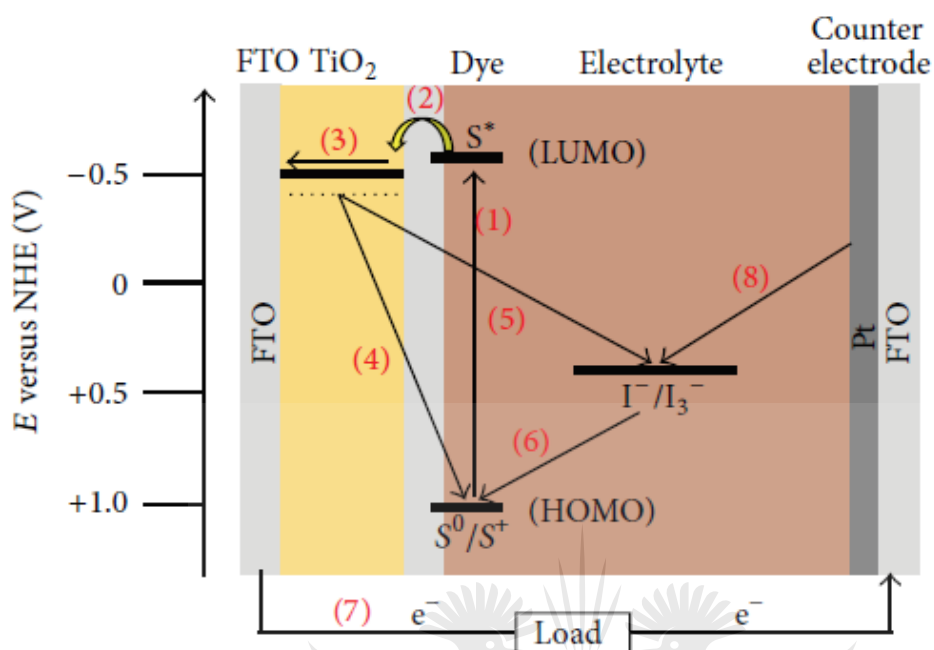


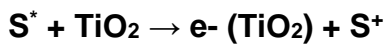
Figure 2.2: Figure provides a simplified energy diagram of DSSCs, adapted from the reference

Upon excitation of the dye by photons, electrons are excited from the highest occupied molecular orbital (HOMO) to the Lowest Unoccupied Molecular Orbital (LUMO) of the dye. This process has been shown to occur on the order of nanoseconds (ns) [8] and is represented by **Process (1)**.



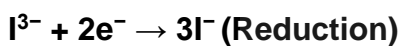
Process (1)

The electrons from the LUMO of the dye are then injected into the conduction band of the semiconductor metal oxide, and the process can be represented by **Process (2)**. For this process to occur, the energy levels of the dye must be higher than the conduction band (CB) of the metal oxide nanoparticles to prevent recombination of excitons. The Ru-complex dye molecules stay in the excited state for 20–60 ns which is long enough for dynamic competition between electron injection by the dye into the CB of the metal oxide and the excited state decay in the sensitizer/dye.

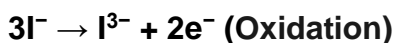


Process (2)

The electrons injected into the CB of the semiconductor oxide nanoparticles then percolate through the mesoporous film as indicated in **Process (3)**. The basic DSSC working electrode is usually assembled with a relatively high surface area nanoparticles (20-30 nm) of anatase TiO₂. However, apart from the low electron mobility ($2.3 \times 10^{-4} \text{ cm}^2/\text{Vs}$) of the TiO₂, the nanoparticles that make up the photoanode have numerous boundaries and surface defects which limit charge transport. If the injected electrons get trapped in the mesoporous film, the electrons return to the oxidized dye or they reduce the triiodide as shown in **Processes (4) or (5)** respectively. This results in charge carrier recombination and consequently reduced PCE [10], [16].

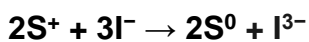


Process (4)



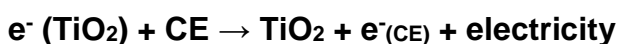
Process (5)

The iodide ion donates the electron that reduces the dye to ground state as represented by **Process (6)**:



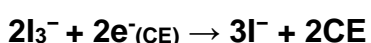
Process (6)

The injected electron travels through the mesoscopic metal oxide film towards the counter electrode (CE) and is simultaneously extracted to a load, causing the generation of electricity and this is presented by **Process (7)**.



Process (7)

Upon the electron reaching the counter electrode, the electron is transferred to the electrolyte which reduces the triiodide ion to iodide (**Process (8)**) which in turn regenerates the dye and therefore completing the circuit.



Process (8)

2.2.2 Characterizing key electrical parameters and efficiency

The performance of the DSSC device is determined by its overall power conversion efficiency, long term stability and cost. There are several techniques and methods that are used to fully understand the working principle and functions of the DSSCs. The basic and most common technique for characterizing solar cells is the Current-Voltage (I-V) curves. Other techniques such the Incident Photon Conversion Efficiency (IPCE) and electrochemical Impedance Spectroscopy (EIS) are also used. In order to compare the performances of solar cells, the I-V curve is measured under standardized conditions, under illumination of a lamp with a spectrum similar to AM 1.5G illumination. The I-V curve can also be measured under dark current to give information about charge carrier recombination [13] and asymmetric diode behaviour.

Typically, the following four parameters are deduced from the I-V curve and used to determine the performance of the cell: short circuit current (I_{sc}), open circuit voltage (V_{oc}), fill factor (FF) and energy conversion efficiency (η). These parameters are depicted in the current-Voltage plot below (**Figure 2.3**) followed by a brief description of each parameter [14-17].

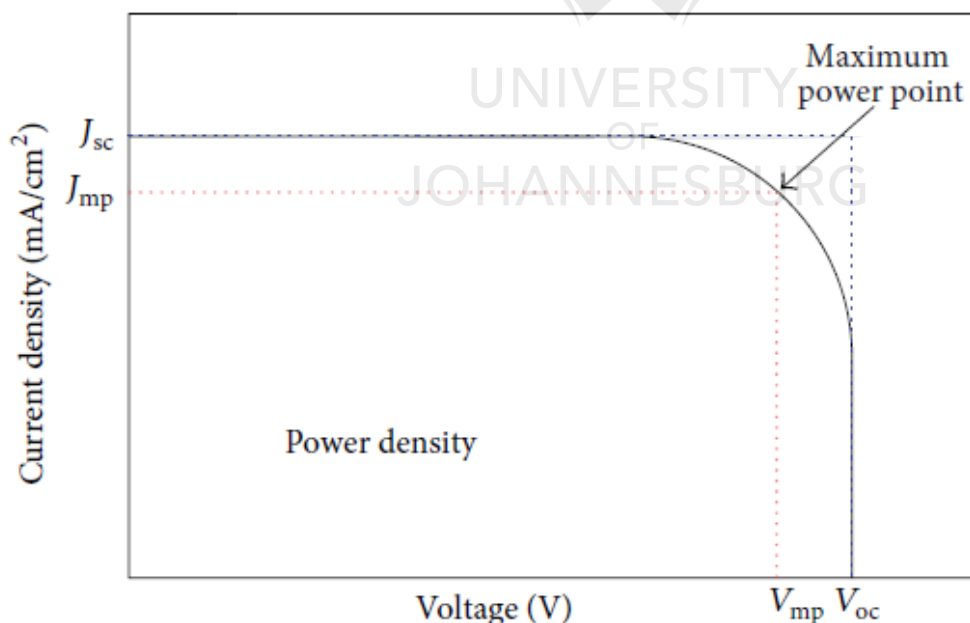


Figure 2.3: Typical I-V characteristic plot for solar cells

2.2.2.1 Short Circuit Current Density (J_{sc})

The short circuit current (I_{sc}) is the current obtained from the cell when the load resistance is zero. The I_{sc} largely depends on the generated electrons and the interfacial recombination of excitons. One major strategy to enhance the I_{sc} is to improve the light harvesting efficiency of the cell, which largely depends on:

- The concentration of the dye adsorbed on the TiO_2 film,
- The molar extinction coefficient of the dye and
- The optical path length of the incident light within the sensitized photoanode [18].

The short circuit current density (J_{sc}) is simply the I_{sc} normalized to the area of the cell and is represented by **equation 2.1**.

$$J_{sc} = \frac{I_{sc}}{A} \quad \text{Equation 2.1}$$

Where A is the effective area of the solar cell. This is a more useful parameter, since it allows for some comparisons to be made between similar devices irrespective of their effective surface areas or geometry.

2.2.2.2 Open Circuit Voltage (V_{oc})

V_{oc} is the maximum voltage in the cell under light illumination measured when the current is zero. V_{oc} depends on both the fermi levels of the semiconductor and the level of dark current. The theoretical maximum V_{oc} is determined by the difference between fermi levels of the semiconductor and the redox potential of the electrolyte. For DSSC, V_{oc} is given by:

$$V_{oc} = \frac{E_{CB}}{q} + \frac{kT}{q} \ln\left(\frac{n}{N_{CB}}\right) - \frac{E_{Redox}}{q} \quad \text{Equation 2.2}$$

Where, n and E_{CB} are the number of moles of electrons and the energy level of the conduction band of the semiconductor metal oxide respectively and N_{CB} is the effective density of states in the conduction band of the semiconductor oxide. The first two terms define the quasi-fermi level of the semiconductor metal oxide and E_{redox} is the Nernst potential of the redox mediator. The V_{oc} can therefore be improved by increasing the energy levels of the semiconductor conduction band, tuning the energy levels of the electrolyte to

lower energy levels, reducing the density of electron trap states and reducing the recombination rates [18].

2.2.2.3 Fill Factor (FF)

The FF is a measure of the quality of the cell and it is calculated by comparing the maximum power delivered to an external load to the theoretical power which will be output at both V_{oc} and J_{sc} . FF is calculated as:

$$FF = \frac{P_{max}}{P_{in}} = \left(\frac{J_{mp} \times V_{mp}}{J_{sc} \times V_{oc}} \right) \quad \text{Equation 2.3}$$

Where P_{max} and P_{in} are the maximum output power and input power from the sunlight measured in $mWcm^{-2}$, respectively. And J_{mp} and V_{mp} are the voltage and current density values at maximum power. Fill factor in DSSCs reflects the degree of electrical and electrochemical losses during cell operation [14-17].

2.2.2.4 Energy Conversion Efficiency (η)

The energy conversion efficiency of a solar cell is defined as the ratio of maximum electrical output to the energy input from the sun. Thus η is reported in percentage and is mathematically expressed as:

$$\eta = \frac{J_{sc} \times V_{oc} \times FF}{P_{in}} \quad \text{Equation 2.4}$$

Apart from the solar cell performance itself, the energy conversion efficiency depends on the incident light spectrum and intensity and the operating temperature. Solar cell efficiency is measured under the internationally recognised standard conditions under 'AM 1.5 Global' solar irradiation and at a temperature of 25 °C [14-17].

2.3 Components of the DSSCs

A DSSC is made up of three main components namely a photoelectrode, electrolyte and counter electrode. Each of these components is briefly described under this section.

2.3.1 Working Electrode

The photoelectrode is made up of a dye-adsorbed onto a semiconductor oxide materials that has been deposited onto a thin film layer of a transparent conducting oxide (TCO) substrate. Each of these parts play a vital role in the performance of the cell and are discussed in the sub-sections below.

2.3.1.1 Transparent Conducting oxide (TCO) Substrate

The TCO plays two major roles on the DSSC. It functions as a current collector and as a support structure for the cell as well as the sealing layer between the cell and the air. TCO substrates should have high optical transparency to allow sunlight to pass through without absorption of the unwanted solar spectrum. In addition, TCO substrates should have a low resistivity to facilitate efficient electron transfer processes and reduce energy loss through recombination reactions [5, 19].

Both organic and inorganic materials have been used for the fabrication of TCOs for photovoltaic applications. The inorganic films are usually made up of a layer of transparent conducting materials such as Fluorine doped tin oxide (FTO), Indium tin oxide (ITO) and doped zinc oxide. Fluorine-doped tin oxide (FTO) and indium doped tin oxide (ITO) on a glass substrate, are the most commonly used transparent conductive oxides for photovoltaic electrodes but because of the better thermal stability of FTO at high temperatures, scarcity and high cost of Indium; FTO is generally preferred in DSSCs [5, 19]. Organic films on the other hand, are fabricated using Carbon nanotube networks and graphene which can be tuned to be highly transparent to infrared light, along with networks of conducting polymers such as poly(3,4-ethylenedioxythiophene) and their derivatives [20].

2.3.1.2 Titania: Mesoporous Semiconductor Oxide Layer

The basic DSSC working electrode is usually assembled with a relatively high surface area mesoporous semiconductor metal oxide film for the chemisorption of the dye molecules. A mesoporous film of 10 – 12 μm thickness made up of 20 – 30 nm nanoparticles and porosity of 50% is able to absorb the entire incident light and achieve conversion efficiency of up to 11.2% [21]. The working electrode plays a vital role in electron transfer processes. The porosity and morphology of the metal oxide film are critical players in determining the amount of dye molecules the film will adsorb on its surface which in turn determines the cell performance.

Semiconductor metal oxides such as TiO₂, ZnO [22, 23] and SnO₂ [24, 25] have been widely studied as photoanodes due to their wide application in energy storage and environmental remediation. Among all the oxides, TiO₂ has been the material of choice in the DSSCs due to its favourable band gap, chemical stability, low toxicity and cost, and surface compatibility with various dyes [26]. Titanium dioxide exists in three natural polymorphs namely rutile, anatase and brookite. Among the three polymorphs, rutile is the most stable. Anatase is metastable and tend to convert to rutile upon heating to 450 °C - 500 °C. However, the anatase phase is more efficient in applications such as catalysis, photocatalysis and DSSCs [19, 27].

Titania, in the anatase phase, is the most commonly used photoanode material and it has a band gap of 3.2 eV. The minimum energy required to excite electrons from the valence band (VB) to the conduction band (CB) falls in the UV region of the electromagnetic spectrum which is only 5% of the solar spectrum that reaches the earth's surface. This means only a small percentage of the solar spectrum is used in the excitation of electrons. For the anatase phase of titania to utilise most of the solar spectrum, the dye/sensitizer molecules are required to extend the absorption spectrum in the visible and infrared regions [5].

2.3.1.3 Sensitizer/Dye

The dye molecules plays a critical role of sensitizing the semiconductor metal oxide to allow absorption of sunlight in the visible and IR regions. For this reason, the dye molecule should satisfy the following requirements [5, 6, 11, 28, 29]:

- (a) The energy levels of the dye molecules should match well with those of the semiconductor metal oxide and with the redox potential of the electrolyte.

The LUMO energy levels of the excited sensitizer molecule should be in the order of 0.2 – 0.3 eV above the CB of the TiO₂ to allow for efficient charge injection. This will prevent electron recombination from CB of TiO₂ to the excited dye molecules and only allow dye regeneration by the electrolyte.

- (b) The ideal sensitizer should have a broad absorption spectrum (800 nm – 400 nm).

The amount of light that is absorbed by the sensitizer depends on the concentration of the dye on the surface of the TiO₂ film and the absorption coefficient of the dye. A sensitizer should therefore have a high absorption coefficient in the visible region as well as a high affinity towards TiO₂ to ensure a dense coverage of the dye on the TiO₂ surface and therefore ensure better light harvesting capability.

(c) The dye molecules should have a strong coupling of orbitals with the metal oxide for an effective injection of electrons in the CB of the metal oxide with a quantum yield close to unity.

(d) The dye molecules should be stable for over 20 years under sunlight.

The electron injection and electron regeneration in the sensitizer should ideally be reversible throughout the 20 years of operation. However, degradation of the sensitizers occurs in real devices but the rate of degradation should be minimal within those 20 years.

The dye monolayer is a very important part of the DSSC because it interacts with the sunlight. The Semiconductor metal oxide films are immersed in the dye solution for a period of 12 to 24 h for the dye molecules to adsorb on the surface of the metal oxide film. Ruthenium polypyridyl complexes especially N3 ($\eta > 10\%$) [8, 29] and N719 ($\eta > 12\%$) (**structures shown in Figure 2.4**) have so far been the most efficient sensitizers in terms of photovoltaic performance and cell stability.

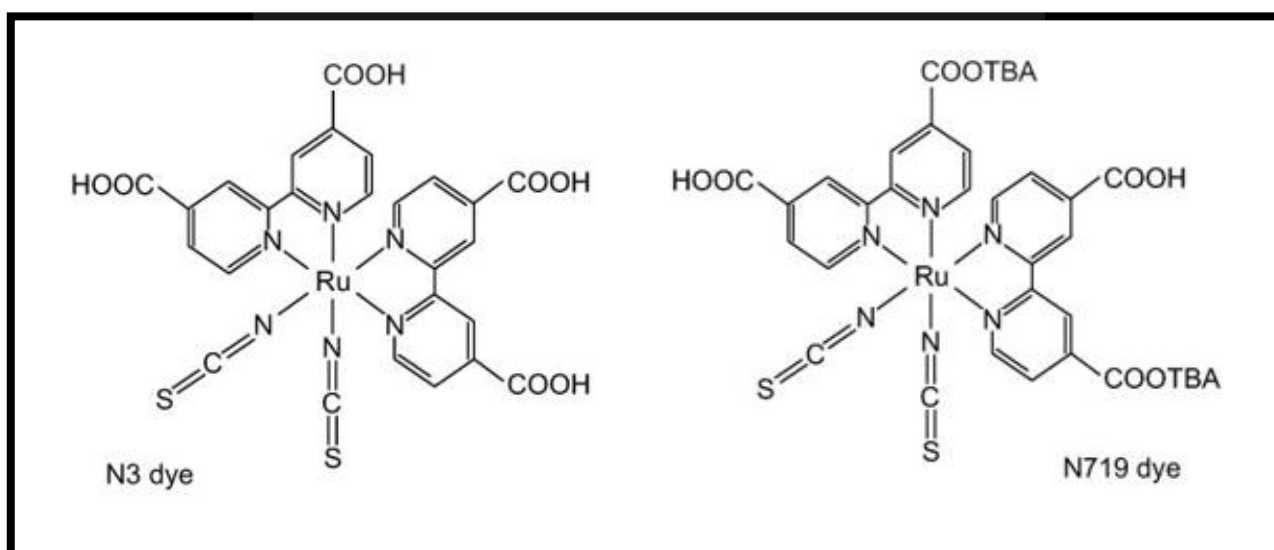


Figure 2.4: Structures of N3 and N719 dyes

The ruthenium polypyridyl complexes have strong absorption in the visible region, long excitation lifetime and efficient metal to ligand charge transfer. However, factors such as high costs, sophisticated synthesis and purification processes of ruthenium based dyes as well as limited availability of noble materials, have hindered their use for large scale production of DSSCs [5, 11, 30]. Several sensitizing molecules such as organic dyes ($\eta = 9.5\%$ for Porphyrin dyes) [28, 31] and natural dyes ($\eta = 1.5\%$ for Anthocyanins extracted from raspberries) [27, 32] have shown promising results in DSSC but still lag behind the ruthenium based dyes in terms of photovoltaic performances.

2.3.2 Electrolyte

The electrolyte is one of the key components of the DSSCs which plays an important role in the light to electricity conversion process. The electrolyte enables the electron transfer mechanism and kinetics and in turn facilitates the regeneration of the dye molecules. The recombination losses occurring in the cells depends on the charge transfer kinetics [5]. Thus the electrolyte plays an important role in the regulation of charge transfer kinetics and thus affecting the overall cell performance and the long term stability of the DSSC devices. The efficiency of the device is determined by the J_{SC} , V_{OC} and FF and all these parameters are significantly affected by the electrolyte in the DSSC as well as the interaction of the electrolyte with the electrode interfaces.

For example, the transport of the redox couple components in the electrolyte can affect the J_{SC} . The FF can be affected by the diffusion of charge carrier in electrolyte and the charge transfer resistance on the electrolyte / electrode interface. While the redox potential of the electrolyte significantly affect the V_{OC} [33].

An efficient electrolyte must meet the following characteristics [33-36]:

- (a) The redox potential of a redox couple should be less negative than the oxidized level of a dye molecules in order to maximize the photovoltage.
- (b) Chemically inert system
- (c) The electrolytes must have both chemical, thermal, optical, electrochemical and interfacial long-term stabilities and not cause desorption and degradation of the sensitized dye.
- (d) Highly reversible couple to allow fast electron transfer and avoid recombination.
- (e) The electrolytes should not exhibit a significant absorption in the visible light range.

- (f) The electrolytes must guarantee fast diffusion of charge carriers and produce good interfacial contact with the mesoporous semiconductor layer and with the counter electrode. For liquid electrolytes, the solvent should have smaller leakage and/or evaporation to prevent long term stability issues.

The iodide/triiodide (I^-/I_3^-) redox couple has been used mainly since the advent of DSSC research and has proven to be one of the most useful redox couples thus far with overall conversion efficiencies of up to 12%. The best performance of the I^-/I_3^- redox couple is mainly due to the favourable penetration into the nanocrystalline semiconductor film, very fast dye regeneration and relatively slow recombination losses. However, disadvantages such as [37].

- (a) The corrosiveness of iodine towards metals which are used as current collectors in some DSSCs;
- (b) iodine has a relatively high vapour pressure, which makes proper closing of the cells challenging;
- (c) the I_3^- ion absorbs a significant part of visible light, taking a percentage of photons away from the sensitizer molecules;
- (d) the redox potential of the I^-/I_3^- limits the photovoltage

Alternative electrolytes such as cobalt polypyridine complexes, room temperature ionic liquids (RTILs), Quasi-solid electrolyte and others [19], have been researched and studied however, although they offer advantages in terms of long term stability, they still lag behind the iodide/triiodide redox couple in terms of conversion efficiency [38].

2.3.3 Counter Electrode

The platinum coated FTO glass substrate is usually used as a counter electrode for the DSSC. The main functions of the counter electrode are to collect electrons coming from the external circuit and the regeneration of the electrolyte. When the oxidized electrolyte diffuses towards the counter electrode, the electrolyte gets reduced by accepting electrons from the external circuit. This reaction requires a catalyst to accelerate the reduction reaction and platinum has been the preferred catalyst because of its good catalytic activity, stability, high exchange current density, low electrical resistance and transparency [27, 39, 40].

The performance of the counter electrode depends on the method used for the preparation and deposition of platinum on the substrate. The catalytic activity of the platinum catalyst decreases over time in the presence of the iodide/triiodide redox couple and this is mainly

because of the changes in the electrocatalytic properties of platinum and the removal of platinum from the substrate. Although the platinum counter electrode possesses high catalytic activity and yields higher energy conversion efficiencies for the DSSCs, its usage is limited by higher costs, resource scarcity, high sintering temperatures and instability in redox electrolyte. As such other counter electrode catalysts such as carbonaceous materials such as amorphous carbon ($\eta = 5.6\%$ vs $\eta = 6.7\%$ for Pt) (Veerappan et al., 2012), graphene ($\eta = 5.73\%$ vs $\eta = 6.89\%$ for Pt) [41] and carbon nanotubes ($\eta = 7.67\%$ vs $\eta = 7.83\%$ for Pt) [42] and conductive polymers eg PANI ($\eta = 6.54\%$ vs $\eta = 6.89\%$ for Pt) [43] have been used as alternatives due to their low cost, chemical stability and good catalytic properties [44, 45]. However, their energy conversion efficiencies were lower than those of the platinum catalyst.

2.4 Mesoporous Materials

Mesoporous materials are solid materials with either ordered or disordered networks with broad or narrow pore distributions ranging between 2 – 50 nm as classified by IUPAC, where porous materials are classified as either:

Micropore has diameters < 2 nm

Mesopore has diameters ranging from 2 – 50 nm

Macropore has diameters > 50 nm

The pores of the mesoporous materials can be cylindrical or spherical, arranged in varying structures such as hexagonal, cubic or lamellar. Mesoporous materials of varying compositions such as SiO_2 , TiO_2 , mesoporous carbon and other metal oxides have been prepared from nanocasting or soft template pathways. The interest, especially in ordered mesoporous materials (OMMs), has grown tremendously over the years because of their potential for use in a wide range of applications [46-48]. Mesoporous materials have relatively large pores, thus can have large surface areas (good for dye sorption), excellent kinetics and therefore meets the essential features of an efficient working electrode of the DSSC [49]. Ordered Mesoporous Silica (OMS) is one of the mesoporous materials, which have been widely studied for several applications [46-48].

2.4.1 Ordered Mesoporous Silica (OMS)

OMS are materials which can be synthesized by using ionic and non-ionic surfactants or copolymers supramolecular assemblies in acidic media via a sol-gel method. Upon addition of the silica precursors, silica walls grew around the self-assembled template forming ordered mesoporous solids with narrow distributed pore sizes of different shapes such as cylindrical or cubic and arranged in hexagonal, cubic or lamellar structures. These pore structures are shown in **Figure 2.5** [46, 48].

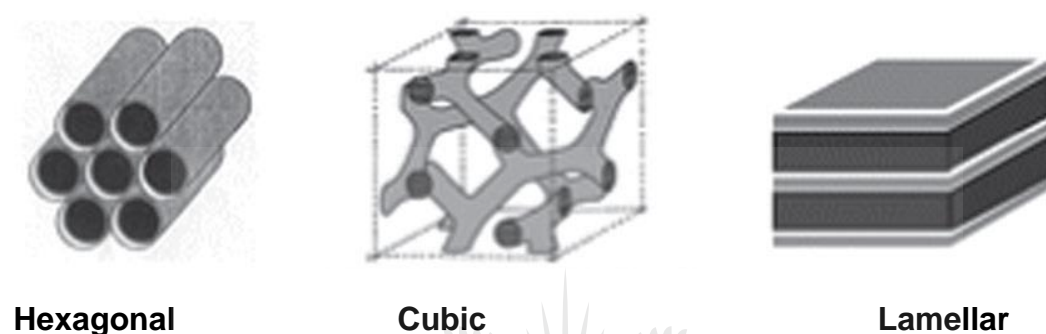


Figure 2.5: Pore structures of Ordered Mesoporous Silica.

OMMs have received a lot of research interest because of their ordered and interconnected pore structures, highly uniform pore size distribution, high specific areas, high mechanical and thermal stability, tunable pore sizes and high adsorption capacity. Another important aspect that has raised interest in OMMs is the possibility of modifying the physicochemical properties of OMMs by incorporation of organic and inorganic oxides, either in the mesopore walls or within the pore channels, resulting in materials of advanced properties with wide applications [46, 50]. These properties make OMMs suitable for diverse applications such as catalysis, adsorption, separation, drug delivery, photocatalysis, sensors, pollutant remediation and energy storage and conversion [47].

One of the common class of OMS is SBA-X (Santa Barbara Amorphous) which was developed by Zhao et al. and synthesized using triblock copolymers as surfactants. The X corresponds to a specific pore structure and surfactant used. Materials with variety pore arrangements such as SBA-1 (cubic), SBA-11 (cubic), SBA-12 (3D hexagonal network), SBA-14 (lamellar), SBA-15 (2D hexagonal) and SBA-16 (cubic cage-structured) have been prepared and reported in literature [51, 52]. Because of its desirable features such as high

surface areas, high thermal stability, high pore volumes and dual porosities, SBA-15 attracted a lot of research interests and it is also the focus of this research project.

2.4.2 SBA-15

SBA-15 is a combined mesoporous and microporous silica composed of uniform, two dimensional hexagonal mesopores typically ranging from 5 – 12 nm in diameter and micropores ranging between 0.5 – 3 nm. SBA-15 is commonly synthesized through an acid catalysed sol-gel method, using the amphiphilic triblock copolymers poly(ethylene glycol)–poly(propylene glycol)–poly(ethylene glycol) (PEO–PPO–PEO) as structure-directing and pore forming agent [51, 53, 54].

Each mesopore in the SBA-15 framework is surrounded by a microporous network called the corona and this network interconnects the mesopores with each other. The micropores in the wall of SBA-15 comes from the more hydrophilic EO chains of the surfactant, which penetrate the silica wall during synthesis and leaves micropores after calcination . The dual porosity systems as well as features such as high surface area (500 – 1000 cm²/g), high porosity, controllable and narrowly distributed pore sizes and good mechanical and thermal stability make SBA-15 materials very attractive for various applications such as catalysis, adsorption and separation, biosensing and energy storage and conversion [55-57].

The synthesis of SBA-15 is a three step process. The first step is the formation of the mesoporous structure using the triblock copolymer (surfactant) and silica precursors. The second step is the hydrothermal treatment at moderate temperatures and finally the removal of the surfactant from the material using calcination or solvent extraction techniques. Various reaction parameters such as pH, hydrolysis and aging temperatures and time, addition of swelling agents and surfactant to silica precursor ratio can be varied during these steps to tune the morphology as well as pore sizes of the SBA-15 [58]. SBA-15 has been found to be a suitable mesoporous silica for incorporation of metals and metal oxides which results in nanostructured composites with combined properties of the mesoporous silica and metal oxides. Because of the superior properties of the nanostructured composites, the composites have been studied in various applications such as photocatalysis and photovoltaic devices with promising results [56, 59-61].

2.5 Recent development in working electrodes

A DSSC is an electrochemical cell made up of three main components: the working electrode, counter electrode and the electrolyte. Each of these components plays a vital role in the whole device system and there have been several developments for each part to optimize the power conversion efficiency. These developments include the application of various nanomaterials and nanostructures in the working and counter electrodes, the design and application of novel dyes which have broader absorption spectra and high extinction coefficient and the synthesis of electrolyte to obtain high V_{oc} and long term stability. Among these developments, optimizing the morphology of the working electrode by using various nanomaterials and nanostructures has been considered to be the most effective way of improving the power conversion efficiency. Research has therefore been extensively focused on the application of novel nanostructures on the working electrode of the DSSC [12, 49].

The basic working electrode film is made of large Surface Area anatase phase of TiO_2 nanoparticles of sizes ranging from 15 – 30 nm. The high surface areas of the nanoparticles is suitable for high dye molecule loading. However, the low electron mobility of the anatase phase of TiO_2 , as well as the grain boundaries and defects at the contacts between the nanoparticles and the three dimensional random via the disordered nanoparticle network, inhibits the electron transport which results in enhanced charge carrier recombination [62]. Charge carrier recombination negatively affect the power conversion efficiency of the DSSC device.

In order to increase the overall conversion efficiency of the DSSC, the following features are essential for the working electrode. First, a large internal surface area for the electrode is required for high dye loading which will result in a higher light harvesting capability. Second, the injected electrons from the dye molecules must be transported to the external circuit with the highest efficiency to decrease recombination reaction between the oxidized species in the electrolyte and holes in the dye molecule. Third, for efficient binding of the dye molecules as well as efficient diffusion of the electrolyte, the working electrode (WE) should have sufficient porosity. And lastly, the materials in the WE should introduce the scattering function that will lengthen the light pathway and in turn improve the light harvesting properties [49].

The highest achieved efficiency for the DSSC is 13% which is still below the minimum theoretical limit and therefore requires improvement. Thus far, cell efficiency improvement

has been achieved either through improving light harvesting capability or by reducing exciton recombination or through a combination of the two. Approaches studied for improving light harvesting capability of the cell include development of alternative dyes with broader absorption solar spectrum and high molar extinction coefficients [63, 64], co-sensitization [65], plasmonic enhancement [66, 67] and incorporation of scattering particles [68, 69]. While improvement in cell efficiency by reducing recombination was achieved by post and pre-treatment of the TiO₂ film [70, 71], introducing a blocking layer on the FTO [72] and co-adsorbants in the electrolyte [73]. This review focused on improving the conversion efficiency by using the light scattering approach.

2.5.1 The Light Scattering Approach

The light scattering approach is used in DSSCs to enhance the probability of interaction between the photons and dye molecules which consequently improves the conversion efficiency of the cell. The common method of light scattering in DSSCs is by depositing a layer of large sized particles with diameters comparable to the wavelength of the incident light on the TiO₂ nanoparticle active layer. However, apart from this approach, nanomaterials can also be embedded in the active layer as light scatterers. Various nanostructures with good dye adsorption and light scattering properties such as core-shell and mesoporous materials have been used in the photoanode with promising results [4, 49, 69, 74, 75].

Recently, incorporation of large sized nanoparticles and porous nanostructures as light scattering materials in the TiO₂ film has attracted a lot of attention because light scatters lead to the dye molecules absorbing more photons and hence improve the efficiency of the cell. It has been reported that silica acts as an efficient light scattering material for improving the light harvesting capability of the cell due to the high difference in refractive index of silica and Titania. Silica has been used as either the core or shell or support material due to its rich surface chemistry, easy preparation methods, high adsorption capacity, optical transparency in the visible region and high thermal and mechanical stability [76].

Incorporation of mesoporous nanostructured materials in the WE have shown promising results because mesoporous materials have large surface area to volume ratios suitable for high dye loading; ordered and interconnected continuous mesopores for efficient electron transport and electrolyte diffusion. And because of the submicron particles, the mesoporous nanostructured materials introduce optical confinement leading to introduction of additional light scattering mechanism. Therefore, a mesoporous nanostructure meets all the features

of a WE for highly efficient DSSCs. Mesoporous nanostructures have therefore been synthesized and applied in the WE of the DSSCs with the aim of improving the cell efficiency as well as the overall characteristics of the cell.

Gajjela *et al.* synthesized mesoporous TiO₂ using various cationic surfactants as structure directing agents. The synthesized mesoporous TiO₂ exhibited high surface areas around 90 – 135 m²/g with uniform pore sizes in the range 5.7 – 7.0 nm. The mesoporous TiO₂ were used as photoelectrodes in DSSCs. The highest efficiency achieved using the synthesized mesoporous TiO₂ was 7.5 % in contrast to the 5.0 % of the commercial P25. This high efficiency of the mesoporous TiO₂ was attributed to the enhanced light scattering owing to large amount of dye adsorbed due to the large surface area and large pore sizes which provided easy access to the electrolyte [77].

Yun *et al.* investigated the effect of the pore size of mesoporous anatase TiO₂ on the photovoltaic performance of DSSCs. They prepared mesoporous TiO₂ particles by different methods, using soft and hard templates which resulted in mesoporous particles with same surface areas but different pore sizes of 6.8 and 3.0 nm respectively which were then applied as photoanodes in the DSSCs. The mesoporous TiO₂ having larger pores resulted in a high photo conversion efficiency of 6.74 % in comparison to 5.62 % typically achieved using the commercial P25 TiO₂ nanopowders. In contrast, the mesoporous TiO₂ with smaller pore sizes resulted only in 3.05 % efficiency. The high conversion efficiency for the large pore mesoporous TiO₂ was attributed to the high surface area which allowed for high dye uptake and in turn enhanced the current density. In contrast, the low efficiency of mesoporous TiO₂ with small pores is attributed to the low uptake of the dye molecules due to the smaller pore size (~3.0 nm), which blocked the diffusion and adsorption of dye molecules through the small pores [78].

Ahmed *et al.* synthesized highly crystalline mesoporous anatase phase of TiO₂ through supramolecular self-assembly using cetyltrimethylammonium bromide (CTAB) as structure directing agent and applied them in the photoanodes of the DSSCs. The photoanodes made of the synthesized mesoporous TiO₂ showed a high specific surface area of 153 m² /g and high surface roughness. Optical absorption spectroscopy studies revealed that the photoanode films adsorbed four times more dye molecules than commercial P25 TiO₂ film. While the electrochemical impedance studies revealed that the photoanodes which had both the mesopores and macropores had lower impedance and higher electron lifetime than the

P25 TiO₂ photoanodes. The devices performance evaluation results revealed the highest efficiency of 4.22 % of the synthesized mesoporous TiO₂ cells compared to the 3.16 % of the P25 cells. The enhancement in efficiency was attributed to the improved photoelectron production, resulting from the high surface area and surface roughness [79].

As revealed from the research studies above, mesoporous structures that have interconnected networks and high specific surface areas have shown superior advantages when applied in the working electrodes of the DSSCs. This is because they lead to improved characteristics such as dye loading, electron transport, electrolyte diffusion and light scattering, as compared to the typical nanoparticle electrodes. However, one should also bear in mind that an electrode made up of a mesoporous structure does not only provide a high surface area and an efficient electrolyte permeation but also enhances electron recombination with the electrolyte, resulting in a lower V_{OC} than a nanoparticle electrode [78].

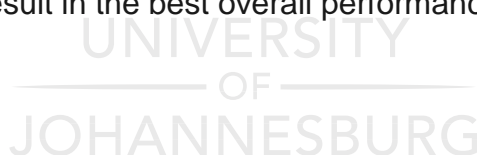
Therefore, key factors which control the optimum conditions of mesoporous working electrodes have been identified. These key factors are porosity and pore sizes of the electrodes, the crystallinity of the mesoporous electrode and the ordering of the mesoporous structure. The porosity and pore size of the working electrodes affect the surface area of the electrode that is available for dye loading and interfacial charge transfer with the electrolytes related to the regeneration of the excited dye molecules and charge carrier recombination. A mesoporous working electrode with a porosity above the optimum value has a lower surface area available for dye loading which leads to negative effects on the photocurrent [80].

The other key factor in DSSC performance is the crystallinity of the mesoporous photoanode. The semiconductor oxide photoanode should be able to efficiently transport the electrons injected from the dye molecules as fast as possible to the transparent conducting oxide on glass substrate in order to reduce recombination of electrons with the redox couple. The electron transport efficiency increases with increasing crystallinity which is achieved by high annealing temperatures of the film [49, 81]. Guldin *et al.* investigated the effect of crystallinity on conductivity and the electron transport properties of mesoporous TiO₂ photoanodes by annealing the mesoporous TiO₂ at different temperatures (400 – 700 °C). Mesoporous TiO₂ was synthesized using the PI-*b*-PEO as a structure directing agent to prevent the mesoporous structure from collapsing at high temperatures and applied the synthesized mesoporous TiO₂ in the photoanode, to investigate the effect of crystallinity on DSSC performance in both liquid DSSs and solid state DSSCs. They found that the anatase

conductivity was significantly improved by high temperature sintering which in turn resulted in reduced specific area of the mesoporous film. The lower specific surface area resulted in detrimental effects on the liquid DSSC performance while the solid state DSSC performance was enhanced threefold due to improved anatase conductivity at high crystallinity [81].

Zhang *et al.* investigated the influence of the ordered and disordered mesoporous TiO₂ on the performance of the DSSC. They used the supramolecular template method using Pluronic F127 to synthesize ordered body-centred orthorhombic and disordered worm-hole-like mesoporous TiO₂ and studied the effect of ordered and disordered morphologies on the devices performances. The results revealed that the DSSC composed of highly ordered mesoporous TiO₂ revealed higher J_{SC} and power conversion efficiency than the cell based on disordered mesoporous TiO₂. The V_{OC} of both devices were similar due to similar dye loading, therefore, higher J_{SC} could be attributed to the enhanced electron transport through the highly ordered mesoporous TiO₂ network [82]. These results demonstrated the importance of the ordering of the mesoporous working electrode network on the performance of the DSSC device.

It is therefore important to control the pore sizes, porosity, crystallinity and ordering in the mesoporous working electrode of the DSSC to obtain optimum performance of the working electrodes which will then result in the best overall performance of the DSSC devices.



2.6 REFERENCES

1. Nazeeruddin, M. K.; Baranoff, E.; Grätzel, M. *Solar energy* **2011**, 85, (6), 1172-1178.
2. Maçaira, J.; Andrade, L.; Mendes, A. *Renewable and Sustainable Energy Reviews* **2013**, 27, 334-349.
3. Gonçalves, L. M.; de Zea Bermudez, V.; Ribeiro, H. A.; Mendes, A. M. *Energy & Environmental Science* **2008**, 1, (6), 655-667.
4. Deepak, T.; Anjusree, G.; Thomas, S.; Arun, T.; Nair, S. V.; Nair, A. S. *RSC Advances* **2014**, 4, (34), 17615-17638.
5. Reddy, K. G.; Deepak, T.; Anjusree, G.; Thomas, S.; Vadukumpully, S.; Subramanian, K.; Nair, S. V.; Nair, A. S. *Physical Chemistry Chemical Physics* **2014**, 16, (15), 6838-6858.
6. Lee, J.-K.; Yang, M. *Materials Science and Engineering: B* **2011**, 176, (15), 1142-1160.
7. Deb, S. K. *Solar Energy Materials and Solar Cells* **2005**, 88, (1), 1-10.
8. Rho, W.-Y.; Jeon, H.; Kim, H.-S.; Chung, W.-J.; Suh, J. S.; Jun, B.-H. *Journal of Nanomaterials* **2015**, 2015, 85.
9. O'regan, B.; Gratzel, M. *nature* **1991**, 353, (6346), 737-740.
10. Bella, F.; Gerbaldi, C.; Barolo, C.; Grätzel, M. *Chemical Society Reviews* **2015**, 44, (11), 3431-3473.
11. Kong, F.-T.; Dai, S.-Y.; Wang, K.-J. *Advances in OptoElectronics* **2007**, 2007.
12. Grätzel, M. *Accounts of chemical research* **2009**, 42, (11), 1788-1798.
13. Al-Alwani, M. A. M.; Mohamad, A. B.; Ludin, N. A.; Kadhum, A. A. H.; Sopian, K. *Renewable and Sustainable Energy Reviews* **2016**, 65, 183-213.
14. Chen, M.; Shao, L.-L. *Chemical Engineering Journal* **2016**, 304, 629-645.
15. Chang, H.; Wu, H. M.; Chen, T. L.; Huang, K. D.; Jwo, C. S.; Lo, Y. J. *Journal of Alloys and Compounds* **2010**, 495, (2), 606-610.
16. Jasim, K. E.; Al-Dallal, S.; Hassan, A. M. *International Journal of Nanoparticles* **2011**, 4, (4), 359-368.
17. Ludin, N. A.; Mahmoud, A. A.-A.; Mohamad, A. B.; Kadhum, A. A. H.; Sopian, K.; Karim, N. S. A. *Renewable and Sustainable Energy Reviews* **2014**, 31, 386-396.
18. Zhang, S.; Yang, X.; Numata, Y.; Han, L. *Energy & Environmental Science* **2013**, 6, (5), 1443-1464.
19. Gong, J.; Liang, J.; Sumathy, K. *Renewable and Sustainable Energy Reviews* **2012**, 16, (8), 5848-5860.

20. Hecht, D. S.; Hu, L.; Irvin, G. *Advanced Materials* **2011**, 23, (13), 1482-1513.
21. Grätzel, M. *Journal of Photochemistry and Photobiology A: Chemistry* **2004**, 164, (1), 3-14.
22. Zhang, Q.; Dandeneau, C. S.; Zhou, X.; Cao, G. *Advanced Materials* **2009**, 21, (41), 4087-4108.
23. Xu, F.; Sun, L. *Energy & Environmental Science* **2011**, 4, (3), 818-841.
24. Ramasamy, E.; Lee, J. *The Journal of Physical Chemistry C* **2010**, 114, (50), 22032-22037.
25. Dou, X.; Sabba, D.; Mathews, N.; Wong, L. H.; Lam, Y. M.; Mhaisalkar, S. *Chemistry of Materials* **2011**, 23, (17), 3938-3945.
26. Bagheri, S.; Hir, Z. A. M.; Yousefi, A. T.; Hamid, S. B. A. *Microporous and Mesoporous Materials* **2015**, 218, 206-222.
27. Shalini, S.; Prasanna, S.; Mallick, T. K.; Senthilarasu, S. *Renewable and Sustainable Energy Reviews* **2015**, 51, 1306-1325.
28. Shalini, S.; Balasundaraprabhu, R.; Kumar, T. S.; Prabavathy, N.; Senthilarasu, S.; Prasanna, S. *International Journal of Energy Research* **2016**.
29. Hagfeldt, A.; Boschloo, G.; Sun, L.; Kloo, L.; Pettersson, H. *Chemical reviews* **2010**, 110, (11), 6595-6663.
30. Robertson, N. *Angewandte Chemie International Edition* **2006**, 45, (15), 2338-2345.
31. Yella, A.; Lee, H.-W.; Tsao, H. N.; Yi, C.; Chandiran, A. K.; Nazeeruddin, M. K.; Diao, E. W.-G.; Yeh, C.-Y.; Zakeeruddin, S. M.; Grätzel, M. *science* **2011**, 334, (6056), 629-634.
32. Alhamed, M.; Issa, A. S.; Doubal, A. W. *Journal of electron Devices* **2012**, 16, (11), 1370-1383.
33. Wu, J.; Lan, Z.; Lin, J.; Huang, M.; Huang, Y.; Fan, L.; Luo, G. *Chemical reviews* **2015**, 115, (5), 2136-2173.
34. Wolfbauer, G.; Bond, A. M.; Eklund, J. C.; MacFarlane, D. R. *Solar energy materials and solar cells* **2001**, 70, (1), 85-101.
35. Wu, J.; Lan, Z.; Hao, S.; Li, P.; Lin, J.; Huang, M.; Fang, L.; Huang, Y. *Pure and Applied Chemistry* **2008**, 80, (11), 2241-2258.
36. Clifford, J. N.; Palomares, E.; Nazeeruddin, M. K.; Grätzel, M.; Durrant, J. R. *The Journal of Physical Chemistry C* **2007**, 111, (17), 6561-6567.
37. Chung, I.; Lee, B.; He, J.; Chang, R. P.; Kanatzidis, M. G. *Nature* **2012**, 485, (7399), 486-489.

38. Sönmezoğlu, S.; Akyürek, C.; Akin, S. *Journal of Physics D: Applied Physics* **2012**, 45, (42), 425101.
39. Kim, S.-S.; Nah, Y.-C.; Noh, Y.-Y.; Jo, J.; Kim, D.-Y. *Electrochimica Acta* **2006**, 51, (18), 3814-3819.
40. Xu, S.; Luo, Y.; Zhong, W. *Solar energy* **2011**, 85, (11), 2826-2832.
41. Wu, M.; Ma, T. *The Journal of Physical Chemistry C* **2014**, 118, (30), 16727-16742.
42. Lee, W. J.; Ramasamy, E.; Lee, D. Y.; Song, J. S. *ACS applied materials & interfaces* **2009**, 1, (6), 1145-1149.
43. Tai, Q.; Chen, B.; Guo, F.; Xu, S.; Hu, H.; Sebo, B.; Zhao, X.-Z. *Acs Nano* **2011**, 5, (5), 3795-3799.
44. Wu, K.; Chen, L.; Duan, C.; Gao, J.; Wu, M. *Materials & Design* **2016**, 104, 298-302.
45. Veerappan, G.; Bojan, K.; Rhee, S.-W. *Renewable Energy* **2012**, 41, 383-388.
46. Walcarius, A. *Chemical Society Reviews* **2013**, 42, (9), 4098-4140.
47. Deng, Y.; Wei, J.; Sun, Z.; Zhao, D. *Chemical Society Reviews* **2013**, 42, (9), 4054-4070.
48. Linares, N.; Silvestre-Albero, A. M.; Serrano, E.; Silvestre-Albero, J.; Garcia-Martinez, J. *Chemical Society Reviews* **2014**, 43, (22), 7681-7717.
49. Ye, Y.; Jo, C.; Jeong, I.; Lee, J. *Nanoscale* **2013**, 5, (11), 4584-4605.
50. Wan, Y.; Zhao, D. *Chemical reviews* **2007**, 107, (7), 2821-2860.
51. Meynen, V.; Cool, P.; Vansant, E. *Microporous and mesoporous materials* **2009**, 125, (3), 170-223.
52. Zhao, D.; Feng, J.; Huo, Q.; Melosh, N.; Fredrickson, G. H.; Chmelka, B. F.; Stucky, G. D. *science* **1998**, 279, (5350), 548-552.
53. Kruk, M.; Jaroniec, M.; Joo, S. H.; Ryoo, R. *The Journal of Physical Chemistry B* **2003**, 107, (10), 2205-2213.
54. Zhang, Z.; Melián-Cabrera, I. *The Journal of Physical Chemistry C* **2014**, 118, (49), 28689-28698.
55. Stevens, W. J.; Lebeau, K.; Mertens, M.; Van Tendeloo, G.; Cool, P.; Vansant, E. F. *The Journal of Physical Chemistry B* **2006**, 110, (18), 9183-9187.
56. Zukerman, R.; Vradman, L.; Titelman, L.; Weidenthaler, C.; Landau, M. V.; Herskowitz, M. *Microporous and Mesoporous Materials* **2008**, 116, (1), 237-245.
57. Kruk, M.; Jaroniec, M.; Ko, C. H.; Ryoo, R. *Chemistry of materials* **2000**, 12, (7), 1961-1968.
58. Johansson, E. M.; Ballem, M. A.; Córdoba, J. M.; Odén, M. *Langmuir* **2011**, 27, (8), 4994-4999.

59. Bonne, M.; Pronier, S.; Can, F.; Courtois, X.; Valange, S.; Tatibouët, J.-M.; Royer, S.; Marécot, P.; Duprez, D. *Solid State Sciences* **2010**, 12, (6), 1002-1012.
60. Perathoner, S.; Lanzafame, P.; Passalacqua, R.; Centi, G.; Schlögl, R.; Su, D. S. *Microporous and Mesoporous Materials* **2006**, 90, (1), 347-361.
61. Lachheb, H.; Ahmed, O.; Houas, A.; Nogier, J. *Journal of Photochemistry and Photobiology A: Chemistry* **2011**, 226, (1), 1-8.
62. Zhu, K.; Neale, N. R.; Miedaner, A.; Frank, A. J. *Nano letters* **2007**, 7, (1), 69-74.
63. Yu, Q.; Liu, S.; Zhang, M.; Cai, N.; Wang, Y.; Wang, P. *The Journal of Physical Chemistry C* **2009**, 113, (32), 14559-14566.
64. Hwang, S.; Lee, J. H.; Park, C.; Lee, H.; Kim, C.; Park, C.; Lee, M.-H.; Lee, W.; Park, J.; Kim, K. *Chemical Communications* **2007**, (46), 4887-4889.
65. Singh, S. P.; Chandrasekharam, M.; Gupta, K. S.; Islam, A.; Han, L.; Sharma, G. *Organic Electronics* **2013**, 14, (5), 1237-1241.
66. Zarick, H. F.; Hurd, O.; Webb, J. A.; Hungerford, C.; Erwin, W. R.; Bardhan, R. *Acs Photonics* **2014**, 1, (9), 806-811.
67. Lin, S.-J.; Lee, K.-C.; Wu, J.-L.; Wu, J.-Y. *Applied Physics Letters* **2011**, 99, (4), 043306.
68. Wang, Y.; Chen, E.; Lai, H.; Lu, B.; Hu, Z.; Qin, X.; Shi, W.; Du, G. *Ceramics International* **2013**, 39, (5), 5407-5413.
69. Son, S.; Hwang, S. H.; Kim, C.; Yun, J. Y.; Jang, J. *ACS applied materials & interfaces* **2013**, 5, (11), 4815-4820.
70. Sommeling, P.; O'regan, B.; Haswell, R.; Smit, H.; Bakker, N.; Smits, J.; Kroon, J.; Van Roosmalen, J. *The Journal of Physical Chemistry B* **2006**, 110, (39), 19191-19197.
71. O'Regan, B. C.; Durrant, J. R.; Sommeling, P. M.; Bakker, N. J. *The Journal of Physical Chemistry C* **2007**, 111, (37), 14001-14010.
72. Heo, J.; Sudhagar, P.; Park, H.; Cho, W.; Kang, Y. S.; Lee, C. *Journal of Thermal Spray Technology* **2015**, 24, (3), 328-337.
73. Song, B. J.; Song, H. M.; Choi, I. T.; Kim, S. K.; Seo, K. D.; Kang, M. S.; Lee, M. J.; Cho, D. W.; Ju, M. J.; Kim, H. K. *Chemistry—A European Journal* **2011**, 17, (40), 11115-11121.
74. Yang, C.-C.; Zheng, Y. R. *Journal of Power Sources* **2012**, 201, 387-394.
75. Tanvi; Mahajan, A.; Bedi, R. K.; Kumar, S.; Saxena, V.; Aswal, D. K. *Chemical Physics Letters* **2016**, 658, 276-281.

76. Ullah, S.; Ferreira-Neto, E. P.; Pasa, A. A.; Alcântara, C. C.; Acuna, J. J.; Bilmes, S. A.; Ricci, M. L. M.; Landers, R.; Fermino, T. Z.; Rodrigues-Filho, U. P. *Applied Catalysis B: Environmental* **2015**, 179, 333-343.
77. Gajjela, S. R.; Ananthanarayanan, K.; Yap, C.; Gratzel, M.; Balaya, P. *Energy & Environmental Science* **2010**, 3, (6), 838-845.
78. Yun, T. K.; Park, S. S.; Kim, D.; Hwang, Y.-K.; Huh, S.; Bae, J. Y.; Won, Y. S. *Journal of Power Sources* **2011**, 196, (7), 3678-3682.
79. Ahmed, S.; Du Pasquier, A.; Birnie III, D. P.; Asefa, T. *ACS applied materials & interfaces* **2011**, 3, (8), 3002-3010.
80. Benkstein, K. D.; Kopidakis, N.; Van de Lagemaat, J.; Frank, A. *The Journal of Physical Chemistry B* **2003**, 107, (31), 7759-7767.
81. Guldin, S.; Hüttner, S.; Tiwana, P.; Orilall, M. C.; Ülgüt, B.; Stefik, M.; Docampo, P.; Kolle, M.; Divitini, G.; Ducati, C. *Energy & Environmental Science* **2011**, 4, (1), 225-233.
82. Zhang, Y.; Xie, Z. *Interfaces* **2009**, 1, 2789-2795.



CHAPTER 3: EXPERIMENTAL

3. INTRODUCTION

Chapter 3 presents the experimental methods undertaken during this research project. The procedures and techniques used for the synthesis and characterization of the nanomaterials and nanocomposites as well as the application of these nanocomposites in the photoanodes of the DSSCs are presented in detail. Where characterization was done elsewhere, this has been duly acknowledged.

3.1 Chemicals and Materials

All chemicals were used as received, without further purification and deionized water was used throughout the project. The chemicals used for the synthesis of the nanomaterials and nanocomposites are listed in **Table 3.1**.

Table 3.1: List of chemicals used for the synthesis of nanomaterials and nanocomposites and their purities and suppliers.

Chemicals/Materials	Supplier	Purity
Titanium isopropoxide (C_3H_7O) ₄ Ti, TTIP	Sigma Aldrich, SA	
Tetraethoxy orthosilicate (C_2H_5O) ₄ Si, TEOS	Sigma Aldrich, SA	
Pluronic Ethylene oxide-propylene oxide-ethylene oxide (EO ₂₀ PO ₇₀ EO ₂₀), P123, M _w 5800	Sigma Aldrich, SA	
Hydrochloric Acid (HCl)	Merck	32 %
Ammonia (NH ₃)	Merck	25 %
Ethanol (C ₂ H ₅ OH)	Merck	99 %
Isopropanol (C ₃ H ₇ OH)	Merck	99 %
Formic Acid (HCO ₂ H)	Saarchem	85 %

The chemicals and materials used in the fabrication of the photoanode are listed in **Table 3.2**.

Table 3.2: List of Chemicals used for the fabrication of the DSSCs and their suppliers.

Chemicals/Materials	Supplier
Triton x-100	Sigma Aldrich ,SA
Polyethylene glycol, M_w 8000	Sigma Aldrich, SA
Ru Dye N719	Solaronix, Switzerland
Acetylacetone	Sigma Aldrich, SA
FTO coated glass electrodes, 2 mm thick, 15 Ω/sq	Solaronix, Switzerland
Iodolyte Z-150	Solaronix, Switzerland
Platisol T/SP	Solaronix, Switzerland

3.2 Characterization Techniques

The physical chemical and optical properties of the synthesized materials were studied using the following techniques: N₂ Desorption, TEM, SEM-EDS, FTIR, diffuse reflectance UV-Vis, and XRD. This section therefore focuses on the description of the techniques and instrument parameters used during the analysis of the materials.

3.2.1 Nitrogen Absorption-Desorption Isotherm Analysis

Nitrogen absorption-desorption at 77 K, is a characterization technique that is used for the determination of specific surface area, pore volume, pore size distribution and surface properties of porous materials [1, 2]. The textural properties of the materials were determined from N₂ Sorption technique at 77 K using a Micrometrics TRI STAR 3020V1.03 (V1.03) instrument. Samples were degassed with a Micrometrics Vacprep 061 sample degas system (USA). About 0.2 g of the sample was weighed into a clean glass sample tube then degassed at 90°C for 1 h under vacuum and thereafter the temperature was increased to 200 °C for 12 h. The temperature of the system was set back to 90 °C to allow the tube and content to gradually decrease to the set temperature. The tube and content was thereafter removed and placed in the cooling chamber and allowed to cool down to room temperature. The total surface area was calculated using the BET equation while the BJH model was used to determine the pore size distribution from the desorption branch of the isotherm. Sample analysis was done at the University of Kwa-Zulu Natal (UKZN), South Africa.

3.2.2 Fourier Transform Infrared Spectroscopy

Fourier transform infrared spectroscopy (FTIR) is a technique that is used to determine specific chemical functional groups present in a sample. The functional groups have characteristic vibrational frequencies depending on the atoms present in a bond, the number of bonds as well as the orientation of the bonds with respect to the rest of the molecule [3]. In order to investigate the functional groups of the nanomaterials and nanocomposites synthesized in this research project, the spectra were taken using a Perkin Elmer Spectrum 100 (USA) Spectrometer. Approximately 100 mg of sample was mixed and pulverised with 2000 mg of KBr and about 250 mg portion of this mixture was used to form pellets for analysis. The spectral range used was $4000\text{ cm}^{-1} - 400\text{ cm}^{-1}$.

3.2.3 Transmission Electron Microscopy

The microstructural properties of the synthesized materials were investigated using a Jeol JEM 2100 Transmission Electron Microscopy (TEM) operating at 200 kV. The images were taken using a Gatan digital Camera. The sample (~ 10 mg) was dispersed in 5 mL of ethanol with the aid of ultrasonication (UMC 5 Ultrasonic bath, Max Power: 100 W) for 10 min and a drop of the sample was deposited on a formvar carbon coated copper grid and the grid was allowed to dry before analysis. ImageJ software was used for particle size distribution (PSD) analysis. **Figure 3.1** below illustrates how the ImageJ software was used to determine the particle sizes of spherical (SiO_2).

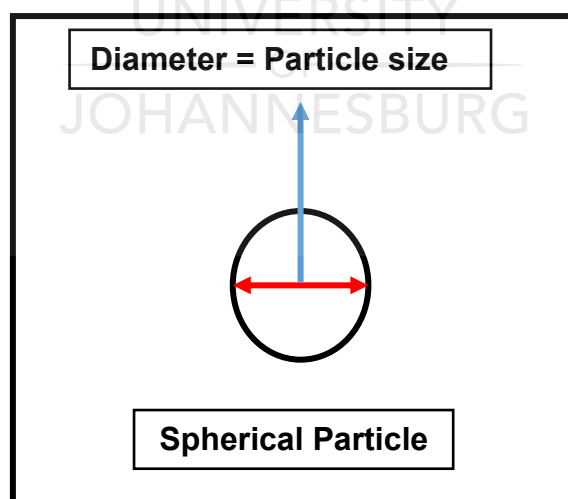


Figure 3.1: Illustration of how ImageJ software was used to determine the particle sizes of spherical particles.

3.2.4 Scanning Electron Microscopy

Scanning electron microscopy (SEM) is a technique that creates an image of the sample by scanning it with a beam of electrons. The beam of electrons interact with the atoms on the surface of the sample giving information about surface morphology and composition [4, 5]. A Vega 3 Tescan XMU SEM microscope was used to study the morphology of the materials. SEM measurements require sample surfaces to be electrically conductive and grounded to prevent electrostatic charging. Therefore, the samples were carbon coated first, using the Quorum Q150T E before SEM analysis. The elemental composition of the nanocomposites were confirmed using energy dispersive X-ray spectroscopy (EDS) coupled to SEM.

3.2.5 X-ray Diffraction (XRD)

The XRD technique is used to determine the structural properties such as crystal structure/phase, lattice parameters and crystallite sizes of the materials [3]. The XRD patterns were recorded by a PAnalytical X'pert Pro operating at 40 kV and 40 mA, with a Cu K α ($\lambda = 1.54056$ nm) radiation source. The instruments scanning range (2θ) was 10 – 90 degrees of 2θ , with a scan rate of 1.00 degree/min and step size of 0.010 degree. A library software, Highscore Plus PDF 4+ was used for data processing, identification and confirmation of the miller indices of the materials. The crystal sizes of TiO $_2$ were calculated using the Scherrer equation (**Equation 3.1**) [6] from the (101) anatase peak.

$$d = \frac{0.91 \lambda}{\beta \cos \theta}$$

Equation 3.1

Where d = crystal size, λ = the wavelength of the x-ray, β = full width at half maximum (FWHM) of the peak and θ = the diffraction angle [3].

3.2.6 Diffuse Reflectance Ultraviolet-Visible (DRS UV-Vis) Spectroscopy

The UV–Vis diffuse reflectance spectra were recorded by UV-Vis 2450 (Shimadzu Co. Ltd.) with an integrated sphere and using Barium Sulphate as a reference. The samples were analysed as they are, without mixing with Barium Sulphate. Both absorbance and reflectance were analysed at the wavelength ranging between 300 and 800 nm, with slit

width at 5 nm and the scanning speed set at medium. The respective band gap of each sample was calculated from the Kubelka-Munk (equation 3.2) [7, 8]:

$$K = \frac{(1 - R)^2}{2R} \quad \text{Equation 3.2}$$

Where R is the reflectance, while K is proportional to the extinction coefficient. In order to determine the band gap of each material, the $[K\text{h}\nu]^2$ (eV)² was plotted against $\text{h}\nu$ (eV). The intercept of the tangent line at the horizontal axis where $[K\text{h}\nu]^2 = 0$ is the band gap (E_g) value.

3.2.7 Raman Analysis

When a sample is illuminated with a monochromatic laser light, the light interacts with the molecules of the sample resulting in a scattered light having a frequency which is different from that of the incident light (inelastic scattering). It is this inelastic scattering that is used to construct the Raman spectrum and provides information about the vibrational, rotational and other low frequency transitions in a molecule [9]. The Raman Spectra of TiO₂ samples and the TiO₂/SiO₂ cores-shell nanostructures were obtained from A Perkin Elmer Raman Micro 200 with 785nm Argon laser and power output used was 50 mW. The sample was placed on a glass slide on the Olympus BX51M microscope with a 50x magnification, focussed to get the best image then switched from bright to dark field. A laser beam was focused on the sample and the spectrum was recorded. Several spots were analysed per sample. The samples were analysed without further preparation.

3.3 METHODOLOGY

This section focuses on the detailed description of the methods used to synthesize the TiO₂, Silica support materials (SiO₂ and SBA-15) and the Titania-Silica nanocomposites.

3.3.1 Synthesis of Titanium Dioxide Nanoparticles

Titanium dioxide nanoparticles were synthesized via a sol-gel method using TTIP as the Titania precursor. In a typical procedure, 8.30 g of TTIP was added to 48 mL of isopropanol in a beaker and the solution was mixed by stirring on a magnetic stirrer at 200 rpm for 20

min under the fume hood. To this solution, 12 mL of formic acid was added slowly and this resulted in the formation of a white precipitate which was continuously stirred at the same speed for another 4 h. The stirrer was switched off and the mixture was left to age for a further 4 h. The beaker containing the precipitate was placed in the oven at 80 °C, overnight, to evaporate the solvent and dry the sample. The as synthesized sample was then calcined in a porcelain boat at 500 °C using an Elite Thermal system (TSH12/38/500-2216E) tube furnace, using a heating rate of 10 °C/min. The furnace temperature was maintained at 500 °C for 3 h and thereafter, the sample was allowed to cool down slowly in the furnace.

3.3.2 Synthesis of silica support materials

3.3.2.1 Synthesis of the non-mesoporous Silica particles

The submicron SiO₂ particles were prepared by hydrolysis and condensation of TEOS in ethanol, using ammonia as a catalyst, following a modified Stober method [10, 11]. First, Solution A, consisting of ammonia, ethanol and deionised (DI) water with a volume ratio of 10:19:21 (10 mL: 19 mL: 21 mL respectively) was stirred vigorously in a beaker, using a magnetic stirrer at a high speed (1000 rpm) for 10 min. Solution B was prepared by mixing 5 mL of TEOS and 45 mL of Ethanol in a beaker and this solution was quickly poured into solution A under vigorous stirring which resulted in a gradual formation of a white precipitate. After vigorous stirring for 10 min, the speed was reduced to 400 rpm and the mixture was continuously stirred for another 2 h at ambient temperatures. The submicron SiO₂ samples were then collected by high speed centrifugation (Eppendorf Centrifuge 5702) operating at 4000 rpm for 10 min, washed three times with alcohol and the sample was dried at 80 °C overnight. This non-mesoporous silica support is hereafter referred to as SiO₂.

3.3.2.2 Synthesis of SBA-15

Two Mesoporous silica SBA-15 were prepared according to a verified procedure from Meynen *et al.* 2009, using tetraethyl orthosilicate (TEOS) as a silica precursor and triblock co-polymer poly(ethylene glycol)–block–poly(propylene glycol)–block–poly(ethylene glycol) EO₂₀PO₇₀EO₂₀ (P123) ($M_w = 5800$) as a structure directing agent under acidic conditions [12]. In a typical procedure, 4 g of P123 were dissolved in 130 mL of DI water and 23 mL of HCl (32 wt%) in a beaker. The complete dissolution of P123 took about 1 h under vigorous stirring using a magnetic stirrer bar on a magnetic stirrer plate set at 600 rpm. This mixture was then transferred to a 2-neck round bottom flask fitted with a condenser open to air and

a thermometer. The temperature was then increased to 35 °C (actual temperature of the mixture) using an oil bath. The mixture was left under reflux for 1 h. Thereafter, 9 mL of TEOS was added dropwise to the flask and the resulting solution was stirred with a magnetic stirrer bar using a magnetic stirrer plate operating at 300 rpm, at 35 °C for 7.5 h and 24 h for SBA-15 A1 and SBA-15 A2 respectively. The solution was then transferred to a beaker and the beaker was placed in the oven set at 80 °C. The mixture was left to age at this temperature for 15.5 h and 24 h for SBA-15 A1 and SBA-15 A2 respectively, without stirring. The samples were then collected by high speed centrifugation (Eppendorf centrifuge 5702) operating at 4000 rpm for 15 min, washed with ethanol three times and dried at 80 °C in the oven overnight. The as synthesized SBA-15 samples were obtained after calcination at 550 °C using an Elite Thermal system (TSH12/38/500-2216E) tube furnace. The furnace temperature was gradually increased (heating rate of 1 °C/min) to 550 °C and thereafter, the temperature was maintained at 550 °C for 6 h. The sample was then allowed to cool down slowly in the furnace.

3.3.3 Synthesis of the Nanocomposites

3.3.3.1 Synthesis of 10% Titania Supported on Silica Nanocomposites

The Titania supported on Silica support material (SBA-15 A1, SBA-15 A2 and SiO₂) nanocomposites were prepared by hydrolysis of TTIP into the support material via a sol-gel method. A typical procedure was as follows: 0.7 g of silica support and 0.277 g of TTIP (calculated according to APPENDIX A) were added to 48 mL isopropanol in a beaker and sonicated for 20 min in an ultrasonic bath. Thereafter, 12 mL of formic acid was added to the mixture and the mixture was stirred continuously at 200 rpm for 4 h and aged for another 4 h without stirring. The beaker containing the mixture was placed in the oven at 80 °C overnight to evaporate the solvent and dry the sample. The as synthesized sample was then annealed in a porcelain boat at 500 °C using an Elite Thermal system (TSH12/38/500-2216E) tube furnace, with a heating rate of 10 °C/min. The furnace temperature was maintained at 500 °C for 3 h and thereafter, the sample was allowed to cool down slowly in the furnace. The synthesized nanocomposites are herewith referred to as 10 wt% TiO₂ / SiO₂, 10 wt% TiO₂ / SBA-15 A1 and 10 wt% TiO₂ / SBA-15 A2.

3.4 FABRICATION OF THE DSSCS

This section focuses on the procedures used for the preparation of different components of the DSSCs such as the preparation of the photoanodes, dye solution and counter electrodes. The procedures for the evaluation of the dye adsorption capacity and morphology of the photoanodes are also presented in this section. Finally, the procedure for the fabrication of the DSSCs is presented.

3.4.1 Cleaning of the FTO glass

The FTO glass was cut into 2.5 cm x 2.5 cm pieces using a diamond glass cutter and each of the pieces was cleaned using the following procedure [13]:

- Sonication in soapy water for 15 min
- Rinsing with copious amount of deionised water
- Sonication in water for 15 min
- Sonication in isopropanol for 15 min

The cleaned FTO glass substrates were sintered in the Elite Thermal system (TSH12/38/500-2216E) tube furnace set at 450 °C for 15 min to remove the organic residues before preparation of the counter and working electrodes.

3.4.2 Preparation of the working electrode

3.4.2.1 *Preparation and application of the paste*

The paste made from the synthesized TiO₂ sample was prepared following a modified procedure in literature [14]. In a typical procedure, 1.0 g of the TiO₂ sample, 2.5 g of water, 0.10 g of PEG, 0.03 g of acetyl acetone and 0.010 g of Triton x-100 were weighed into a sample bottle and stirred for 24 h on a magnetic stirring plate at 100 rpm. The paste was thereafter allowed to equilibrate for 15 min without stirring before it was used for the preparation of the photoanode. The electrode prepared using this paste was referred to as the reference electrode. PEG acts as the binder to prevent cracking and control the porosity during sintering of the film while Triton X-100 facilitates the spreading of the colloid on the substrate. The same procedure was followed for the preparation of the photoanodes with addition of 10 % of the synthesized TiO₂ supported on Silica (**10 wt% TiO₂ / SBA-15 A1**, **10 wt% TiO₂ / SBA-15 A2** and **10 wt% TiO₂ / SiO₂**) nanocomposites as a light scattering materials. The compositions of the prepared pastes are shown in **Table 3.3**.

Table 3.3: The composition of the prepared photoanodes

Composition	Reference Paste	Paste 1
TiO ₂ (g)	1.00	0.90
PEG (g)	0.10	0.10
Triton x-100 (g)	0.01	0.01
Acetyl acetone (g)	0.03	0.03
Water (g)	2.50	2.50
Nanocomposite (g)	0.00	0.10
Total Mass (g)	3.64	3.64
% TiO₂	27.49	24.74
% Composite in the dry paste	0.00	10.00

A 1.0 x 0.8 cm² window was marked out on the conductive side of the glass substrate using a scotch tape (50 μm) where a thin layer of the prepared paste was applied by doctor blade method [15] using a glass rod to flatten the paste. Two layers of the adhesive tapes were used to control the thickness of the paste. The paste was applied on one end of the glass substrate and spread to the other end of the glass substrate using a glass rod. The tape was then carefully removed and the film was left for 30 min at room temperature in a covered petri dish. The coated glass substrate was then heated at 120 °C on a hotplate for 20 min. The paste was thereafter sintered in the Elite Thermal system (TSH12/38/500-2216E) tube furnace, with the heating rate of 10 °C/min. The furnace was maintained at 450 °C for 30 minutes and thereafter the furnace was switched off and the electrodes were allowed to cool down slowly in the furnace before use.

3.4.2.2 Preparation of the dye solution and dye adsorption

A 0.50 mM solution of N719 dye was prepared in a 100 mL volumetric flask covered with an aluminium foil, by dissolving 59.43 g of the N719 dye in ethanol. The dye solution was then stored in a brown container and away from the light to prevent dye degradation for 24 h before use. TiO₂ photoanodes were immersed in the ethanolic N719 dye solution (0.50 mM) for 24 h. The dye loaded Titania films were rinsed with ethanol and dried in the oven at 80 °C for 30 min before they were used in the fabrication of the DSSCs.

3.4.2.3 Dye Adsorption Capacity Analysis

The concentration of the dye adsorbed on the working electrode is very important because it directly affects the cell performance. The dye concentration depends mainly on the surface properties of the TiO₂ nanoparticles, film surface area and film thickness. The adsorption of the dye on the surface of electrode was carried out by soaking 50 mg of the dry paste (TiO₂ and modified TiO₂ pastes) in 3 mL of 0.50 mM N719 ethanol solution at 25 °C for 24 h. The dye adsorbed paste was then separated from the residual dye solution by centrifugation. The dye loading measurements were conducted by desorbing the dye molecules from the paste into 4 mL of 0.10 M NaOH (1:1 ethanol : water) aqueous solution and the absorbance spectra of the desorbed dye were measured using a UV-Vis 2450 (Shimadzu Co. Ltd.) spectrophotometer.

3.4.2.4 Characterization of the photoanodes

The morphologies of the Titania photoanodes with and without the 10% Titania / Silica nanocomposites, were studied using the Vega 3 Tescan XMU SEM.

3.4.2.5 Preparation of the counter electrodes

The counter electrodes are key players in determining the energy conversion efficiencies of the DSSCs and thus a lot of efforts have been focussed in the design of counter electrodes. Up to date, Pt has been considered as the best candidate for the counter electrode. For this research project, the counter electrodes were prepared by depositing a thin Pt layer onto the cleaned FTO glass by doctor blade method, using the commercial Pt paste (Platisol T/SP paste, Solaronix). The electrodes were then sintered immediately at 450 °C for 30 min

to activate the Pt layer. The activated electrodes were immediately used for DSSCs fabrication.

3.4.3 Assembly and evaluation of the DSSCs

A DSSC was assembled in a typical sandwich-type cell by placing a platinum-coated glass electrode on the dye-sensitized photoanode (prepared according to subsections 3.4.3 and 3.4.2 in Chapter 3, respectively) and clipped together using paper clips as an open cell as shown in **Figure 3.2** below. The electrolyte (Iodolyte Z-150 (Solaronix)) was injected into the open cell from the edges and was attracted into the inner-electrode space by capillary force.



Figure 3.2: Examples of DSSC devices assembled for testing.

The solar cell devices were tested immediately under irradiance and dark current. A 45 W incandescent lamp was placed at 16 cm perpendicular to the cell. Both the digital multimeter (Keysight 34461A) and power source were connected to the cell in parallel. The voltage was gradually increased from 0 V to 0.6 V, and the current was recorded on the computer.

3.5 REFERENCES

1. Kruk, M.; Jaroniec, M. *Chemistry of Materials* **2001**, 13, (10), 3169-3183.
2. Groen, J. C.; Peffer, L. A.; Pérez-Ramírez, J. *Microporous and Mesoporous Materials* **2003**, 60, (1), 1-17.
3. Barron, A. R. *Houston, Texas: Connexions, Rice University* **2012**, p693.
4. Brandon, D.; Kaplan, W. D., *Microstructural characterization of materials*. John Wiley & Sons: 2013.
5. PJ Goodhew, J. H., R. Beanland, *Electron Microscopy and Analysis*, 3rd edition. Taylor and Francis: 2001.
6. Yang, J.; Zhang, J.; Zhu, L.; Chen, S.; Zhang, Y.; Tang, Y.; Zhu, Y.; Li, Y. *Journal of Hazardous Materials* **2006**, 137, (2), 952-958.
7. López, R.; Gómez, R. *Journal of sol-gel science and technology* **2012**, 61, (1), 1-7.
8. Minga, I.; Kurajica, S.; Mandić, V. *Acta Graphica znanstveni časopis za tiskarstvo i grafičke komunikacije* **2015**, 26, (4), 11-20.
9. Bumbrah, G. S.; Sharma, R. M. *Egyptian Journal of Forensic Sciences* **2016**, 6, (3), 209-215.
10. Stöber, W.; Fink, A.; Bohn, E. *Journal of colloid and interface science* **1968**, 26, (1), 62-69.
11. Wang, Y.; Chen, E.; Lai, H.; Lu, B.; Hu, Z.; Qin, X.; Shi, W.; Du, G. *Ceramics International* **2013**, 39, (5), 5407-5413.
12. Meynen, V.; Cool, P.; Vansant, E. *Microporous and mesoporous materials* **2009**, 125, (3), 170-223.
13. Falahatdoost, S.; Ara, M. H. M.; Shaban, Z.; Ghazyani, N. *Optical Materials* **2015**, 47, 51-55.
14. Mamo, M. A. *Functionalization of carbonaceous materials for photovoltaic devices*. 2011.
15. Tong, H.; Enomoto, N.; Inada, M.; Tanaka, Y.; Hojo, J. *Electrochimica Acta* **2014**, 130, 329-334.

CHAPTER 4: RESULTS AND DISCUSSION

4. INTRODUCTION

This chapter focuses on the physical, chemical and optical properties of the synthesized materials specifically TiO₂ nanoparticles, silica support materials and titania supported on silica nanocomposites as well as the application of TiO₂ and the nanocomposites in the photoanodes of Dye Sensitized Solar Cells. These materials have been prepared according to subsections 3.3.1.1, 3.3.2.1 – 3.3.2.2 and 3.3.3.1 in Chapter 3. The characterization techniques used to study the properties of the materials are presented in Chapter 3, section 3.2. The chapter starts with the discussion of characterization results of TiO₂ particles, followed by a discussion on the characterization results of the silica support materials. The effect of supporting TiO₂ on silica support materials and the change in TiO₂ properties are presented and discussed. Finally, a discussion on the effect of incorporating the TiO₂ supported on silica nanocomposites on the morphology of the photoanode of the DSCCs is presented.

4.1 CHARACTERIZATION OF TITANIA NANOPARTICLES

This section focusses on the results and discussion of the titania nanoparticles synthesized according to subsection 3.3.1.1 in Chapter 3. Only the XRD, Raman and TEM analysis are covered in this section. The rest of the characterization results (FTIR, DR UV-VIS and SEM-EDS) are discussed elsewhere to compare with the composites.

4.1.1 XRD ANALYSIS OF TiO₂ SAMPLE

XRD is a non-destructive technique used to study the structural properties (e.g. crystal phase, lattice parameters, crystallite size or crystalline defects) of materials. When a beam of x-rays are incident upon a specimen, a specific diffraction pattern for the material occurs. This specific diffraction pattern helps in identifying and understanding the structural properties of the specimen [1, 2].

The diffraction pattern of the TiO₂ sample is shown in **Figure 4.1**. The XRD pattern exhibited several peaks located at 2θ angle of 25.33°, 37.93°, 48.08°, 53.97°, 55.11°, 62.75°, 68.87°, 70.35° and 75.15°, corresponding to crystal phases (101), (004), (200), (105), (211), (204), (116), (220) and (215) respectively [3, 4]. **Figure 4.1** revealed that there was no peak at 2θ

angle of 27.50° , where the characteristic peak for the rutile phase of TiO_2 appears. All the peaks in the XRD pattern can therefore be clearly attributed to the anatase phase of TiO_2 (JCPDS card: 00-064-0863). The Scherrer equation was used to determine the crystallite size of TiO_2 nanoparticles. Using the FWHM of the (101) planes at 2θ angles of 25.33° , the average crystallite size was found to be 15.89 nm.

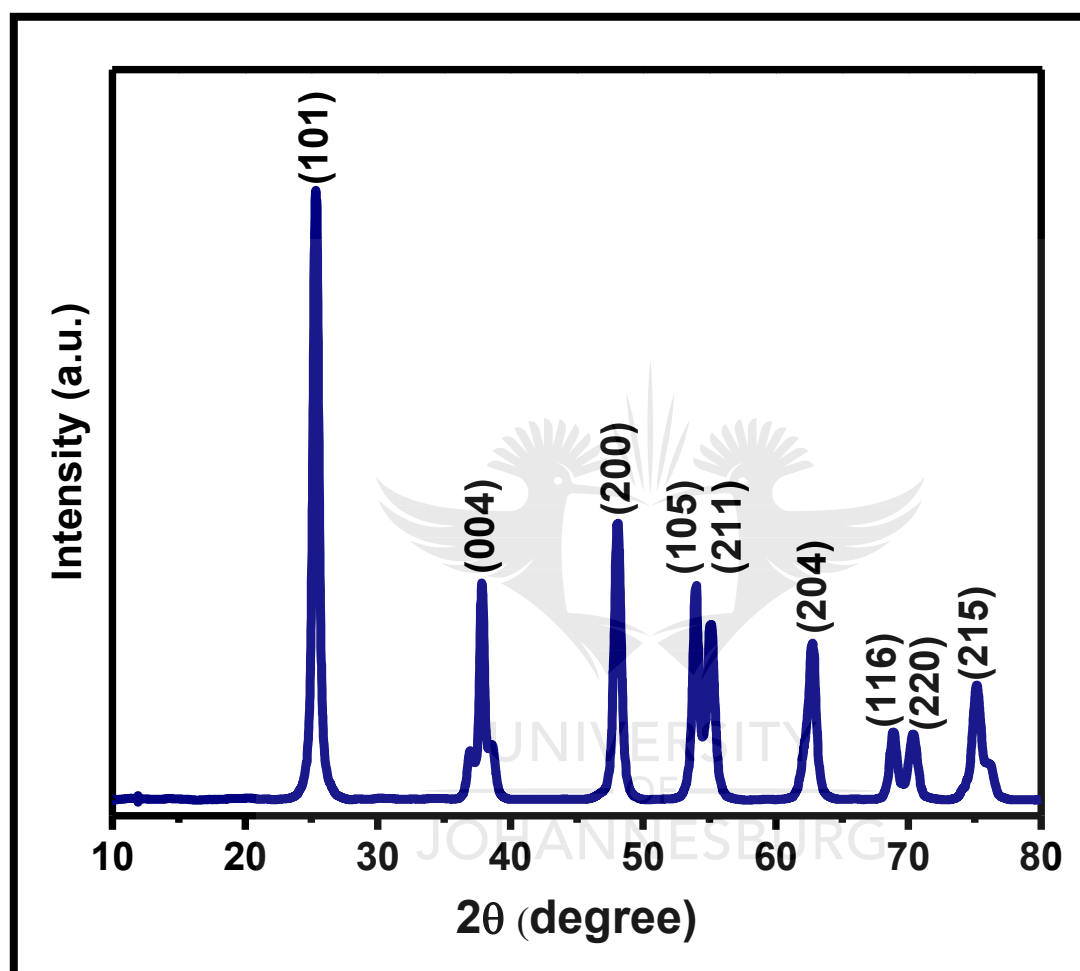


Figure 4.1: The XRD diffraction pattern of TiO_2 sample synthesized via a sol-gel method.

4.1.2 RAMAN ANALYSIS

According to factor group analysis, the anatase phase of TiO_2 has six Raman active modes, namely $A_{1g} + 2B_{1g} + 3E_g$. Ohsaka reported the Raman spectrum of an anatase phase of TiO_2 single crystal that the six allowed modes appear at 144 cm^{-1} (E_g), 197 cm^{-1} (E_g), 399 cm^{-1} (B_{1g}), 513 cm^{-1} (A_{1g}), 519 cm^{-1} (B_{1g}), and 639 cm^{-1} (E_g), which has also been reported elsewhere [5-7]. The Raman spectrum of the TiO_2 sample calcined at 500°C , presented in **Figure 4.2** exhibited four strong peaks at 142 cm^{-1} , 395 cm^{-1} , 515 cm^{-1} and 640

cm^{-1} which corresponded to E_g , B_{1g} , A_{1g} and E_g vibrational modes. The peaks at 515 cm^{-1} and 640 cm^{-1} show a slight blue shift which can be attributed to the quantum size confinement. These Raman results revealed that the phase of TiO_2 sample was anatase previously confirmed by XRD.

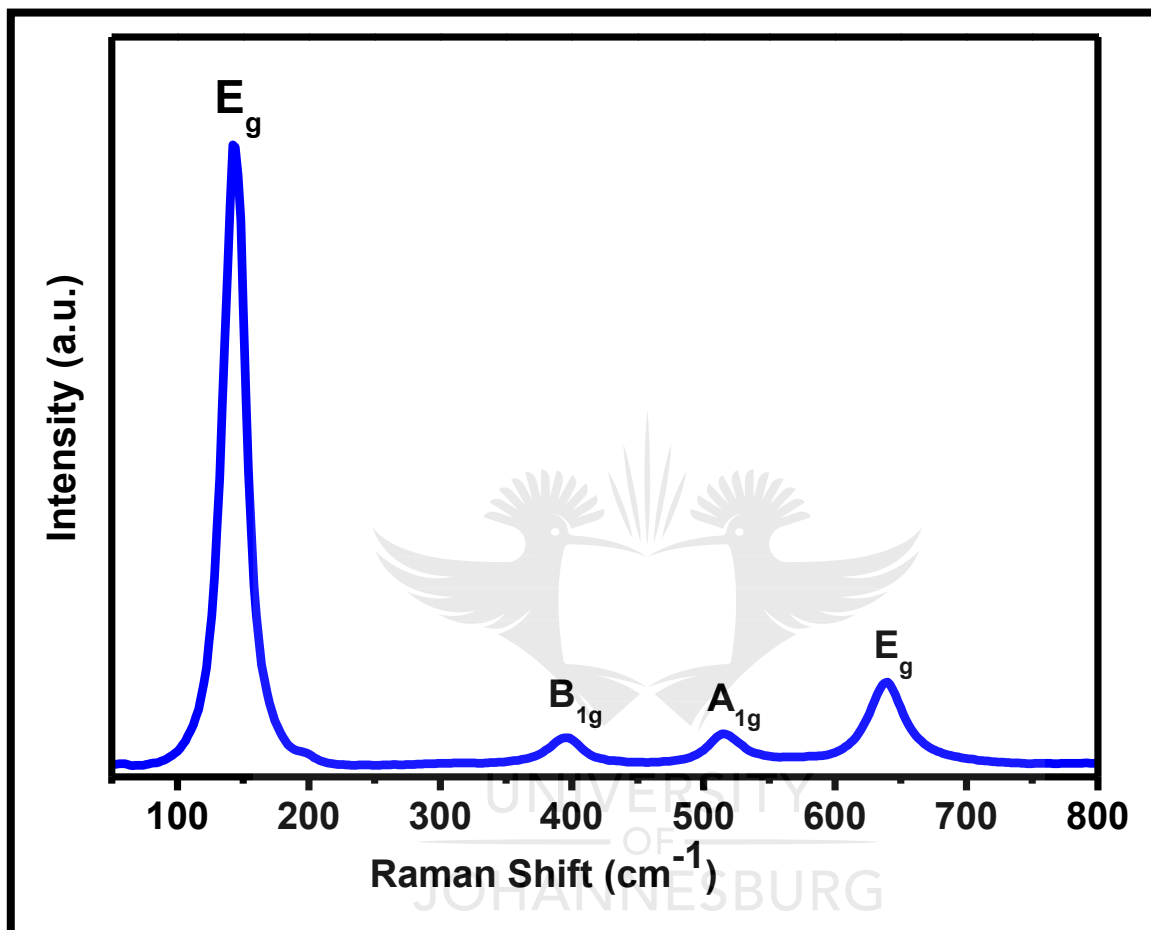


Figure 4.2: The Raman Spectrum of TiO_2 sample.

4.1.3 TEM ANALYSIS

The TEM images with particle size distribution plots of the synthesized TiO_2 samples are shown in **Figure 4.3**. The average particle sizes of the TiO_2 (**Figure 4.3**) were approximately $19.32 \pm 3.70 \text{ nm}$ ($n=193$). The TiO_2 samples were agglomerated and revealed irregular shaped particles. The active layer of the photoanode is made of TiO_2 particles with sizes ranging between $15 - 30 \text{ nm}$ [8, 9]. The synthesized TiO_2 sample had particle sizes which fall within this range and were therefore considered suitable for use as active material for the photoanode.

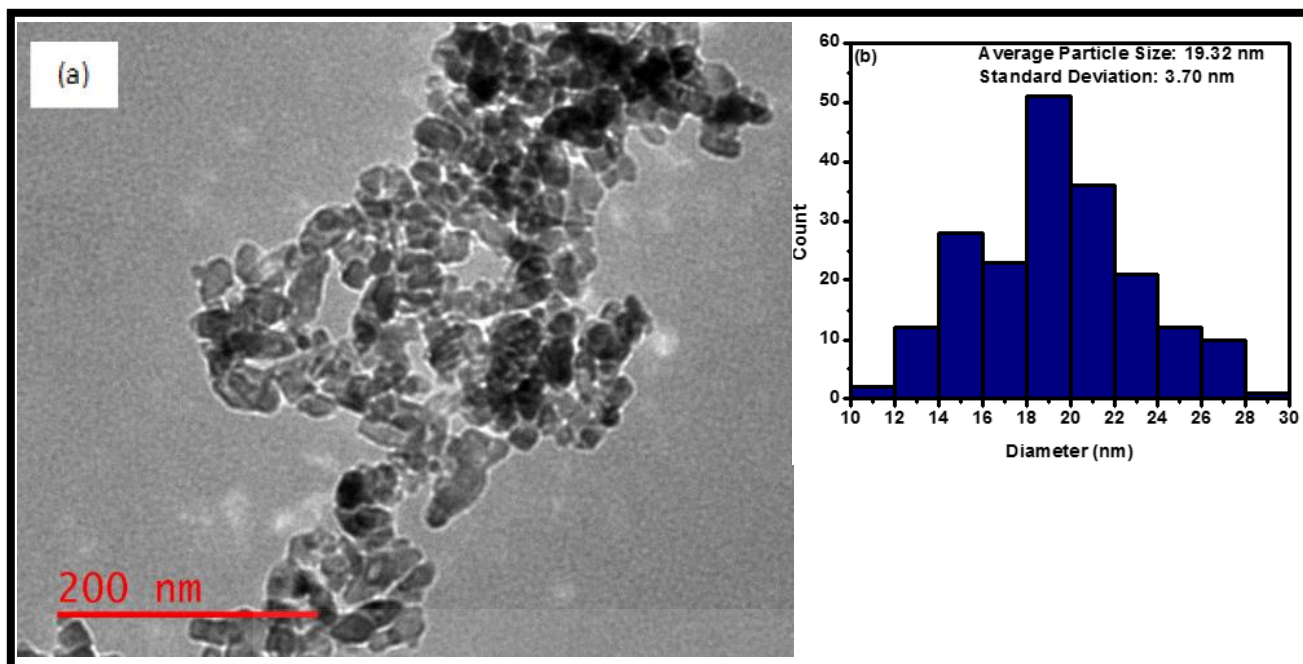


Figure 4.3: (a) TEM image and (b) the particle size diameter plot ($n = 193$) of the TiO₂ sample.

4.2 CHARACTERIZATION OF SILICA SUPPORT MATERIALS

This section focusses on the results and discussion of the silica support materials (non-mesoporous silica, SiO₂ and 2 x mesoporous silica, SBA-15), synthesized according to section 3.3.2 in Chapter 3. Only the Nitrogen Sorption and TEM analysis results and discussion are presented in this section. The rest of the characterization results (XRD, FTIR, DR UV-VIS and SEM-EDS) are discussed elsewhere for comparison with the composites.

4.2.1 TEM ANALYSIS

4.2.1.1 Non-mesoporous Silica Particles

The morphology and size of the non-mesoporous silica support material were analysed using TEM. The images and the particle size distribution of non-mesoporous silica (SiO₂) support material are presented in **Figure 4.4**. **Figure 4.4** (a) revealed that the silica particles were non-aggregated and had uniform spherical shapes, which is in agreement with earlier findings in literature [10, 11]. The particle size distribution plot in **Figure 4.4** (b) showed that the average diameters of silica particles ranged from 290 nm to 370 nm, with an average particle diameter of 331 ± 12.9 nm, determined from 152 particles ($n = 152$). Recently, incorporation of large sized nanoparticles and porous nanostructures as light scattering

materials in the TiO₂ film has attracted a lot of attention because light scatters lead to the dye molecules absorbing more photons and hence improve the efficiency of the cell.

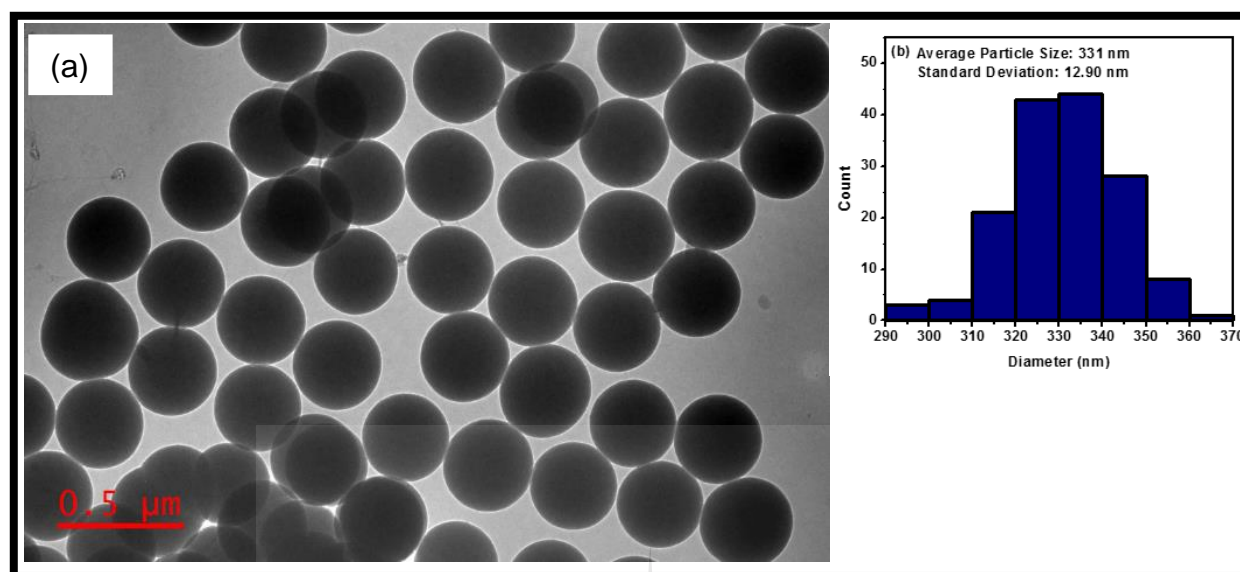


Figure 4.4: (a) TEM Image and (b) Particle Size Distribution plot (n = 152) of the non-mesoporous silica sample.

4.2.1.2 Mesoporous silica SBA-15 A1 and SBA-15 A2 particles

Two SBA-15 powders synthesized by varying hydrolysis and aging times were used in this research project. The TEM images of SBA-15 samples are shown in **Figure 4.5**. The images show a highly uniform and hexagonally ordered pore structure of SBA-15 which is similar to what has been described in the literature [1, 12]. The two SBA-15 samples revealed different morphologies. The SBA-15 A1 which was synthesized at shorter hydrolysis time (7.5 h and aging time (15.5 h) were almost spherical while the SBA-15 synthesized at longer hydrolysis time (24 h) and aging time (24 h) revealed a curved rod-like structures. These different morphologies have been reported in literature [1]. The morphologies of the SBA-15 silica can be controlled by varying the synthesis parameters such as reaction times and temperatures, silica sources, addition of salts and use of co-solvents as well as varying the surfactants [1, 13]. In this case, since only the reaction times (hydrolysis and aging) were varied, it is assumed that the difference in morphologies resulted from the difference in hydrolysis times.

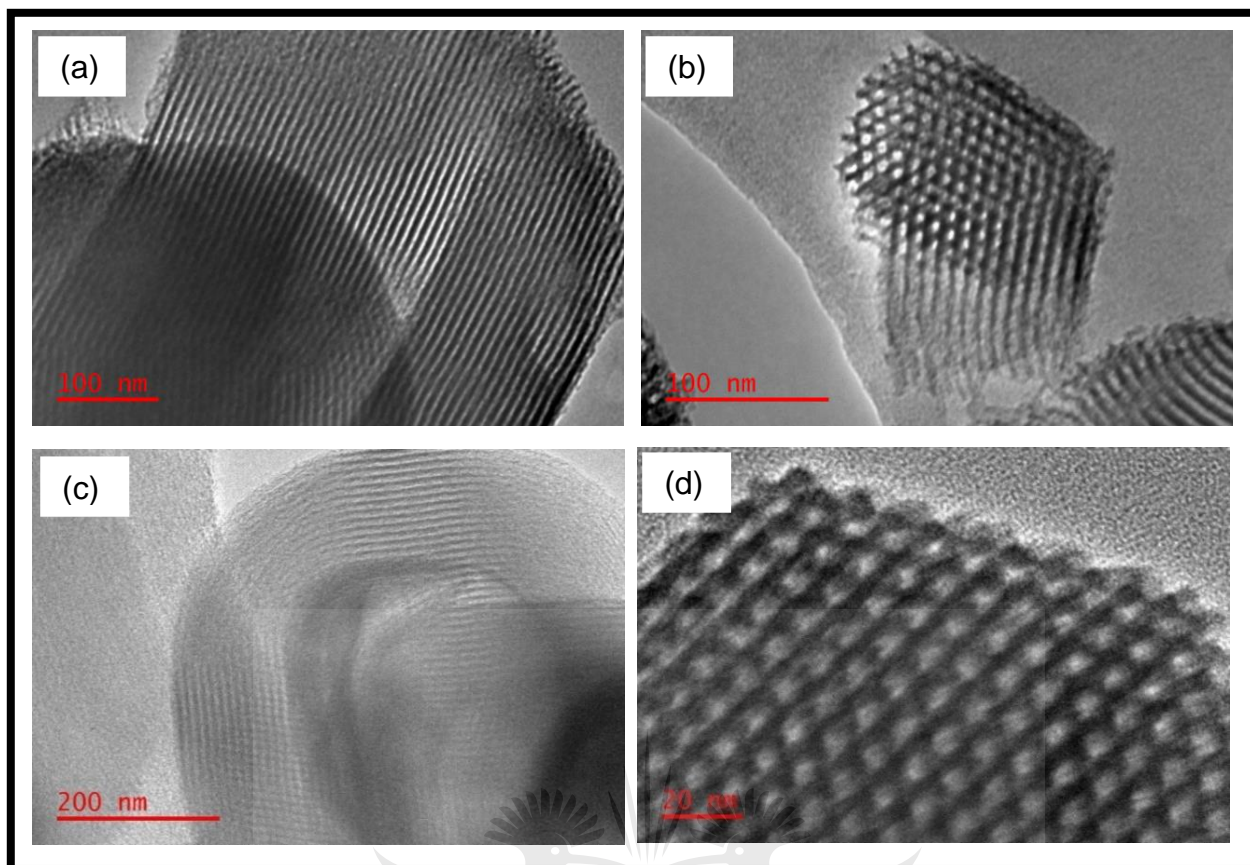


Figure 4.5: TEM images of (a) - (b) SBA-15 A1 and (c) - (d) SBA-15 A2 samples.

4.2.2 Textural properties of SiO₂ and SBA-15 samples

The textural properties of the synthesized silica support materials were investigated and their nitrogen adsorption-desorption isotherms are presented in **Figure 4.6**. From **Figure 4.6 (a)**, the shape of the isotherm can be classified as a type III, according to the IUPAC classifications [14], and the lack of a hysteresis loop shows that the SiO₂ submicron particles are not mesoporous. In addition the surface areas of the submicron SiO₂ was only 10.79 m²/g, also indicating that the SiO₂ sample is not mesoporous. The lack of mesoporosity is in agreement with the structures observed under TEM. The average pore size of the non-mesoporous silica was 37.32 nm which is an indication of the voids between the particles and not the pores in the silica structure.

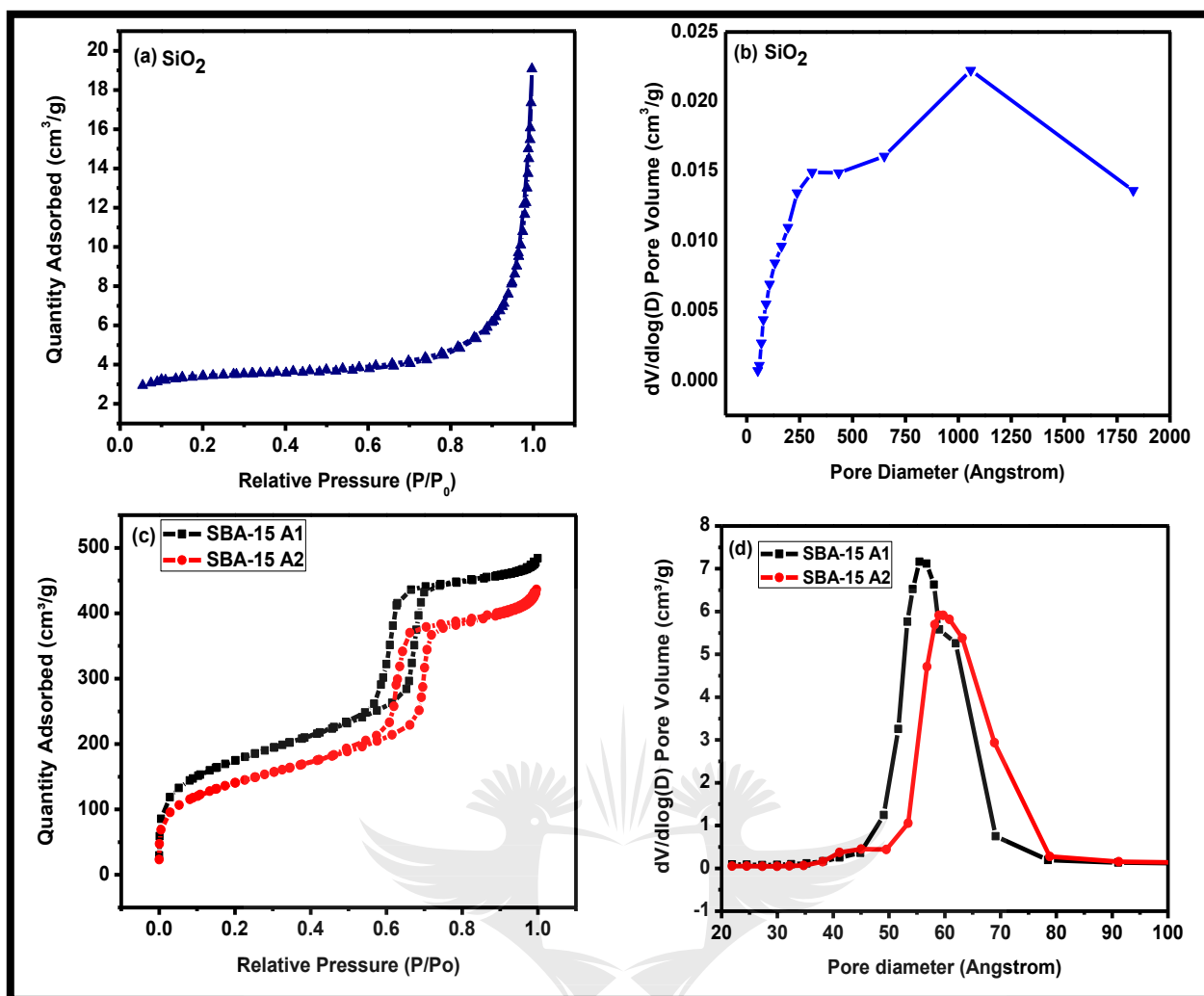


Figure 4.6: Nitrogen desorption isotherms for (a) SiO₂, (b) SBA-15 A1 and A2 and (c) their respective pore size distribution plots.

The Nitrogen adsorption-desorption isotherms for the two SBA-15 support materials in **Figure 4.6** (c) revealed the type IV characteristic isotherms with parallel adsorption and desorption branches. These observations matched the IUPAC classification of mesoporous materials with H1 hysteresis loops which clearly indicate the presence of uniform cylindrical mesopores [14, 15]. The sharp variation in relative pressures P/P_0 between 0.55 and 0.8 in the isotherms was due to capillary condensation within the ordered mesopores, which was an indication of the high uniformity of the pores in the two SBA-15 materials. Capillary condensation occurred at relatively similar pressures for SBA-15 A1 and SBA-15 A2, however for the former, the adsorption/desorption isotherms are shifted to lower values of the adsorbed volume. The pore size distribution plots in **Figure 4.6** (d) revealed an average pore sizes of 5.17 nm and 6.30 nm for SBA-15 A1 and SBA-15 A2 samples respectively. The results for the silica support materials shown in **Table 4.1** revealed that the specific surface areas were 605 and 488 m²/g for SBA-15 A1 and SBA-15 A2 respectively. The large

specific surface areas (SSA) and their corresponding large average pore sizes make SBA-15 samples ideal for metal oxides (such as TiO₂) impregnation [1].

Table 4.1: Textural properties of the synthesized materials

Sample	SSA (m²/g)	Pore volume (cm³/g)	Average pore diameter (nm)
SiO₂	10.79	-	-
SBA-15 A1	604.61	0.737	5.17
SBA-15 A2	488.28	0.682	6.30

The high surface area and porosity are essential characteristics of an efficient photoanode. High surface area is necessary for efficient dye loading while porosity is important for efficient electrolyte diffusion and electron transport [16]. These silica samples (SiO₂, SBA-15 A1 and SBA-15 A2) were used as support materials for the TiO₂ nanocomposites.

4.3 CHARACTERIZATION OF TITANIA SUPPORTED ON SILICA NANOCOMPOSITES

This section presents and discusses the results for the characterization of the nanocomposites using XRD, nitrogen sorption at 77 K, TEM analysis, SEM-EDS measurements, FTIR analysis, and the optical properties. The properties of the support materials are also provided, where necessary, for baseline comparisons.

4.3.1 XRD ANALYSIS

The TiO₂ nanoparticles were deposited on the silica support materials (SiO₂, SBA-15 A1 and SBA-15 A2) to form nanocomposites and the structural properties were studied. The XRD patterns in **Figure 4.7** show that the anatase phase was the only phase of TiO₂ that was present in all the nanocomposites. This was indicated by the dominant peak at 25.3°, a peak associated with the anatase diffraction (101). The diffraction peaks of the (101) silica phase from the 10 wt% TiO₂ / SBA-15 nanocomposites were more intense but broader than that of the 10 wt% TiO₂ / SiO₂ nanocomposite.

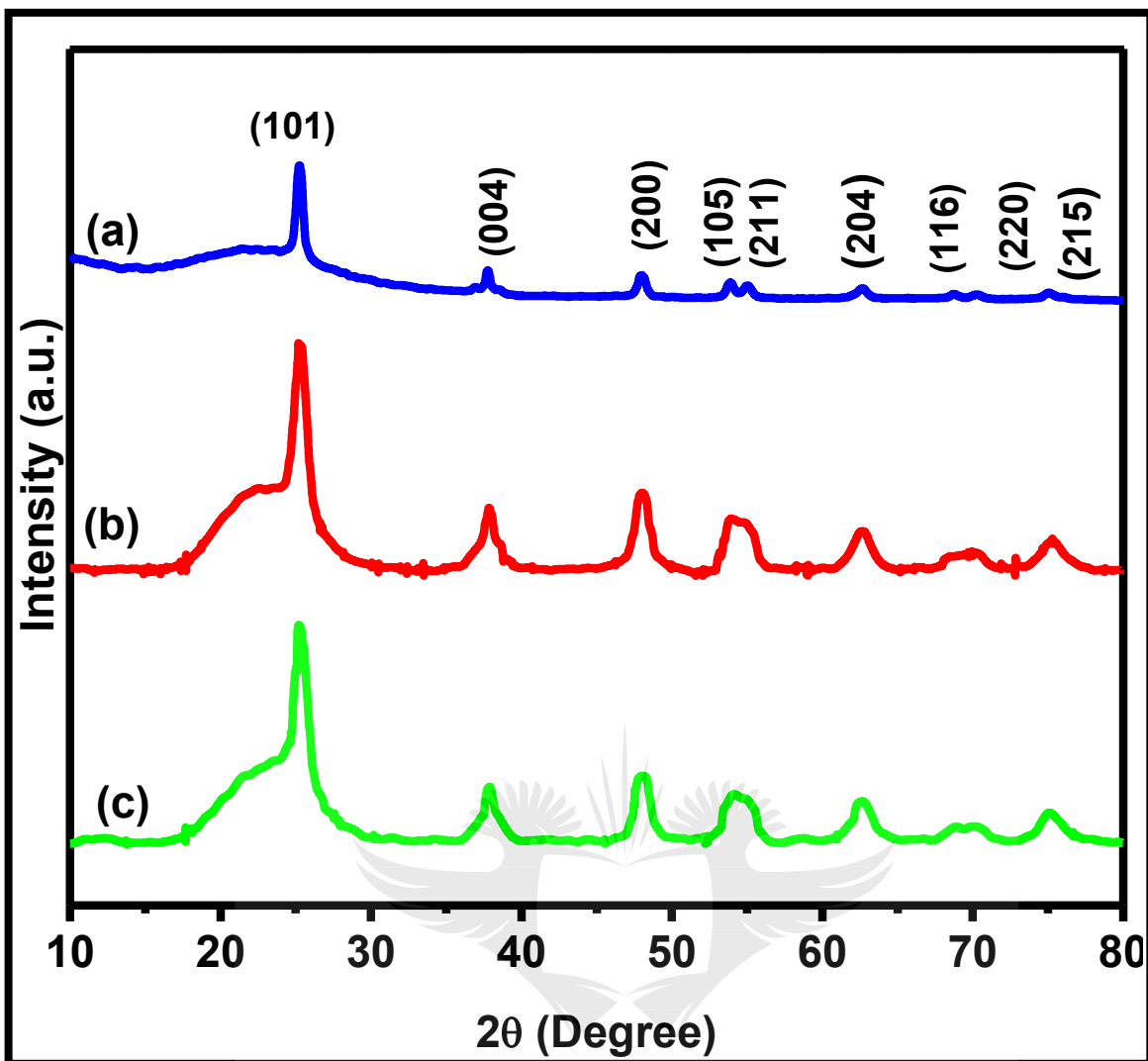


Figure 4.7: The XRD diffraction patterns of Titania supported on silica (a) 10 wt% TiO₂ / SiO₂, (b) 10 wt% TiO₂ / SBA-15 A1 and (c) 10 wt% TiO₂ / SBA-15 A2

The crystallite size generally decreases with increasing line broadening and this inverse relationship between size and FWHM is demonstrated in **Table 4.2**. The diffuse peak located at 15° – 30° in the nanocomposites was ascribed to the amorphous silica [11, 12]. The Scherrer equation was used to determine the crystallite size of TiO₂ nanoparticles in the nanocomposites, from the FWHM of the (101) plane at 2θ angle of 25.3° and the results are presented in **Table 4.2**.

Table 4.2: The crystallite sizes, calculated from the XRD pattern results, 2θ and FWHM using the Scherrer equation, of the supported and unsupported TiO₂ nanocrystals.

Sample Name	2θ (°)	FWHM (°)	d-spacing (nm)	Crystallite Size (nm)
TiO₂ nanoparticles	25.334	0.5353	0.3516	15.89
10 wt% TiO₂ / SiO₂	25.356	0.5353	0.3513	15.89
10 wt% TiO₂ / SBA-15 A1	25.313	0.8029	0.3519	10.60
10 wt% TiO₂ / SBA-15 A2	25.311	0.8029	0.3519	10.60

Incorporation of TiO₂ nanoparticles in the SBA-15 framework resulted in smaller TiO₂ crystallite sizes, as presented in **Table 4.2**. SBA-15 can therefore be seen to inhibit the growth of anatase TiO₂. This behaviour has been reported by Yang *et al.* and Ramoraswi *et al.* [17, 18]. This effect is desirable in the photoanode of the DSSCs since small crystals have high surface area which is suitable for dye loading [19]. This inhibition effect was however not evident in the non-mesoporous silica because the TiO₂ crystallite sizes remained the same as the sizes for the unsupported TiO₂ nanoparticles.

4.3.2 Textural properties of the nanocomposites

Textural characteristics, determined from gas sorption analysis, of the nanocomposites are presented in this section. The surface area, pore size, and pore volume are important characteristics of the mesoporous materials. High surface area and porosity are essential characteristics of an efficient photoanode. A photoanode with a high surface area adsorb high concentration of the dye molecules which improves the light harvesting capability of the DSSC and optimum porosity allows for the efficient electrolyte diffusion and electron transport. These properties enhance the power conversion efficiency of the cell.

4.3.2.1 Titania supported on non-mesoporous silica (10 wt% TiO₂ / SiO₂) sample

The textural properties of the TiO₂ supported on SiO₂ samples were determined using nitrogen sorption techniques and the findings are displayed in **Figure 4.8**. The 10 wt% TiO₂ / SiO₂ nanocomposite isotherm displayed in **Figure 4.8** (a) revealed a type III isotherm which is an indication that the sample was not mesoporous. The lack of mesoporosity is in agreement with the TEM results. The silica support material did not show any hysteresis

loop, however upon incorporation of the TiO₂, an H3 hysteresis loop appeared. This indicated that the sample was comprised of aggregates of TiO₂ particles and because of the irregular shapes of the TiO₂ particles, the formed aggregates resulted in the formation of voids between the particles, which resulted in the formation of the H3 hysteresis loop. This finding correlates with the TEM images of the 10 wt% TiO₂ / SiO₂ sample which exhibited small aggregates of TiO₂ nanoparticles on the surface of submicron SiO₂ support (see **Figure 4.11**). The surface area of the SiO₂ support was 10.79 m²/g which increased to 58.66 m²/g upon addition of TiO₂ nanoparticles (75.03 m²/g), as revealed in **Table 4.3**.

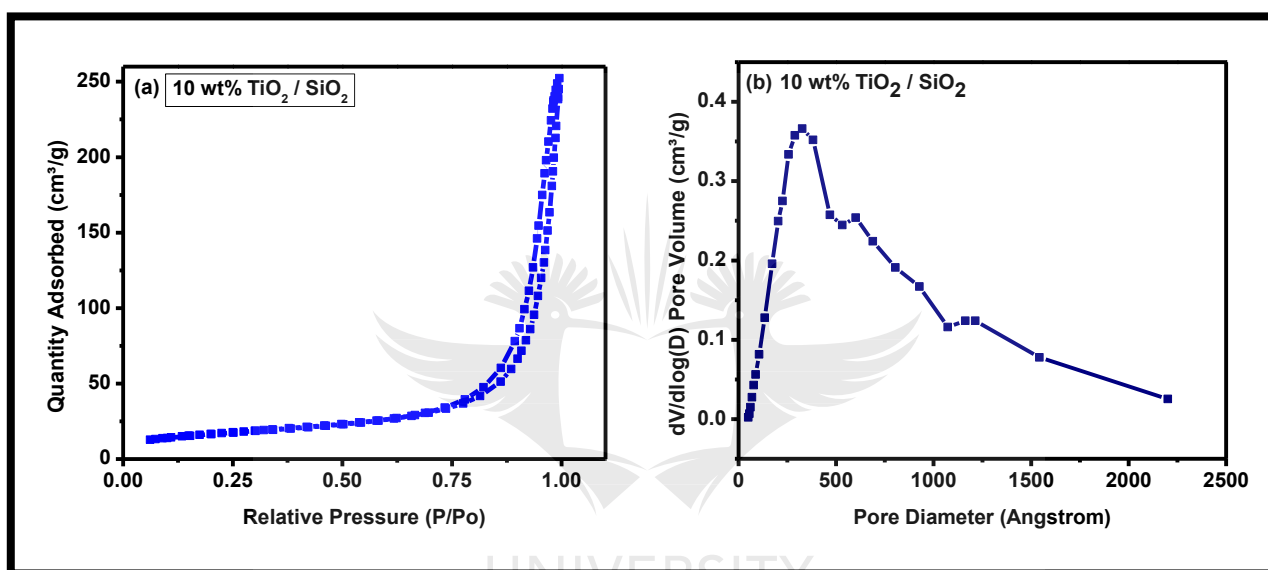


Figure 4.8: (a) Nitrogen desorption isotherm and (b) pore size distribution plot for (a) 10 wt% TiO₂ / SiO₂ sample.

4.3.2.2 *Titania supported on mesoporous Silica (10 wt% TiO₂ / SBA-15 A1 and 10 wt% TiO₂ / SBA-15 A2) samples*

The analysis of the textural properties revealed that the prepared 10 wt% TiO₂ / SBA-15 A1 and 10 wt% TiO₂ / SBA-15 A2 samples retained the ordered mesoporous structure of the parent SBA-15 A1 and SBA-15 A2 respectively. This is because the 10 wt% TiO₂ / SBA-15 samples also revealed the typical type IV adsorption isotherms which are characteristics of highly uniformly arranged mesopores [14, 20], as shown in **Figure 4.9** (a). Both the isotherms for the parent SBA-15 supports and their respective nanocomposites revealed a decrease in the adsorbed nitrogen volume. The overall shape of the isotherms indicated that incorporation of TiO₂ particles in the SBA-15 A1 framework did not alter the uniformity of the mesopores.

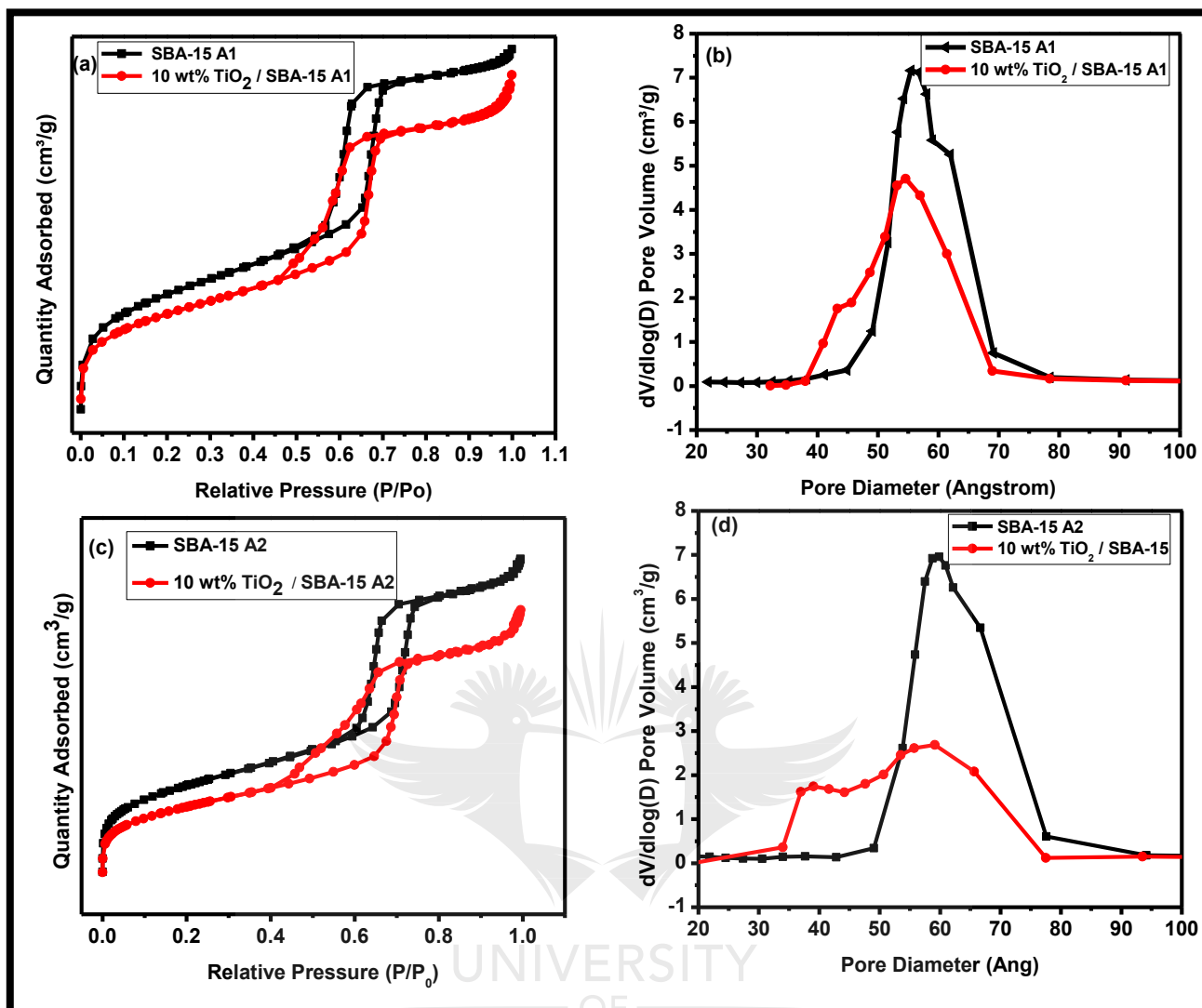


Figure 4.9: (a) Nitrogen sorption isotherms and (b) pore size distribution plots for SBA-15 A1 and 10 wt% TiO₂ / SBA-15 A1 samples. SBA-15 A1 hydrolysis and aging times were 7.5 h and 18 h respectively. Panels (c) nitrogen sorption isotherms and (d) pore size distribution plots for SBA-15 A2 and 10 wt% TiO₂ / SBA-15 A2 samples. SBA-15 A2 hydrolysis and aging times were 24 h and 24 h respectively.

As shown in **Table 4.3**, the 10 wt% TiO₂ / SBA-15 A1 sample exhibited a decrease in both its SSA (518 m²/g) and pore volume (0.697 cm³/g) as compared to the parent SBA-15 A1 (605 m²/g and 0.737 cm³/g respectively). The reduction in the specific surface area and pore volume could be a result of lower surface area TiO₂ particles deposited on the walls of the SBA-15 support thereby covering the micropores and hence reducing the surface area and pore volume of the support material. The average pore diameter of the 10 wt% TiO₂ / SBA-15 A1 sample (5.09 nm) was similar to the parent SBA-15 support (5.17 nm) indicating that no Titania nanoparticles were deposited in the pores.

Table 4.3: Textural properties of the synthesized particles and nanocomposites

Sample	SSA (m²/g)	Pore Volume (cm³/g)	Average Pore Diameter (nm)
TiO₂ nanoparticles	75.03	-	-
SiO₂	10.79	-	-
10 wt% TiO₂ / SiO₂	58.66	-	-
SBA-15 A1	604.61	0.737	5.17
10 wt% TiO₂ / SBA-15 A1	518.41	0.697	5.09
SBA-15 A2	488.28	0.682	6.30
10 wt% TiO₂ / SBA-15 A2	386.41	0.597	5.24

In contrast, when TiO₂ was deposited on SBA-15 A2, the shape of the isotherm changed as revealed in **Figure 4.9** (c). This indicated the existence of open and narrowed mesopores, a phenomena also evident in the pore size distribution plot (**Figure 4.9** (d)) which revealed two maxima confirming two types of pores. The PSD for SBA-15 showed only one maximum while the PSD for the composites revealed two maxima at 3.81 nm and 5.88 nm confirming the existence of two types of pores. The first part/step of desorption on the isotherm of 10 wt% TiO₂ / SBA-15, at higher P/P₀ values resulted from the open pores (**Figure 4.10 A**) while the narrowed pores were responsible for the second part of desorption (**Figure 4.10 B and C**). The second step desorption can be attributed to the dispersed Titania nanoparticles within the pores narrowing the mesoporous channels, creating ink-bottle like section (the narrowed mesopores). Busuioc, *et al.*, Sietsma, *et al.*, Thielemann, *et al.* and Dragoi, *et al.* observed similar findings [21-24].

Figure 4.10 indicates that there are two types of narrowed pores. The second pore type (**Figure 4.10 B**) results from small nanoparticles having sizes smaller than the pore diameter, deposited on the silica walls, facing each other. In this case, the pore diameter reduces. While the second type (**Figure 4.10 C**) is formed when nanoparticles with same sizes as the pore diameter deposit on both sides of the pore opening, blocking the pore while keeping the pore diameter constant [22, 24]. In our case, it can therefore be assumed that the narrowed pores revealed in **Figure 4.10 B** were generated as the pore sizes reduced from 6.30 nm to 5.81 nm as shown in **Table 4.3**.

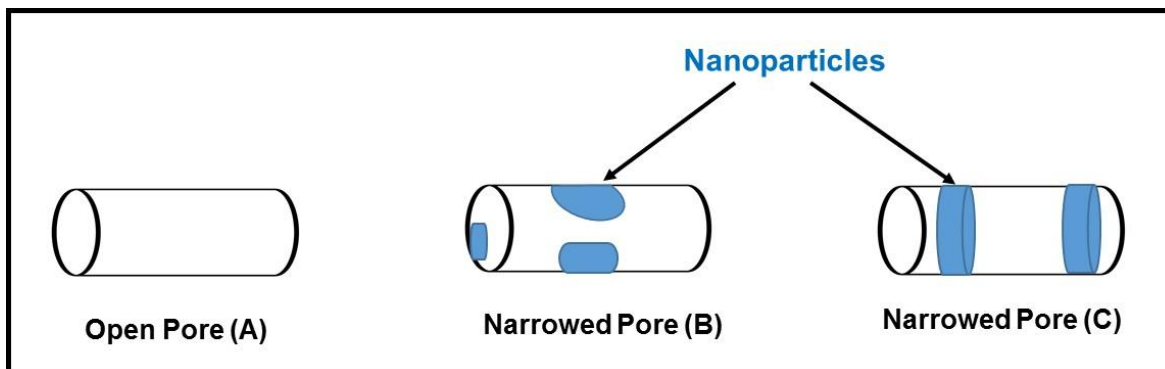


Figure 4.10: Types of pores found in SBA-15 after impregnation with nanoparticles, drying and calcination.

4.3.3 ELECTRON MICROSCOPY

Electron microscopy is a powerful technique that is used to study the morphologies, structures and compositions of materials at the nano scale [2]. The Transmission Electron Microscopy (TEM) and Scanning Electron Microscopy Energy Dispersive Spectroscopy (SEM-EDS) were used to identify the characteristic structures and study the elemental compositions of the synthesized nanocomposites.

4.3.3.1 TEM ANALYSIS

The TEM micrographs of the TiO₂ supported on Silica nanocomposites are shown in **Figure 4.11**. **Figure 4.11** (a) clearly shows that TiO₂ nanoparticles were successfully deposited on the surface of the SiO₂ submicron particles without altering the shape of the silica support. The images of TiO₂ supported on SBA-15 nanocomposites shown **Figure 4.11** (b) and (c) revealed the presence of parallel, hexagonally arranged cylindrical pores, similar to the parent support SBA-15 samples. This indicated that the incorporation of TiO₂ on the SBA-15 wall did not alter the regular arrangement of the mesopores. The nanocomposites images revealed small dark spots on the support framework and since these spots were not present in the as synthesized SBA-15 support materials, they could be attributed to the presence of TiO₂. The presence of TiO₂ on the silica support materials was confirmed by the EDS results.

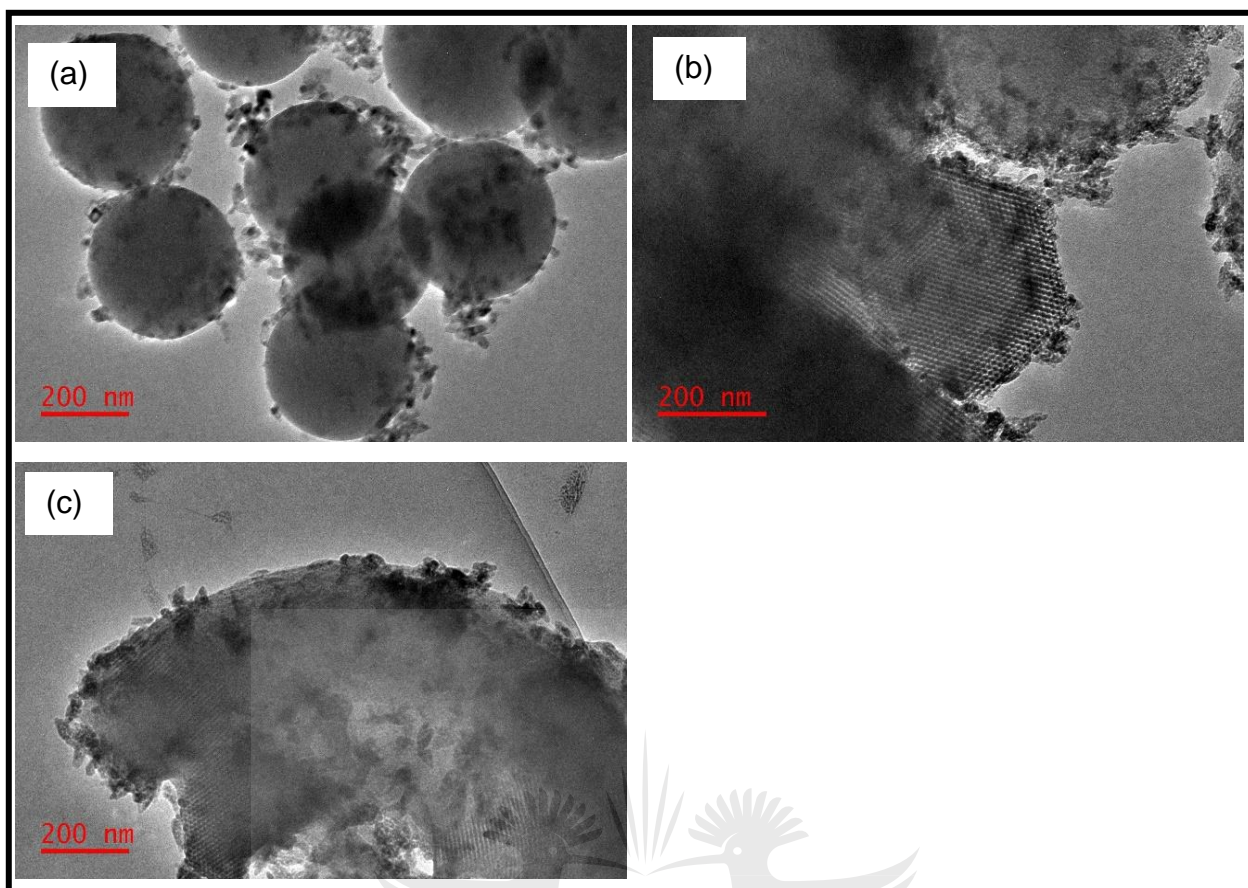


Figure 4.11: The TEM micrograms of the synthesized nanocomposites (a) 10 wt% TiO₂ / SiO₂, (b) 10 wt% TiO₂ / SBA-15 A1 and (c) 10 wt% TiO₂ / SBA-15 A2

4.3.3.2 SEM-EDS ANALYSIS

The morphologies and elemental compositions of the Silica support samples and the nanocomposites were investigated using SEM-EDS. The SEM images and EDS spectra of the nanocomposites and Silica support samples are presented in **Figure 4.12**. SEM images (**Figure 4.12** (a) – (b) and (d) – (e)) of the silica support materials (SBA-15 A1 and SBA-15 A2) and their corresponding nanocomposites (10 wt% TiO₂ / SBA-15 A1 and 10 wt% TiO₂ / SBA-15 A2) respectively, revealed the characteristic spherical and curved shapes of SBA-15. Various authors have observed similar structures using SEM analysis [1, 18]. The morphologies of the nanocomposites were found to be similar to the parent support materials, indicating that depositing TiO₂ on the silica support did not alter the shapes of the support materials. The shapes and curvatures of the pores offer an advantage for photocatalysis as it allows for efficient diffusion of molecules through the SBA-15 structures [1, 25]. This is an important feature for the efficient photoanode of the DSSC because it will allow for efficient electrolyte transport through the photoanode which could result in enhanced power conversion efficiency [16].

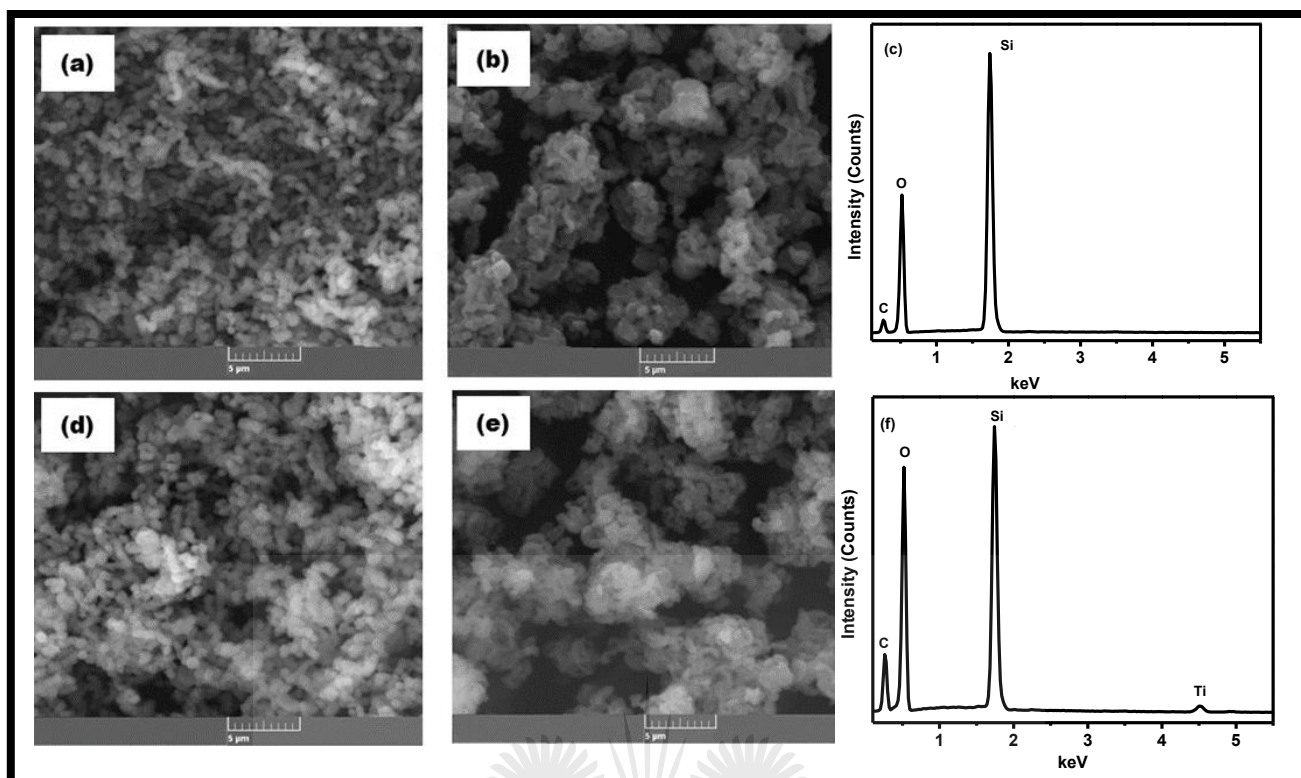


Figure 4.12: The SEM images of (a) SBA-15 A1, (b) SBA-15 A2, (d) 10 wt% TiO₂ / SBA-15 A1 and (e) 10 wt% TiO₂ / SBA-15 A2 and EDS spectra of (c) silica support samples and (f) Titania supported on silica. Only the SEM images of the Titania supported on SBA-15 are presented here to clearly show the difference in morphologies between the two SBA-15 support materials. The elemental composition of titania supported on SiO₂ were similar to the ones presented here.

The EDS spectrum of Silica supports (**Figure 4.12 (c)**) exhibited peaks attributed to Si, O and C only. There was no trace of any other elements which confirmed that these were pure Silica samples.

The nanocomposites spectrum (**Figure 4.12 (f)**) exhibited peaks attributed to Ti, Si, O and C. All samples were carbon coated before EDS analysis and the C peak could be contributed by this sample preparation step. The presence of Ti in the nanocomposites confirmed that Ti was successfully deposited on the silica support as confirmed by the TEM images. The peak ascribed to Ti was less intense in comparison to the Si peak. This showed that the Titania: Silica ratio was low because only 10% of the sample weight was TiO₂.

4.3.4 FTIR ANALYSIS

Figure 4.13 displays the FTIR spectra of Titania, silica and silica/titania composites for comparison. Since the SBA-15 nanocomposites were similar, only one of the samples is included in the Figure.

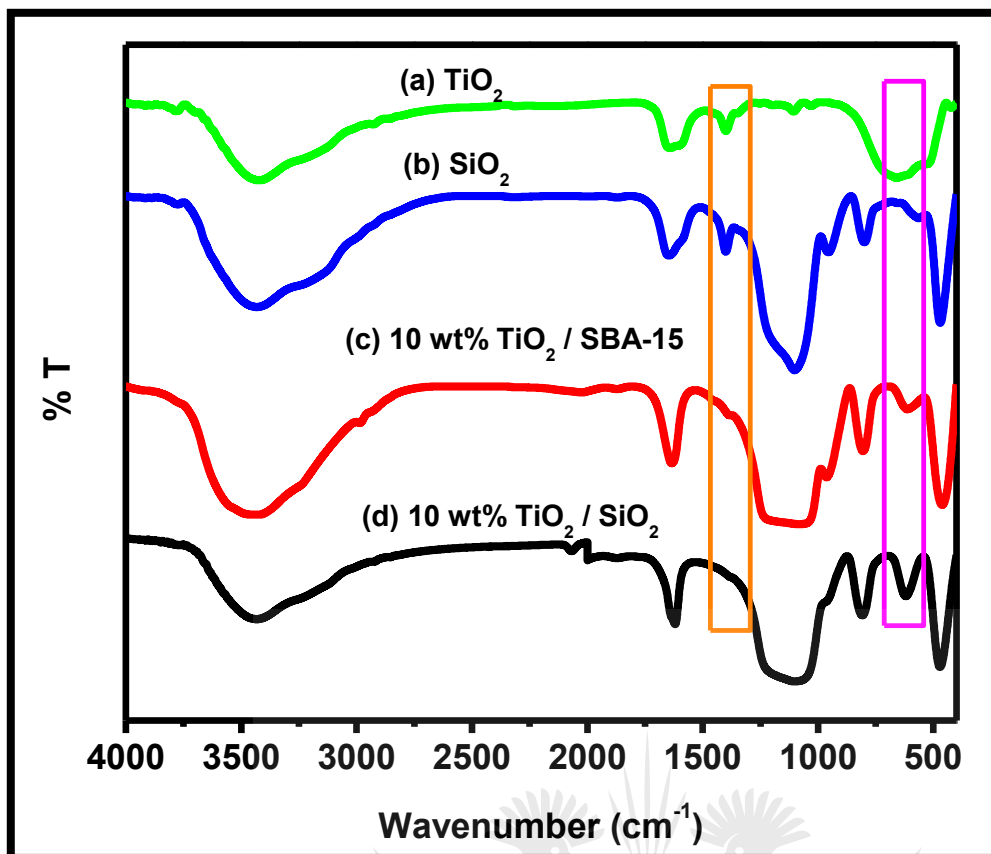


Figure 4.13: The FTIR Spectra of (a) 10 wt% TiO₂ / SBA-15, (b) 10 wt% TiO₂ / SiO₂, (c) Silica and (d) TiO₂ samples measured at room temperature.

In all spectra, the broad peaks at 3430 cm⁻¹ and 1634 cm⁻¹ were attributed to the stretching vibrations of O-H and H-O-H respectively, indicating the presence of moisture [26]. The two peaks observed at 3430 cm⁻¹ and 1634 cm⁻¹ therefore correspond to the surface adsorbed water and hydroxyl groups. The presence of hydroxyl bands in the spectra was due to chemically and physically adsorbed H₂O on the surface of nanoparticles [3]. The absorption peaks at 1404 cm⁻¹ and 1401 cm⁻¹ in the silica and Titania spectra respectively, were ascribed to the Si-O-Si and Ti-O-Ti stretching vibrations respectively. These peaks are less intense in the nanocomposites and are shifted to 1394 cm⁻¹ and 1384 cm⁻¹ in 10 wt% TiO₂ / SiO₂ and 10 wt% TiO₂ / SBA-15 respectively, indicating the formation of Si-O-Ti bond. The peaks at 1085 cm⁻¹, 804 cm⁻¹ and 464 cm⁻¹ in silica and the nanocomposites correspond to the asymmetric stretching, symmetric stretching and deformation modes of Si-O-Si respectively [10, 26]. The Titania spectrum showed a broad peak in the 400 – 800 cm⁻¹ range which is not present in silica and nanocomposite. This peak was attributed to the Ti-O-Ti vibrations [3, 10]. The band appearing in the 910 – 970 cm⁻¹ range is theoretically associated with Ti-O-Si stretching vibrations [17]. Two weak bands are observed in silica and the nanocomposites at 970 cm⁻¹ and 613 cm⁻¹. In silica, the weak band at 970 cm⁻¹ was

assigned to the Si-OH stretching vibrations. These peaks are more intense in the nanocomposites than in silica, indicating a possible formation of Ti-O-Si bond [17, 27].

4.3.5 OPTICAL PROPERTIES

The DRS UV-Vis spectra for Titania and the nanocomposite samples are shown in **Figure 4.14**. It can be clearly seen from the spectra (**Figure 4.14** (a)) that supporting Titania nanoparticles on silica resulted in a shift to lower wavelengths as compared to the unsupported Titania nanoparticles. The Titania supported on mesoporous silica shifted significantly to the lower wavelengths as compared to Titania supported on silica and TiO₂ samples. This blue shift was due to the well-known quantum size effect and suggests that incorporation of Titania on SBA-15 can significantly inhibit the growth of Titania nanoparticles. These results are consistent with the average crystallite size results from XRD. The absorption edge blue shift of the supported materials clearly indicates an increase in the energy band gap as indicated in **Figure 4.14**.

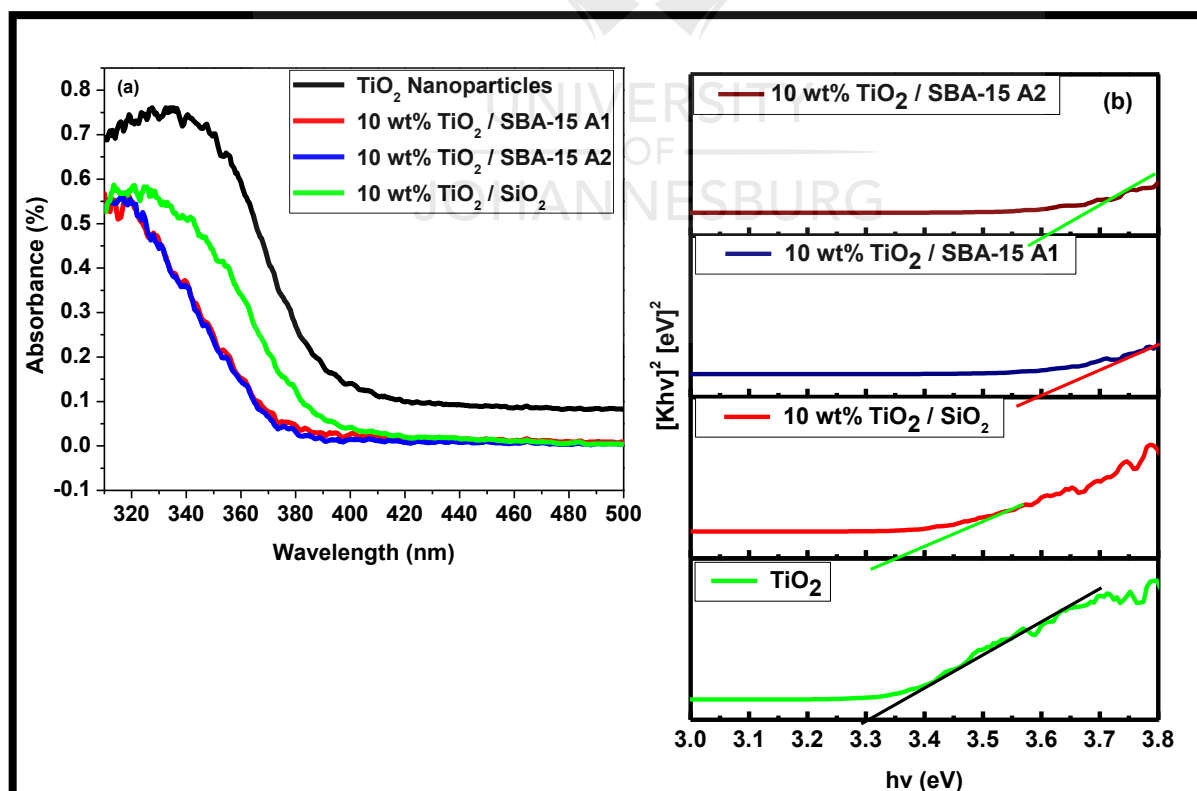


Figure 4.14: (a) The absorbance spectra and (b) the corresponding Kubelka-Munk plots of the unsupported and supported TiO₂ samples.

The optical band gaps (E_g) for unsupported and supported TiO_2 nanoparticles were calculated from the Kubelka-Munk function, **Equation 4.1** [3] [28, 29]:

$$K = \frac{(1 - R)^2}{2R} \quad \text{Equation 4.1}$$

Where R is the reflectance, while K is proportional to the extinction coefficient. By extrapolating the linear portion of the graph to $(Kh\nu)^2 = 0$ as presented in **Figure 4.14** (b). The optical band gap energy of the synthesized samples estimated from the **Figure 4.14** (b) are presented in together with their crystallite sizes. The optical band gap of TiO_2 nanoparticles was estimated to be 3.33 eV which is slightly larger than the theoretical band gap energy of bulk Titania (3.2 eV). There is no significant shift in band gap energy between the synthesized Titania nanoparticles and 10 wt% $\text{TiO}_2 / \text{SiO}_2$ (3.35 eV), which confirmed the XRD results which revealed that the crystallite sizes of the TiO_2 sample and the TiO_2 supported on SiO_2 were the same. The band gaps of the TiO_2 supported on the SBA-15 samples were 3.6 eV, which indicated a significant blue shift from the TiO_2 sample.

Table 4.4: The band gaps of the unsupported and supported TiO_2 in relation to their crystallite sizes.

Sample	TiO_2 Crystallite size (nm)	Band gap (eV)
TiO_2 Nanoparticles	15.89	3.33
10 wt% $\text{TiO}_2 / \text{SiO}_2$	15.89	3.35
10 wt% $\text{TiO}_2 / \text{SBA-15 A1}$	10.60	3.61
10 wt% $\text{TiO}_2 / \text{SBA-15 A2}$	10.60	3.60

4.4 APPLICATION

The synthesized nanocomposites, namely 10 wt% $\text{TiO}_2 / \text{SiO}_2$, 10 wt% $\text{TiO}_2 / \text{SBA-15 A1}$ and 10 wt% $\text{TiO}_2 / \text{SBA-15 A2}$ were incorporated in the photoanode as light scattering materials. This was aimed at studying their effects on the morphologies, dye adsorption capacity of the photoanodes and on the characteristic solar parameters, such as current and voltage of the DSSCs. This section therefore explores the effect of embedding these nanocomposites in the photoanodes as per the procedures described in sections 3.4 in Chapter 3.

4.4.1 PHOTOANODE MORPHOLOGY

The surface morphology of the TiO_2 ; $\text{TiO}_2 + 10\% \text{TiO}_2 / \text{SiO}_2$; $\text{TiO}_2 + 10\% \text{TiO}_2 / \text{SBA-15 A1}$ and $\text{TiO}_2 + 10\% \text{TiO}_2 / \text{SBA-15 A2}$ photoanodes were studied using SEM. The **Figure 4.15** presents the top-view SEM images of the modified and unmodified TiO_2 photoanodes. Both images revealed a number of cracks which could be due to the fast evaporation of deionised water from the top surface of the electrodes.

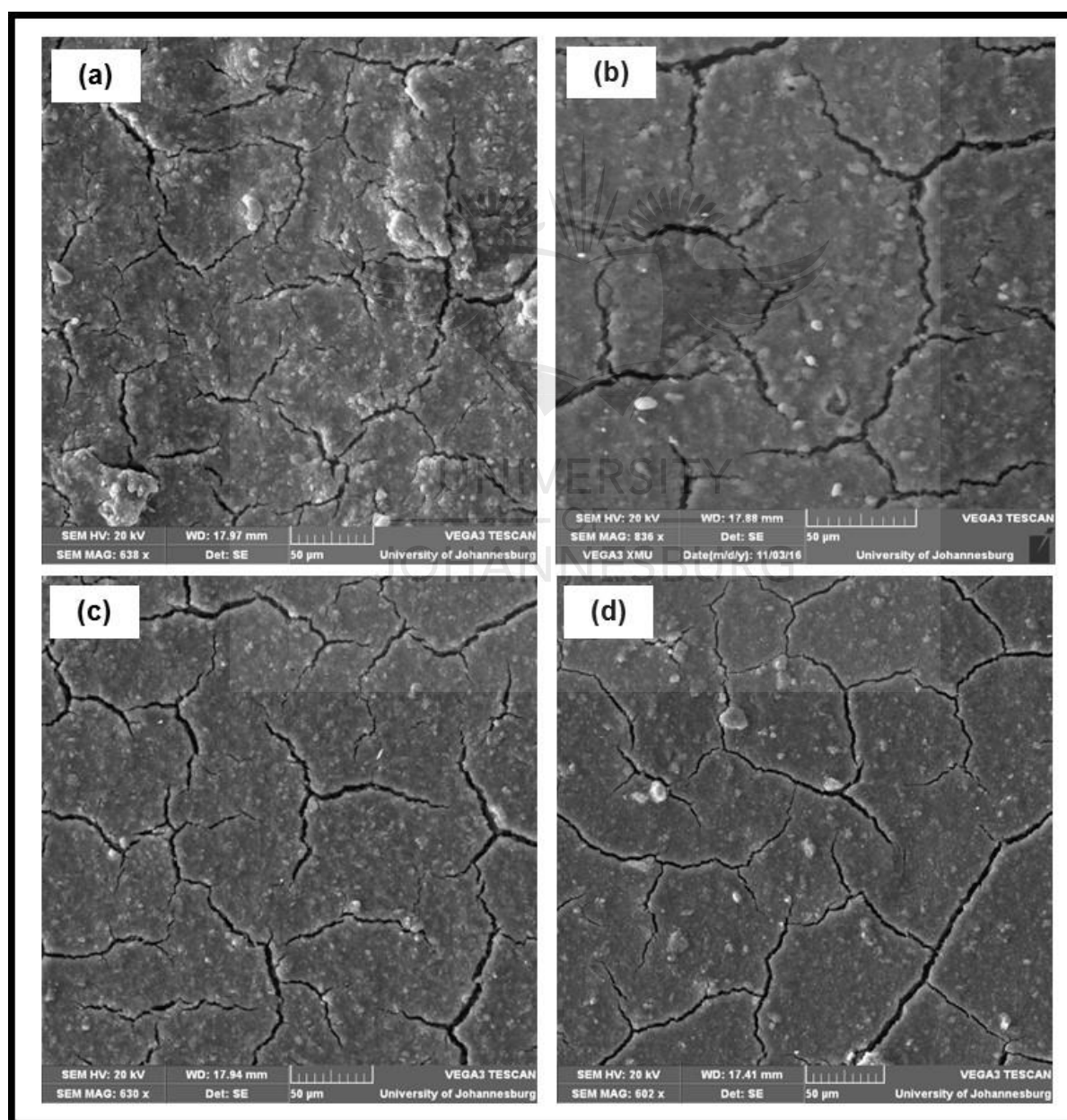


Figure 4.15: SEM images of modified and unmodified electrodes: (a) TiO_2 , (b) $\text{TiO}_2 + 10\% \text{TiO}_2 / \text{SiO}_2$, (c) $\text{TiO}_2 + 10\% \text{TiO}_2 / \text{SBA-15 A1}$ and (d) $\text{TiO}_2 + 10\% \text{TiO}_2 / \text{SBA-15 A2}$.

Incorporation of the nanocomposites did not reduce the degree of cracking however, it was observed that there was a significant improvement in terms of surface roughness although this requires confirmation with the AFM measurements. The cracking problem was attributed to the fast evaporation of the deionized water from the top surface of TiO₂ [30]. The surface of the unmodified TiO₂ photoanode was very rough as compared to the modified photoanodes. The photoanode modified with 10% TiO₂ / SBA-15 A1 was smoother than the rest of the photoanodes. Surface smoothness may lead to better electron transport as well as electrolyte diffusion which could result in improved photocurrent and hence in improvement of the energy conversion efficiency of the cells [16].

4.4.2 DYE LOADING ANALYSIS

In order to study the effect of the nanocomposites on the dye adsorption capacity of the photoanodes, the dye adsorbed pastes were immersed in sodium Hydroxide solutions which induced dye desorption. The UV Vis absorption spectra of the desorbed dye solutions were measured and the spectra are shown in **Figure 4.16**. As shown in **Figure 4.16**, two absorption peaks at around 375 nm and 502 nm were clearly observed. These are typical absorption bands of the N719 dye.

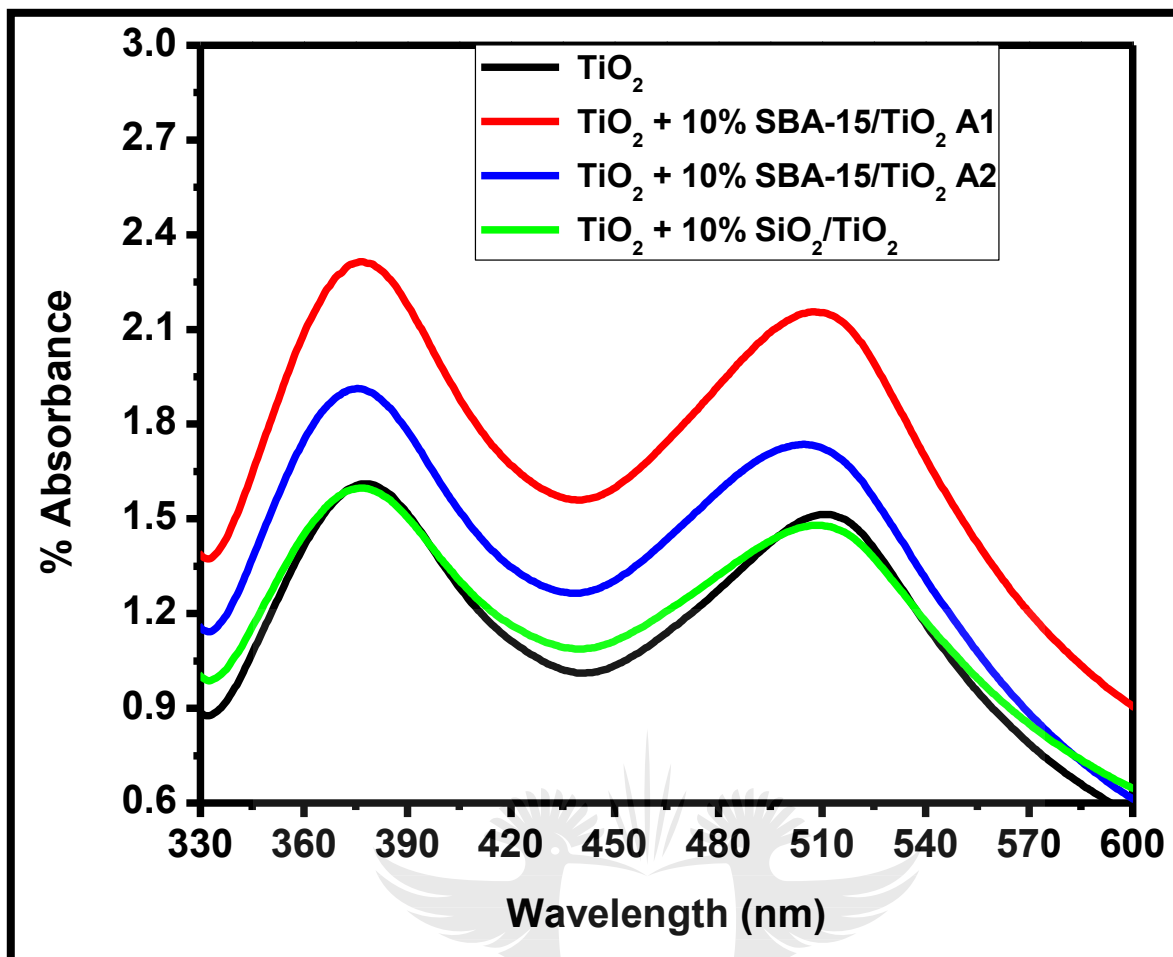


Figure 4.16: The Absorption Spectra of the N719 dye solution desorbed from the dye-sensitized TiO₂; TiO₂ + 10% TiO₂ / SiO₂; TiO₂ + 10% TiO₂ / SBA-15 A1 and TiO₂ + 10% TiO₂ / SBA-15 A2 photoanodes using 0.1 M NaOH aqueous solution.

Among the three photoanode pastes, the photoanode comprising of 10% TiO₂ / SBA-15 A1 exhibited the largest absorbance followed by 10% TiO₂ / SBA-15 A2. This is because the surface area of the 10% TiO₂ / SBA-15 A1 nanocomposite was higher than all the other nanocomposites synthesized, and upon addition of this large surface area nanocomposite, the dye loading capacity of the photoanode was improved better than the rest of the nanocomposites. The significant improvement in dye loading could result in better light harvesting and higher photocurrent conversion efficiency of the devices. There was no significant difference between the dye loading capacity of the reference photoanode made of TiO₂ only and the one with 10% TiO₂ / SiO₂ embedded in the photoanode. This is because the surface area of 10% TiO₂ / SiO₂ was not significantly different from the TiO₂ and therefore no improvement in terms of dye loading was noticed.

4.4.3 Testing and evaluation of the DSSC devices

The DSSCs composed of the synthesized TiO_2 particles and the nanocomposites were assembled and tested according to the procedure described in Subsection 3.4.3 of Chapter 3 and their I-V plots are shown in **Figure 4.17** below.

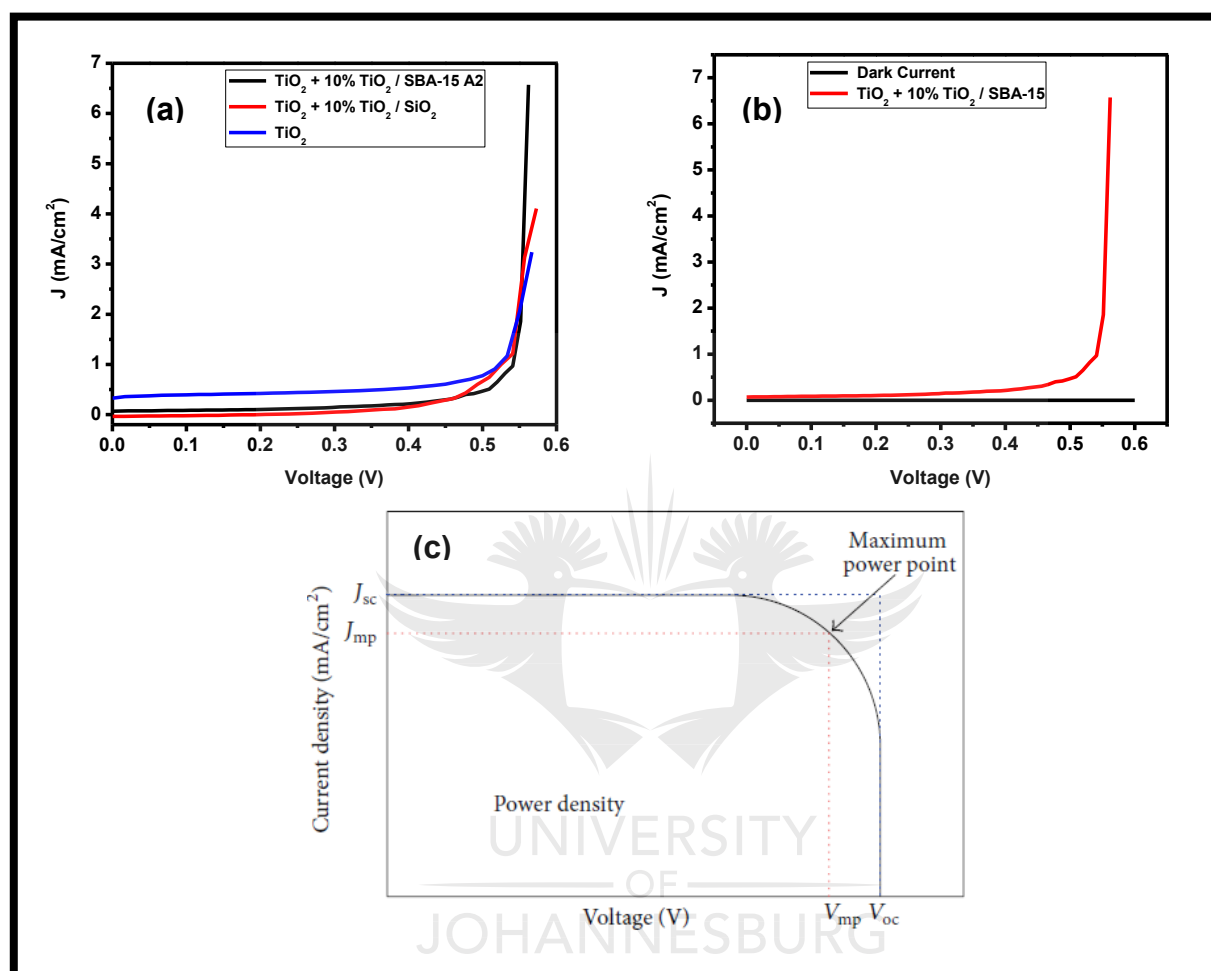


Figure 4.17: The Current-Voltage curves measured under (a) irradiance, (b) dark current and (c) an ideal DSSC curve [31]. Dark current curves for the devices showed similar trends, hence only one dark current curve is shown.

Figure 4.17(a) showed that the assembled devices revealed the electrical behaviours of photodiodes rather than that of photovoltaic cells. What was expected was at 0 V, the J_{sc} would have been at some value above zero, and at a J_{sc} of 0 mA/cm², the V_{oc} would have been between 0.6-1.1 V, as per reports in the literature. For example, Son *et al.*, reported a J_{sc} of 15.9 mA/cm² and V_{oc} of 0.71 V, after assembling a DSSC with silica nanoparticles coated with titania as the photoanode [32]. Recently, Yang *et al.*, showed that a layer of silica on top of the titania layer within the photoanode produced a maximum J_{sc} of 17.83 mA/cm² and V_{oc} of 0.715 V [33]. In contrast, Tanvi *et al.*, reported a J_{sc} of ~8.5 mA/cm² and V_{oc} ~ 0.75 V when incorporating mesoporous silica (SBA-15) within the photoanode [34].

Falahatdoost *et al.*, showed that silica coated with titania and used within the photoanode produced a J_{sc} of 16.24 mA/cm² and V_{oc} of 0.74 V [10]. In all of these previous examples, the author's I-V curves were a close approximation of the ideal curve illustrated in the **Figure 4.17(c)**.

In contrast, **Figure 4.17(a)** showed that the current densities of the devices were low until the applied voltage reached about 0.51 – 0.54 V then suddenly increased to the maximum of 3.22 mA/cm², 4.12 mA/cm² and 6.58 mA/cm² for TiO₂, TiO₂ / SiO₂ and TiO₂ / SBA-15 based devices, respectively. Such behaviour is characteristic of a diode [35, 36]. Furthermore, when the measurements were repeated in the dark (Figure 4.17 (b)), the various devices showed no effect on the current density ($J_{sc} \sim 0$ mA/cm²). This highlighted that the behaviour of the devices depends on the light applied i.e. these devices behaved as photodiodes. Ideally, the behaviour (shape of the I-V curve) of the DSSC devices does not depend on the light intensity applied.

The IV curve of the photodiode describes their operations which is based on either the Forward bias and/or Reverse bias. Forward Bias is when the anode or P type material is connected to a higher voltage than the cathode or N type material, then the width of PN junction decreases and the current flows from anode to cathode. While the Reverse Bias is when the cathode or N type material is connected to a higher voltage than the anode or P type material, then the width of PN junction increases and diode will not conduct electricity [37]. The Characteristic IV plot of the photodiode showing the Forward and Reverse bias is shown in **Figure 4.18** below. Since we only applied the positive voltage, we were only able to obtain the forward conduction/bias part of the IV curve.

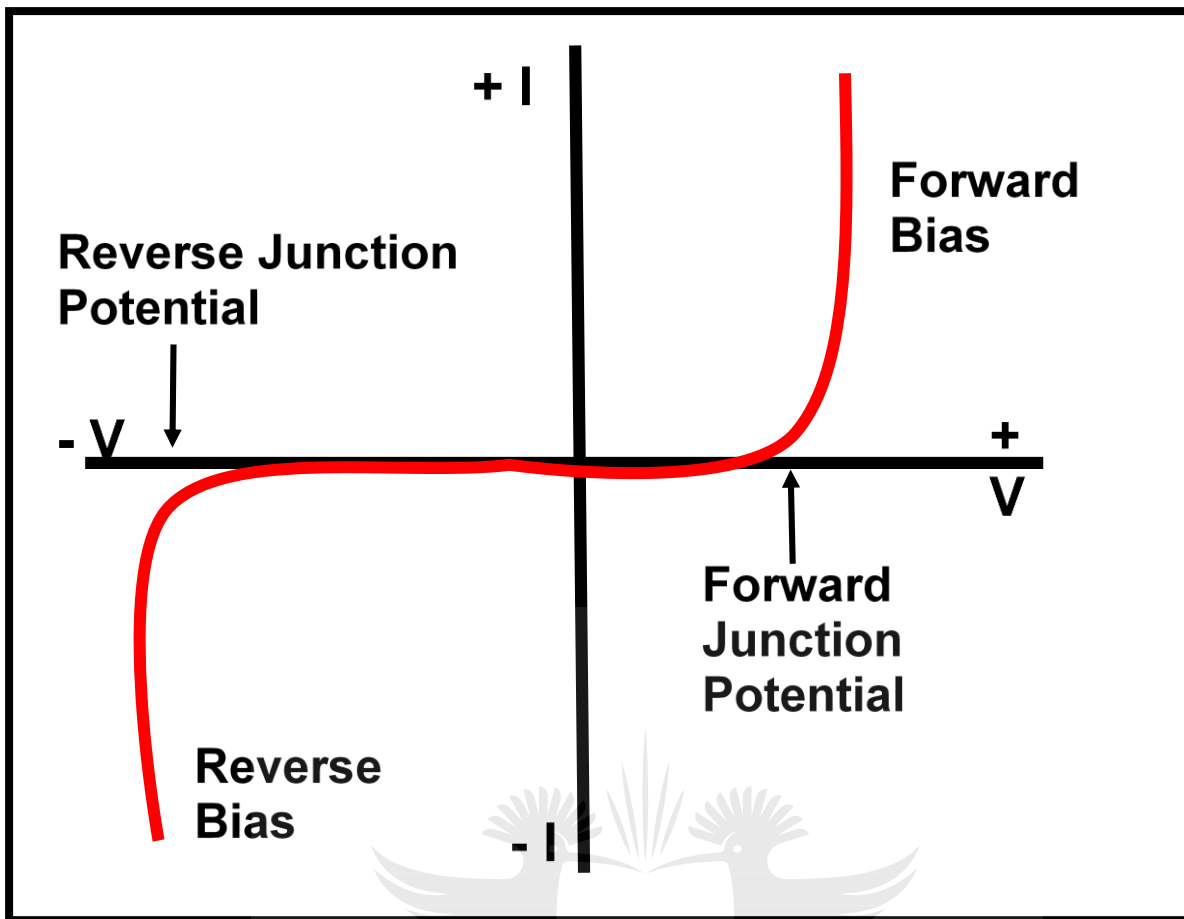


Figure 4.18: The characteristic Current-Voltage curves of the photodiode.

Pradhan *et al.*, recently reported on an inorganic-organic hybrid photodiode device, that shows similar behaviour in the forward direction (positive bias) [36]. Also, Ahmad *et al.*, recently reported on a nanocomposite containing titania nanoparticles and the results show a similar curve in the positive direction [35].

This behaviour of our DSSC devices could be due to the method used to assemble the devices. The devices were assembled by the Doctor blade method of the TiO₂ paste incorporated with the nanocomposites. This could have resulted in two separate layers, and thus the dye molecules may have been largely adsorbing on the top layer resulting in the top layer acting as the N-doped layer, while the bottom layer acting as the P-doped layer. When the light shines on the top layer, the top layer acted as an electron collector and the bottom layer acted as a hole collector at the junction, creating the depletion region between the layers. Thus further work on these devices is beyond the scope of the current project; however, this work does provide new and exciting directions of research with photo-electrochemical systems.

4.5 SUMMARY

The TiO₂ nanoparticles, silica support materials as well as the TiO₂ supported on the silica support nanocomposites were both efficiently synthesized using the sol-gel method. The characterization analysis showed that silica support materials of different textural and morphological properties were synthesized. Varying the hydrolysis and aging times resulted in two SBA-15 support materials with different morphologies, high surface areas and pore sizes. The analysis revealed that TiO₂ nanoparticles were successfully supported on the silica support materials. Titania supported on SBA-15 supports resulted in enhanced optical and structural properties of the TiO₂ as compared to the unsupported TiO₂ and TiO₂ supported on non-mesoporous SiO₂ support. The Titania particles supported on SBA-15 support materials revealed small crystallite sizes which resulted in larger band gaps. The nanocomposites with the highest surface area showed the highest dye adsorption capacity and better surface morphology once incorporated in the photoanode of the DSSC. These indicated that the Titania particles supported on SBA-15 support materials have potential to improve morphology of the photoanode of the DSSCs. The evaluation of the DSSC devices showed that the devices showed electrical behaviour of the photodiodes instead of the electrical behaviour of the photovoltaic devices. Further studies on these were however beyond the scope of this research.

4.6 REFERENCES

1. Meynen, V.; Cool, P.; Vansant, E. *Microporous and mesoporous materials* **2009**, 125, (3), 170-223.
2. Barron, A. R. *Houston, Texas: Connexions, Rice University* **2012**, p693.
3. Praveen, P.; Viruthagiri, G.; Mugundan, S.; Shanmugam, N. *Spectrochimica Acta Part A: Molecular and Biomolecular Spectroscopy* **2014**, 117, 622-629.
4. Anajafi, Z.; Marandi, M.; Taghavinia, N. *Physica E: Low-dimensional Systems and Nanostructures* **2015**, 70, 113-120.
5. Ohsaka, T. *Journal of the Physical Society of Japan* **1980**, 48, (5), 1661-1668.
6. Choi, H. C.; Jung, Y. M.; Kim, S. B. *Bulletin of the Korean Chemical Society* **2004**, 25, (3), 426-428.
7. Swamy, V.; Kuznetsov, A.; Dubrovinsky, L. S.; Caruso, R. A.; Shchukin, D. G.; Muddle, B. C. *Physical Review B* **2005**, 71, (18), 184302.
8. Rho, W.-Y.; Jeon, H.; Kim, H.-S.; Chung, W.-J.; Suh, J. S.; Jun, B.-H. *Journal of Nanomaterials* **2015**, 2015, 85.
9. Deepak, T.; Anjusree, G.; Thomas, S.; Arun, T.; Nair, S. V.; Nair, A. S. *RSC Advances* **2014**, 4, (34), 17615-17638.
10. Falahatdoost, S.; Ara, M. H. M.; Shaban, Z.; Ghazyani, N. *Optical Materials* **2015**, 47, 51-55.
11. Wang, Y.; Chen, E.; Lai, H.; Lu, B.; Hu, Z.; Qin, X.; Shi, W.; Du, G. *Ceramics International* **2013**, 39, (5), 5407-5413.
12. Zukerman, R.; Vradman, L.; Titelman, L.; Weidenthaler, C.; Landau, M. V.; Herskowitz, M. *Microporous and Mesoporous Materials* **2008**, 116, (1), 237-245.
13. Stevens, W. J.; Lebeau, K.; Mertens, M.; Van Tendeloo, G.; Cool, P.; Vansant, E. F. *The Journal of Physical Chemistry B* **2006**, 110, (18), 9183-9187.
14. Kruk, M.; Jaroniec, M. *Chemistry of Materials* **2001**, 13, (10), 3169-3183.
15. Sing, K. S. *Pure and applied chemistry* **1985**, 57, (4), 603-619.
16. Ye, Y.; Jo, C.; Jeong, I.; Lee, J. *Nanoscale* **2013**, 5, (11), 4584-4605.
17. Yang, J.; Zhang, J.; Zhu, L.; Chen, S.; Zhang, Y.; Tang, Y.; Zhu, Y.; Li, Y. *Journal of Hazardous Materials* **2006**, 137, (2), 952-958.
18. Ramoraswi, N. O.; Ndungu, P. G. *Nanoscale research letters* **2015**, 10, (1), 1.
19. Maçaira, J.; Andrade, L.; Mendes, A. *Renewable and Sustainable Energy Reviews* **2013**, 27, 334-349.

20. Kruk, M.; Jaroniec, M.; Ko, C. H.; Ryoo, R. *Chemistry of materials* **2000**, 12, (7), 1961-1968.
21. Busuioc, A.; Meynen, V.; Beyers, E.; Cool, P.; Bilba, N.; Vansant, E. *Catalysis Communications* **2007**, 8, (3), 527-530.
22. Sietsma, J. R.; Meeldijk, J. D.; Versluijs-Helder, M.; Broersma, A.; Dillen, A. J. v.; de Jongh, P. E.; de Jong, K. P. *Chemistry of materials* **2008**, 20, (9), 2921-2931.
23. Thielemann, J. P.; Girgsdies, F.; Schlögl, R.; Hess, C. *Beilstein journal of nanotechnology* **2011**, 2, (1), 110-118.
24. Dragoi, B.; Ungureanu, A.; Ciotonea, C.; Chirieac, A.; Petit, S.; Royer, S.; Dumitriu, E. *Microporous and Mesoporous Materials* **2016**, 224, 176-189.
25. Qiao, W.-T.; Zhou, G.-W.; Zhang, X.-T.; Li, T.-D. *Materials Science and Engineering: C* **2009**, 29, (4), 1498-1502.
26. Resende, S.; Nunes, E.; Houmard, M.; Vasconcelos, W. *Journal of colloid and interface science* **2014**, 433, 211-217.
27. Perathoner, S.; Lanzafame, P.; Passalacqua, R.; Centi, G.; Schlögl, R.; Su, D. S. *Microporous and Mesoporous Materials* **2006**, 90, (1), 347-361.
28. Minga, I.; Kurajica, S.; Mandić, V. *Acta Graphica znanstveni časopis za tiskarstvo i grafičke komunikacije* **2015**, 26, (4), 11-20.
29. López, R.; Gómez, R. *Journal of sol-gel science and technology* **2012**, 61, (1), 1-7.
30. Yang, C.-C.; Zheng, Y. R. *Journal of Power Sources* **2012**, 201, 387-394.
31. Kong, F.-T.; Dai, S.-Y.; Wang, K.-J. *Advances in OptoElectronics* **2007**, 2007.
32. Son, S.; Hwang, S. H.; Kim, C.; Yun, J. Y.; Jang, J. *ACS applied materials & interfaces* **2013**, 5, (11), 4815-4820.
33. Yang, W.; Chen, X.; Liu, L.; Yang, Q.; Yang, P. *Electrochimica Acta* **2016**, 213, 1-7.
34. Tanvi; Mahajan, A.; Bedi, R. K.; Kumar, S.; Saxena, V.; Aswal, D. K. *Chemical Physics Letters* **2016**, 658, 276-281.
35. Ahmad, Z.; Abdullah, S. M.; Sulaiman, K. *Measurement* **2013**, 46, (7), 2073-2076.
36. Pradhan, B.; Sharma, A. K.; Ray, A. K. *Journal of Physics D: Applied Physics* **2009**, 42, (16), 165308.
37. Othman, M.; Taib, S.; Husain, M.; Napiah, Z. *APRN Journal of Engineering and Applied Sciences* **2014**, 9, 35-44.

CHAPTER 5: CONCLUSION AND RECOMMENDATIONS

5.1 CONCLUSION

This work entailed the synthesis of silica support materials, specifically mesoporous silica SBA-15 and non-mesoporous SiO₂. Two SBA-15 nanomaterials were synthesized by varying the hydrolysis and aging times which resulted in materials of different textural and morphological properties. These silica materials were used as support for the synthesis of TiO₂ supported on silica nanocomposites. Also, TiO₂ nanoparticles were synthesized via a sol-gel method. The physical, chemical and optical properties of the nanoparticles and nanocomposites were studied using FTIR, TEM, Nitrogen Sorption, SEM-EDS, XRD and diffuse reflectance Ultraviolet-Visible (DR-UV-VIS) spectroscopy.

The TEM results revealed highly agglomerated TiO₂ particles of irregular shapes and average particle sizes of 19.32 ± 3.70 nm (n = 193). While the Raman and XRD analysis revealed the anatase polymorph of TiO₂ nanoparticles. The TEM images of the non-mesoporous silica revealed uniform spherical shapes with average particle sizes of 331 ± 12.9 nm (n = 152). The TEM analysis of the SBA-15 support materials showed highly uniform and hexagonally arranged pore structures. The morphologies and textural properties of the two SBA-15 differed depending on the hydrolysis and aging times. The SBA-15 synthesised at shorter hydrolysis and aging times were spherical with the Surface Area of 605 m²/g and average pore size of 5.17 nm. While the SBA-15 synthesised at longer hydrolysis and aging times revealed rod-like structures with the Surface Area of 488 m²/g and average pore size of 6.30 nm. The nitrogen desorption results of the 10 wt% TiO₂ / SBA-15 nanocomposites also revealed the Type IV isotherms with H1 hysteresis loops which indicated that the support materials did not lose their mesoporosity and uniform pore size arrangement upon incorporation of TiO₂ nanocrystals. This finding was supported by the TEM images of the nanocomposites which revealed the uniform arrangement of the pore structures.

The energy band gaps of TiO₂ supported on the mesoporous silica (SBA-15) (3.60 eV) were blue shifted relative to the unsupported TiO₂ (3.44 eV) and TiO₂ supported on the non-mesoporous SiO₂ (3.55 eV). These results confirmed the XRD results which indicated

smaller TiO₂ crystallite sizes for TiO₂ crystals supported on the SBA-15 support materials which was 10.60 nm as compared to the unsupported TiO₂ and TiO₂ supported on the non-mesoporous SiO₂ (15.89 nm). The band gap increased as the crystallite sizes decreased.

The TiO₂ nanoparticles were used to prepare the pastes for the photoanodes, with addition of 10% w/w of the nanocomposites to the TiO₂ particles. The photoanodes were evaluated for the dye loading capacity and their effect on the morphology of the photoanodes. The photoanode incorporated with 10 wt% TiO₂ / SBA-15 A1, which had a higher surface area, adsorbed more dye molecules than the rest of the composites. Also the top view surface morphology of the photoanode incorporated with 10 wt% TiO₂ / SBA-15 A1 had a smoother surface than the rest of the photoanode which could result in better electron transport and electrolyte diffusion. These indicated that the Titania particles supported on SBA-15 support materials have potential to improve the morphology of the photoanode. However, the performance evaluation of the assembled devices revealed the electrical behaviour of the photodiodes instead of photovoltaic solar cells.

5.2 RECOMMENDATIONS

The effect of embedding the SiO₂ / TiO₂ nanocomposites in the TiO₂ photoanodes on the dye adsorption capacity and surface morphology was studied and the results indicated that the nanocomposites are capable of improving the morphology and dye adsorption capacity of the photoanodes. However, the effect of these nanocomposites on the overall performance of the DSSCs revealed the photodiode behaviour instead of the photovoltaic solar cell. Further studies on these devices was however beyond the scope of this research.

- ✓ Since both the morphology, size, porosity and surface areas of the support materials affect the morphology of the photoanode, the use of SBA-15 of different morphologies but similar textural properties should be synthesized and be used as support materials for TiO₂ and their effects in optimizing the photoanodes should be studied and performance of the DSSC based on these nanocomposites should be evaluated.
- ✓ Since the synthesis of the particles greatly affects the efficiency of the device, other controlled synthesis method which result in less agglomerated particles with higher surface areas should be explored.

- ✓ Further investigation on the surface smoothness and/or roughness of the photoanodes should be studied by Atomic force microscopy (AFM) since this affects the electrical conductivity of the DSSC devices.
- ✓ Tape casting/doctor blade method does not result in the best photoanodes because not only the thickness of the tape and the concentration of the nanocomposite solution but also the speed of the glass rod is likely to affect the obtained film thickness and uniformity of the paste. Therefore the screen printing machine is essential for proper optimization of the nanocomposite film thickness.
- ✓ Since the thickness of the paste contributes to the performance of the device, there should be a tool to determine the thickness of the paste to allow for proper optimization.
- ✓ The Electrochemical Impedance Spectroscopy (EIS) should be conducted on the photoanodes/devices to understand the effect of the nanocomposites on inhibiting recombination as well as on charge carrier transport.
- ✓ Mechanisms of charge transfer should be investigated using Ultrafast spectroscopy techniques
- ✓ Charge injection should also be studied between the dye and the photoanode.
- ✓ Reverse bias characteristics of the devices should also be investigated.

APPENDIX A

Calculations: 10% Titania supported on Silica

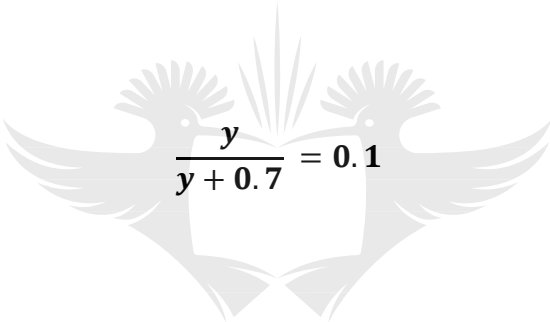
Starting with 0.7 g Silica

Find how much TTIP is needed to support 10% Titania on silica

$$\text{TiO}_2 = y$$

$$\text{MM}_{\text{TiO}_2} = 79.866 \text{ g/mol}$$

$$\text{MM}_{\text{TTIP}} = 284.215 \text{ g/mol}$$


$$\frac{y}{y + 0.7} = 0.1$$

$$0.1y + 0.07g = y$$

$$\underline{Y = 0.0778 \text{ g TiO}_2}$$

Mass of TTIP needed:

$$\frac{0.0778}{79.866 \frac{\text{g}}{\text{mol}}} \times 284.215 \text{ g/mol}$$

$$\underline{\underline{= 0.27678 \text{ g TTIP}}}$$

APPENDIX B

Calculations: 10% Silica on Titania

Starting with 1 g titania nanoparticles

Find how much TEOS is needed to support 10% Silica on Titania

$$\text{SiO}_2 = y$$

$$\text{MM}_{\text{SiO}_2} = 60.08 \text{ g/mol}$$

$$\text{MM}_{\text{TEOS}} = 208.33 \text{ g/mol}$$

$$\frac{y}{y+1} = 0.1$$

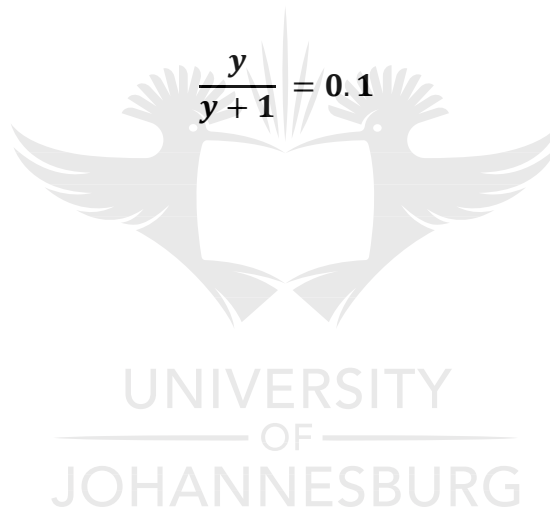
$$0.1y + 0.1g = y$$

$$\underline{Y = 0.1111 \text{ g SiO}_2}$$

Mass of TEOS needed:

$$\frac{0.1111 \text{ g}}{60.08 \frac{\text{g}}{\text{mol}}} \times 208.33 \text{ g/mol}$$

$$\underline{= 0.38528 \text{ T g TEOS}}$$





UNIVERSITY
OF
JOHANNESBURG